

Cranfield University
School of Engineering

**Development of a Dual Axis Tilt Rotorcraft
UAV: Modelling, Simulation and Control**

MSc in Autonomous Vehicle Dynamics and Control
2012

Pau Seguí Gascó

Supervisors:
Dr Al Savvaris
Dr Hyo-Sang Shin

This thesis is submitted in partial fulfilment of the requirements for the degree
of Master of Science

©Pau Segui Gasco

Abstract

This thesis stems from a project to design a novel dual axis tilt quadrotor that uses gyroscopic effects to explore an increase in the performance with respect to a conventionally actuated quadrotor. The project is developed in two theses, one by Y. Al-Rihani, [2], which develops the design and prototyping, and the present thesis which develops the mathematical model and the control system design of the new vehicle.

The main contribution of this work is the development of the mathematical model of the new actuator suite and the control system design exploiting the gyroscopic features that lead to a significant improvement in performance.

The mathematical model has 3 main areas. First, the development of the gyroscopic reaction moment equations for the new tilt mechanism design, taking into account the vehicle, the 2 tilting axes and the motor motion. Second, experiments are carried out to characterise the generation of the propeller forces and moments, alongside with an analysis of the efficiency of the propulsive system. Third and finally, a series of experiments are carried out to identify the dynamics the motor and the two RC servomotors, this is conducted by feeding a series of sinusoidal inputs and fitting transfer functions in the frequency domain.

The control system design is composed of two main parts, the control allocator design and the control law design. The control allocator design is based around a Pseudoinverse method, to develop it, a simplification of the nonlinear dynamics is carried out to derive the control effectiveness matrix, or B matrix. The control law design is based on a SISO PD controller for each Euler angle, to develop it, firstly a simplified model of the pitch or roll dynamics is developed, then, the gains are tuned by a combination of frequency domain loop shaping and rig testing.

Finally, improvements in performance of about 20% respect to a conventional actuated quadrotor are obtained with the novel actuator suite. The most important result is that, based on the obtained results, suggestions are made to improve the design of actuator suite that could lead to an order of magnitude increase in performance respect to a conventional actuator suite. Results of the first flight, rig tests and a qualitative validation of the simulation model are also presented.

Keywords: MAV, UAV, Quadrotor Design, Gyroscopic Actuation, Overactuated, Novel Actuator, Propellers as Gyroscopes.

Acknowledgements

I would like to thank Dr. Savvaris and Dr. Shin for their supportive guidance and advice along this project.

My most sincere thanks to my friend and colleague Yazan Al-Rihani who shared the project with me. The collaboration with him has been extremely fruitful, leading to a synergy which resulted in an outcome much greater than the sum of the parts. I'm thankful I learnt so much from his wisdom and experience during this project.

I am hugely grateful to Isabel, the joy of my life, for making me feel always the luckiest man on earth for sharing my life with such an extraordinary person. She was generous enough to move with me to UK and has been supportive during all the many hours of work, always giving me love, energy and encouragement to keep on.

I would like to thank my family, my father Jesus, my mother Ana and my sister Mireia. I will be forever indebted with them for all their love, support and encouragement throughout my life, they have always been there when I most needed. I have been very lucky that my father transmitted to me his love and passion for engineering and who, with his endless patience, spend countless hours sharing his wisdom. I would not be what I am today without them. Thanks.

The support of the Erasmus Programme of the Universidad Politécnic de Valencia and the Cranfield University European Partnership Programme is gratefully acknowledged.

Contents

1	Introduction	10
1.1	Background & motivation	10
1.2	Aims and Objectives	11
1.3	Key Challenges	12
1.4	An Overview of the Thesis	13
2	Literature Review	14
2.1	Introduction	14
2.2	Modelling	14
2.2.1	Quadrotor Analysis	14
2.2.2	Tilt Rotor Gyroscopic Actuation	16
2.2.3	Component System Identification	16
2.2.4	Equations of Motion	17
2.3	Control Allocation	17
2.3.1	Introduction	17
2.3.2	Control Allocation Methods	18
3	Vehicle Description	20
3.1	Introduction	20
3.2	Requirements and Baseline Specifications	20
3.3	Tilting Rotor Design	21
3.3.1	Tilting Arm Design	21
3.4	Airframe, Powerplant and Avionics	26
3.4.1	Propulsion	26
3.4.2	Sensors	28
3.4.3	Power Source (Battery)	28
3.4.4	Flight Computer	30
3.4.5	Wireless Communication	32
3.4.6	Final Mechanical Design	32
3.4.7	Custom designed parts	34
3.4.8	Description of the Design	36
3.4.9	Electronics layout	36
3.4.10	CG location	39
3.5	Mass Breakdown	39
3.6	Prototype	39

4	Modelling	45
4.1	Introduction	45
4.2	Rigid Body Modelling	46
4.2.1	Angular Acceleration	51
4.2.2	Total Moments	52
4.3	Aerodynamic Modelling	54
4.4	Motopropulsive Group Modelling and Characterisation	57
4.4.1	Static Testing	58
4.4.2	Dynamic Modelling of the Motors.	63
4.5	Servo Motor Modelling	69
4.5.1	Introduction	69
4.5.2	Experimental Setup.	69
4.5.3	Servoblock system ID	73
4.5.4	Push Pull system ID	74
4.6	Equations of motion	77
4.7	Simulation Model	78
4.7.1	Main Structure	78
4.7.2	Vehicle Dynamics Block	79
4.7.3	Actuators Block	80
4.7.4	Standard Actuator Block	80
5	Control System Design	82
5.1	Introduction	82
5.2	Control Allocator	83
5.2.1	Introduction	83
5.2.2	Control Allocation for Dual Axis Tilt Rotorcraft	87
5.2.3	Derivation of the submatrix B for the standard arm	89
5.2.4	B matrix	98
5.2.5	Weighted Pseudoinverse Control Allocator	99
5.3	Controller	103
5.3.1	Introduction	103
5.3.2	Simplified Plant Model for Controller Design	103
5.3.3	PD Design for Roll and Pitch	106
6	Testing and Results	121
6.1	Introduction	121
6.2	Validation of the Simulation Model	121
6.3	Stability at ball joint rig	125
6.4	Flight test	129
7	Conclusions of the Work	135
7.1	Conclusions of the Work	135
7.2	Future Work	136
7.2.1	Modelling	136
7.2.2	Control System	137

A	Testing Setup	138
A.1	Introduction	138
A.2	Motor Static Testing	138
A.2.1	Motor Thrust Static Test	139
A.2.2	Motor Torque static Test	145
A.3	Motor Dynamic Testing	149
A.4	Servo Dynamic Testing	151
A.4.1	Servo mapping Test	151
A.4.2	Servoblock Servo Dynamic Test	155
A.4.3	Push-Pull Servo Dynamic Test	158
A.5	Ball Joint Rig	160
B	2 blade or 3 blade propellers	161
B.1	Introduction	161
B.2	Newton Euler Description	162
B.2.1	Angular Acceleration	165
B.2.2	Total Moments	165
C	Simulink Model	167
D	Platform technical drawing	170
E	SBG IG-500N IMU Technical Specifications	172
	References	175

List of Figures

2.1	Examples of Quadrotors UAVs	15
2.2	Illustration of the quadrotor working principle. Extracted from [37].	15
2.3	Control system structure when control allocation is used. Reproduced from Harkegard, [15].	18
3.1	Servo Block [30]	21
3.2	Tilting Arm Design	22
3.3	Tilting Arm Parts	23
3.4	Tilting arm mechanism components	23
3.5	Push-Pull arm and its components	24
3.6	RC Servos	25
3.7	Masterairscrew 12 x 6 3-blade [23]	26
3.8	MK3638 Brushless motor [25]	27
3.9	Roxyy BI Control 930-6 [29]	27
3.10	SBG IG-500N [35]	28
3.11	4 cell flat battery	29
3.12	Mikrokopter Battery Holder	30
3.13	chipKIT Max32 Prototyping Platform [8]	30
3.14	Propeller Servo Controller USB	31
3.15	Wireless Data Communication kit	33
3.16	Radio Control kit	33
3.17	Motor bracket	34
3.18	Central Plate	35
3.19	Central body structure	35
3.20	Mikrokopter landing gear	36
3.21	Servo blocks in the central body	37
3.22	Tilting mechanism	37
3.23	Assembled Arm	38
3.24	Avionics components arrangement	38
3.25	CG Location.	40
3.26	Dual axis Tilt rotor Arm mechanism	42
3.27	Electronics layout	43
3.28	Dual axis Tilt rotor UAV	44
4.1	Body axes reference frame and arm numbering.	47
4.2	Spinning body studied, i.e. propeller+motor rotor.	47
4.3	Reference frames used in the development.	48
4.4	Thrust Measurement Stand.	55

4.5	Torque Measurement Stand	56
4.6	Laser Interferometer Setup.	56
4.7	Thrust vs $\rho A(\Omega R)^2$	57
4.8	Torque vs $\rho A(\Omega R)^2 R$	58
4.9	Mechanical Power vs Electric Power.	59
4.10	Efficiency vs Mechanical Power Output. From fitted curve (eq. 4.43) and raw data.	60
4.11	Throttle Position vs Angular Velocity of the Propeller, Steady state.	61
4.12	Thrust vs Throttle, Controller Linearity.	61
4.13	Hovering Efficiency vs Thrust Generated.	62
4.14	Description of the Frequency Domain identification process	64
4.15	Description of the frequency domain data processing. Blue is input and red is output, in order to be able to plot them in the same picture they've both been normalised with amplitude one and zero average.	65
4.16	Sample of a fitted sinusoidal to a throttle input of 0.8Hz frequency.	66
4.17	Phase and Gain for all the frequencies fed into the motor around the 50% throttle operating point. Note that the input throttle from 0 to 1 and the output is in radian per second. Therefore an offset in the gain is due to unit scaling.	67
4.18	Frequency domain motor transfer function gain fit.	67
4.19	Frequency domain motor transfer function gain and phase fit.	68
4.20	Servoblock motion testing on the prototype arm.	70
4.21	Pushpull motion testing on the prototype arm.	70
4.22	Data processing for the servo sinusoid System Identification. Blue is input and red is output.	72
4.23	Frequency domain servoblock transfer function gain and phase fit.	73
4.24	Frequency domain servoblock transfer function gain and phase fit.	74
4.25	Frequency domain Push Pull transfer function gain and phase fit.	75
4.26	Frequency domain Push Pull transfer function gain and phase fit.	76
4.27	Main structure of the simulation model.	78
4.28	Inside of the Vehicle Dynamics Block.	79
4.29	Actuator Block, generates the forces and moments from the control inputs and the angular motion.	80
4.30	Standard Actuator model, mechanises the dynamics: Rigid Body and Aerodynamics of an arm.	81
5.1	Main structure of the control system.	82
5.2	Main structure of the control system.	88
5.3	Standard Arm and definition of the angles.	90
5.4	Response of the servo and the gyroscopic pitching moment to an input of 0.1(rad) in the servoblock servo at time 0. Note time scale $\approx 0.2s$	91
5.5	Pitching moment response generated by the motors following a differential step of 1% in throttle at time 0. Note time scale $\approx 0.8s$	91
5.6	Normalised pitching moment response generated by the motors following a differential step and the servo gyroscopic effects following a step at time 0. Note difference in time scales.	99

5.7	Illustration of the concept of the control allocator as a “mixer” of the two kinds of effectors. Note that all the responses are normalised.	101
5.8	Normalised pitching moment response generated by the allocator for different weights w_{motor} ranging from 0 to 1. Note the red line when $w_{\text{motor}} \approx 0$, thus, being basically executed by the motors alone.	101
5.9	Resulting allocator with $w_{\text{motor}} = 0.994$. Blue lines show the responses for several Pitching Moment (N) step commands from 0 to 1 Nm. The red line represents the response when $w_{\text{motor}} \approx 0$. Note the dashed lines showing the settling time (95%) for the two actuator combinations.	103
5.10	Frequency response of the different sets of effectors. Blue using weighted pseudoinverse allocator and red using differential thrusting approach.	104
5.11	Simplified Open Loop Pitching Dynamics. Where θ is the pitch angle, v_p pitching moment command, and N the pitching moment.	105
5.12	Pitching Moment Response of the Simplified Open Loop Pitching Dynamics (Red) vs the Full Nonlinear Model (Blue).	106
5.13	Mapping of the pilot reference inputs to the control system.	107
5.14	Structure of the PD controller for the pitching dynamics.	108
5.15	GUI to modify the gains and display the closed loop frequency responses. T is presented in Blue, S in Red and L in Yellow.	110
5.16	Detail of the ball joint rig. The ball joint is attached to a frame by a bicycle hub that allows the ball joint to spin, yaw, freely. On its side, the ball joint allows for free movement of the pitch and roll axes. Hence, the only motion constrained is the translational.	110
5.17	Closed loop functions frequency response, with the final gains $K_P = 2.5$ and $K_D = 0.38$. Blue is T, Red is S and Brown is L.	112
5.18	Closed loop functions frequency response for the baseline controller, aka, differential thrust. Blue is T, Red is S and Brown is L.	113
5.19	Gain and Phase of the Closed loop function T, for both actuators suites, The gyroscopic+motors (Blue) and the conventional quadrotor (Red).	115
5.20	Gain of frequency response of the T function (Blue) and of the Gyroscopic+Motor actuation suite (Red).	118
5.21	Closed loop functions frequency response for the high gain controller. Blue is T, Red is S and Brown is L.	119
6.1	Pitch Validation	122
6.2	Roll Validation	123
6.3	Yaw Validation	124
6.4	Stability at ball joint rig	125
6.5	Perturbations in Roll at ball joint rig	126
6.6	Perturbations in Pitch at ball joint rig	126
6.7	Perturbations in Yaw at ball joint rig	127
6.8	Roll angle command tracking at ball joint rig	127
6.9	Vehicle recovery after a disturbance test.	128
6.10	Pitch angle command tracking at ball joint rig	128

6.11	Yaw angle command tracking at ball joint rig	129
6.12	Throttle during flight test. Note that the throttle varies from -50%, zero stick, to 50%, full stick. Hence, around zero, the vehicle is at hover using around half of the power, with the stick in the middle.	130
6.13	Pitch angle during the first flight. Note the scaling of the moment and angular rate.	130
6.14	Roll angle during the first flight. Note the scaling of the moment and angular rate.	131
6.15	Yaw angle during the first flight. Note the scaling of the moment and angular rate.	131
6.16	First Flight: takeoff	132
6.17	First Flight: landing	133
6.18	First Flight, Vehicle at hover.	134
6.19	First Flight, Vehicle at hover.	134
A.1	Motor thrust static test setup	140
A.2	Laser interferometer setup	140
A.3	Phototransistor Circuit	141
A.4	Train of pulses as read by the oscilloscope. The PWM signal sent to the ESC in red, and the laser interferometer signal in blue	141
A.5	Motor torque static test setup	145
A.6	Servo internal model	151
A.7	HS-7950TH servo control Circuit	152
A.8	Servo mapping using a Protractor	152
A.9	Prototype of one arm was build for testing	156
A.10	Servoblock dynamic test	156
A.11	pushpull dynamic test	159
A.12	Balljoint	160
B.1	Two propeller considered attached to the rotor of the motor out-runner motor.	161
B.2	Reference Frames	163
C.1	General Structure of the Simulink Simulation Model	167
C.2	Vehicle Dynamics block. Implementing the equations of motion and the actuator dynamics.	168
C.3	Actuators Block. Implementing the dynamics of each actuator Arm.	168
C.4	Arm 1 Block. Implementing the standard dynamics arm with the rotation to transform it to Arm 1. All the other Arms follow the same layout.	169
C.5	Standard Arm Dynamics. Internal workings of the dynamics of an arm. It implements the individual actuator dynamics, motor and servos, the aerodynamic equations and the rigid body or gyroscopic equations.	169
D.1	Platform technical drawing	171
E.1	SBG IG-500N IMU Technical Specifications	173

E.2 SBG IG-500N IMU Technical Specifications 174

List of Tables

3.1	Hitec servo HS-7940TH technical data	25
3.2	MK3638 motor specifications	27
3.3	Batteries Specifications	29
3.4	chipKIT Max32 specifications	31
3.5	Mass and Inertia around the CG obtained from CAD.	39
3.6	Breckdown of components and their weights	41
5.1	Comparison of the speed of te response of both control actions.	100
5.2	Comparison of the speed of the response of both control actions.	102
A.1	Motor static thrust test environment conditions	142
A.2	Motor static thrust test recorded data part 1	143
A.3	Motor static thrust test recorded data part 2	144
A.4	Motor static torque test environment Conditions	146
A.5	Motor static torque test recorded data part 1	147
A.6	Motor static torque test recorded data part 2	148
A.7	Motor dynamic test recorded data	150
A.8	Servo mapping test recorded data part 1	153
A.9	Servo mapping test recorded data part 2	154
A.10	Servoblock servo dynamic test recorded data	157
A.11	Push-Pull dynamic test recorded data	159

Chapter 1

Introduction

1.1 Background & motivation

In the last decade the Unmanned Aerial Vehicles market has seen major growth figures. Among them, quadrotors have arisen as an architecture with great adoption in the Vertical Take Off and Landing (VTOL) Micro Aerial Vehicle (MAV) segment both in civilian market and military market.

One of the main reasons of the success of the quadrotor lies in its mechanical simplicity, it is only composed by 4 rotors in a cruciform configuration. Electrically powered, its 4 motors usually drive fixed pitch propellers that allow the vehicle to manoeuvre by differential rotor speeds. This allows the vehicle to be both a very simple test platform for a research lab, or to be a tough tactical aid for a soldier in the battlefield.

Although the mechanical construction of a quadrotor is very simple is a very interesting dynamic problem. Hence, in the last decade many researchers have devoted themselves to find ways to exploit its full features. But there exist boundaries on its performance, its manoeuvring capability is upper bounded by the performance of its motors. In other words, the vehicle will be as fast as the motors are, no matter how good the control algorithms are.

Fast transient dynamics in motors demand high peaks in current. Usually, the electrical motors found in quadrotors have its dynamics diminished in order keep the peak current below levels in which it would damage the vehicle circuitry or the motor coils. Then, due to the dependency of the performance of the vehicle on the motors dynamic performance, it exists a clear performance barrier. Hence, it arises the need of searching for new actuation strategies that avoid it.

In order to avoid the performance barrier imposed by the current limit, in this work a new actuation strategy is proposed that breaks the link between motor performance and vehicle performance. The main idea is tilt the propellers in order to use gyroscopic effects to provide fast control action. Thus, the performance of the vehicle will be bounded by the performance of the tilt-

ing devices rather than the performance of the motors.

A novel vehicle implementing this concept has been developed in a joint project with a fellow MSc student Yazan Al-Rihani at Cranfield University. The main areas developed in this study are:

- Design and Vehicle Prototyping
- System Integration and Software
- Modelling and Simulation
- Control System Design

This topics are covered two MSc theses that are complementary one to another. **Al-Rihani's** thesis,[2], titled "*Development of a Dual Axis Tilt Rotorcraft UAV: Design, Prototyping and Control*" covers more the design, prototyping and integration side while the present thesis develops more the modelling and simulation part. The control system design is common to both theses.

1.2 Aims and Objectives

The central goal of this project is to successfully fly a novel actuated tilt rotor vehicle to explore an increased control bandwidth by utilising new, faster, gyroscopic actuation devices. The in order to achieve this, the aims and objectives are:

- **Conception of a new actuation strategy.** Propose a new strategy based on the use of fast gyroscopic moments to complement the current, relatively slower, differential thrusting.
- **Design of the Vehicle.** Design of the vehicle that implements the novel actuator strategy.
- **Prototyping of the vehicle.** Construction of the vehicle implementing the new actuation concept.
- **Modelling and Simulation.** Analysis of the dynamics, mathematical modelling of the novel actuator suite and construction of a high fidelity simulation model for the design of the control system.
- **Design of the Control System.** Design of the control architecture based on a control law and a control allocator to deal with the actuator redundancy.
 - Design of the Control Allocator.
 - Design of the Control Law.
- **Flight Testing of the Platform.** Validating and testing the proposed architecture in real flight of the vehicle.

1.3 Key Challenges

- **No background information on similar vehicles.** There is not any previous project involving a quadrotor using gyroscopic effects for actuation. Hence, it is very challenging to establish, for example, the proper weight ratios due to the increased mechanisms or the proper sizing of the servomotors and propeller to find a successful gyroscopic actuation.
- **COTS and short time-to-fly.** The project was to be finished in less than 4 months, from the first sketch of the concept to the first flight. Hence, there was no time to neither design nor manufacture custom parts. Therefore, the vehicle was designed around off the shelf available parts which could be delivered in very short times. Among these parts there were, for example, the servoblock and servos, whose size determined that of the whole quadrotor. As a consequence, the size and weight of the vehicle was constrained by this ready-made parts, what increased the mass and inertia and did not allow to exploit in full the benefits of the novel actuation strategy.
- **Real time algorithm execution.** All the control architecture was to be designed in order to be able to be executed in real time. That is why the control allocator and the control law had to be simple enough to be executed in a small microcontroller in a relatively short time in order to guarantee acceptable loop frequencies. This constrained the options of the algorithms to be implemented to mostly proportional feedback of variables and precomputed control allocators.
- **Sensor suite.** No external localisation system was available. For the control system only an inertial measurement unit consistent on accelerometers, gyroscopes and magnetometers is used. Although the sensor implemented an Extended Kalman Filter to improve the measurements, only angles and angular rates are used with sufficient guarantees, even though, if operated for a long period of time drift issues can become significant. No position measurements are available indoor, because they are integrated twice from the accelerometer readings, hence, its error builds up with time without bounds. Therefore, the control system had to be constrained to the feedback of the aforementioned angle and angular rate parameters.
- **Multidisciplinary nature of project.** This project is about the design of a totally new kind of vehicle of its own kind. Thus, the nature of the engineering decisions is of multifaceted nature, and usually implying more than one engineering field. The propellers are an example, they have to fulfil both aerodynamic requirements and mass distribution requirements for its dual actuation role as gyroscopes and thrusters. Another example are the servomotors since they have to meet mechanical requirements in terms of stall torque, dynamic requirements in terms of its speed and electrical requirements in terms of its peak current and operating voltage.

1.4 An Overview of the Thesis

The thesis is distributed in the following way. In Chapter 2 a literature review of the relevant modelling and gyroscopic actuation vehicles is presented alongside with a brief primer about control allocation. In Chapter 3, the design of the vehicle is outlined. In Chapter 4, the mathematical modelling of the vehicle and the simulation model is presented. In Chapter 5, the control system designed is presented in two parts, first, the control allocator design and, secondly, the control law design. In Chapter 6 some results of the rig tests and flight test are presented alongside a qualitative validation of the simulation model. Finally, in Chapter 7, the conclusions of the thesis and the future work are presented.

Chapter 2

Literature Review

2.1 Introduction

In this chapter the literature review is carried out. It's divided in two main parts the Modelling and the Control Allocator. In the modelling section an introduction to the background work in conventional quadrotors is given alongside results from other gyroscopically actuated vehicles and system identification procedures for the relevant components. In the control allocation part, first, an introduction to CA is carried out outlining its advantages, and second, a brief summary of existing methods is carried out.

2.2 Modelling

In this section relevant publications for the modelling of the quadrotor dynamics are described.

2.2.1 Quadrotor Analysis

Basic Working Principle.

A quadrotor is a multirotor helicopter vehicle composed by 4 rotors that are placed, usually, in a cruciform configuration. They have seen widespread adoption during the last ten years and are now being used in tactical environments. Examples of commercial quadrotors are the Aeryon Scout and Microdrones md4-1000, both shown in figure 2.1.

A quadrotor is symmetric and its control actions come from the differential speed of the propellers. The basic manoeuvres to control a quadrotor are illustrated in figure 2.2. Basically, to do a Roll or Pitch manoeuvre, the thrust in one propeller is increased and on the opposite one it is decreased, creating a moment from differential thrust. To yaw the vehicle, the strategy is to create an unbalance in the drag torque of the propellers.

The dynamics of this differential propeller speed actuation strategy are given by the dynamics of the motors of the vehicle. In other words, the vehicle will

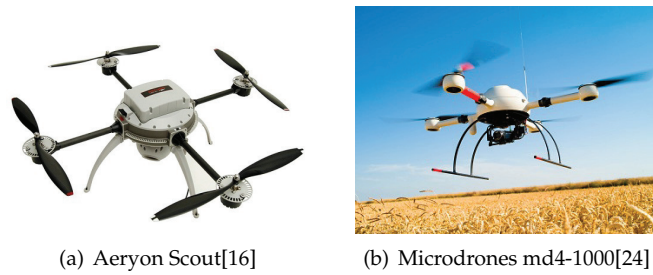


Figure 2.1: Examples of Quadrotors UAVs

manoeuvre as quick (or slow) as its motors are. This imposes a limitation in performance so, to maintain the current peaks within acceptable levels, the transients are rather slow comparing to other actuators such as servomotors.

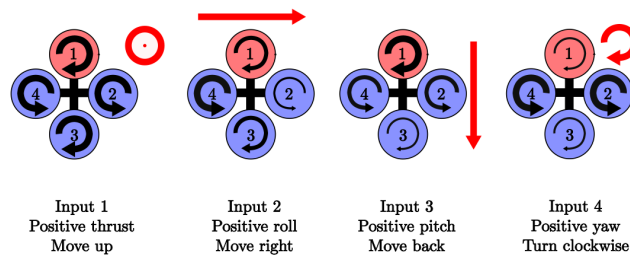


Figure 2.2: Illustration of the quadrotor working principle. Extracted from [37].

General Quadrotor Modelling.

Several publications have been devoted to the analysis of the quadrotor configuration. Among all of them, Bouabdallah [4] provides an early rationalisation and an analysis of the main drivers behind the quadrotor dynamics that is followed by a significant number of other authors.

According to [4] the main effects acting on a quadrotor are:

Effect	Source
Aerodynamic effects	Propeller rotation Blades flapping
Inertial counter torques	Change in propeller rotation speed
Gravity effect	Center of mass position
Gyroscopic effects	Change in orientation of the rigid body Change in orientation of the propeller plane
Friction	All helicopter motion

Aerodynamic Modelling

The aerodynamics of helicopters are described in large detail by J. Leishman in his book, [21], which develops a comprehensive analysis of rotor and helicopter theory. In this project several results from the momentum theory will be used to characterise the propeller behaviour.

2.2.2 Tilt Rotor Gyroscopic Actuation

The main aim of this project is to increase the speed or bandwidth of the control system of a quadrotor by increasing the speed or bandwidth of its actuators. Efforts to increase the bandwidth of the actuators of the control system have been conducted using Control Moment Gyroscopes, the same way as spacecraft govern their attitude, see [22]. In this work the authors merge a thrust vectoring approach with increased bandwidth including additional flywheels to use as CMG.

Gary R. Gress [13] came up with the idea of using Opposed Lateral Tilting as a means of using the gyroscopic effects for governing the pitch attitude of his aircraft, using the propellers as gyroscopes. In his latest work [14] provides an overview of the Opposed Lateral Tilting philosophy. In this work the author provides, through a simplified modelling, evidence of the feasibility of the gyroscopic actuation for governing pitch attitude. In [14] OLT is proved to give higher control authority than other means of actuation such as vaned fans.

In an independent work [20] conducted a more detailed modelling of a platform based on the OLT strategy and provide evidence of the effectivity of this technique in simulation. Later the same group, [1], these concepts are put into practice into the vehicle T-Phoenix UAV, providing a detailed model and a control strategy for hovering, demonstrating experimental evidence of the feasibility of the OLT strategy.

In the work [26] the authors provide also a survey of OLT technology and a more in depth modelling of the tilting phenomena allowing for distinct angular velocities and tilt angles of the two thrusters.

From all these promising attempts and published results it can therefore be concluded that the control bandwidth of the conventional quadrotor can be significantly increased by the implementation of controlled gyroscopic moment capabilities.

2.2.3 Component System Identification

Essential to the success of the in the veracity of the simulation model is to have a good approximation of the individual actuator dynamics that create the actions onto the airframe. In the dual axis tilt rotorcraft the independent actuators to be identified are the motors and the servomotors.

RC Servo Modeling

The rigid body equations that model the gyroscopic forces and moments are based on the knowledge of the angles, angular rates and angular accelerations. Hence, it is essential to the veracity of the simulation model to have a good approximation of the servomotor dynamics that create this motions. In the work [36], by Wada et al, an internal model of a similar servomotor to the ones used in this project is described, and a system identification approach is proposed.

Brushless + ESC system ID

In the work by [28] a breakdown of the dynamics of the different component of a brushless DC and Speed controller are described. Although its results are not directly applicable to this project, it provides insight in the internal dynamics that can be expected from a system of this kind, which are helpful for the understanding and the system identification of the motors and drivers used in this project.

2.2.4 Equations of Motion

In order to model the motion of the vehicle, the full nonlinear 6 Degree of Freedom equations of motion for a rigid aircraft are used. These equations are described in detail in books like the ones from Cook [7] and Stengel [34].

2.3 Control Allocation

2.3.1 Introduction

Control Allocation is a mathematical tool to distribute a given control command into the individual inputs of a suite of effectors. Hence, it is very useful for overactuated systems, such as the vehicle of this project.

According to O. Harkegard, [15], Control Allocation, in the context of overactuated systems, allows to split the control system design in the following two steps:

- Design a control law specifying which total control effort to be produced (net torque, force, etc.).
- Design a control allocator that maps the total control demand onto individual actuator settings (commanded aerosurfaces deflections, thrust forces, etc.).

The control system can, then, be structured as it is shown in figure 2.3. According to O. Harkegard, [15], the control system is made up by a control law, specifying which total control effect, v , should be produced, and a control allocator, which distributes this control demand among the individual actuators, u . In the system, the actuators generate a total control effect, v_{sys} , which determines the system behaviour. If the control allocation is successful, $v_{\text{sys}} = v$.

Harkegard, [15], suggests several advantages of this approach:

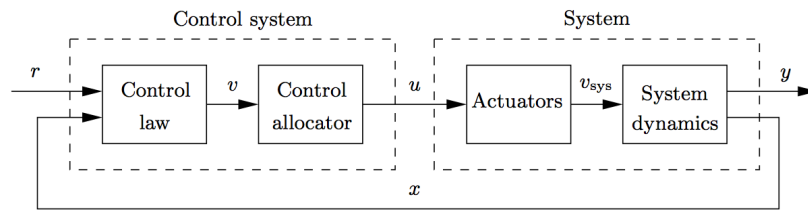


Figure 2.3: Control system structure when control allocation is used. Reproduced from Harkegard, [15].

- One benefit is that actuator constraints can be taken into account. If one actuator saturates, and fails to produce its nominal control effect, another actuator may be used to make up the difference. This way, the control capabilities of the actuator suite are fully exploited before the closed loop performance is degraded. The way the system performance degrades can also be affected. For example, in flight control, it might be crucial to maintain yaw control performance to avoid yaw departure, while roll control may be less important.
- Controller reconfiguration can be performed if the effectiveness of the actuators change over time, or in the event of an actuator failure, without having to redesign the control law.
- Actuator utilisation can be treated independently and can be optimised for the application considered. The actuator redundancy can be used for several purposes. Most commonly, the extra degrees of freedom are used to optimise some secondary objective, like total aerosurface deflections, drag, wing load, or radar signature in aircraft applications.
- Filtering can be included in the control allocation procedure, to obtain different control distributions among the actuators at different frequencies. That is, efficient in generating slow responses.

2.3.2 Control Allocation Methods

Daisy Chaining

Daisy Chaining ([6], [11]) is based on dividing the effectors into groups which are to generate a given virtual command such that they in total generate, successively, the demanded control effort. The main idea is to try to generate the control demand with the first group of effectors, with the others remaining at idle. If the total virtual command is not met, then, the second group of actuators is used, if, then, total command is not attained the third group of actuators is used and so on in a successive process.

Direct Control Allocation

Constrained Control Allocation or Direct Control was presented by Durham [10] as a way to maximise the use of the effectors ability to provide the de-

manded virtual control command. The selection of the effectors is made unique by including the geometry of the constraints of the effectors. Hence, it can maximise the use of the capabilities of the effectors.

Optimal Control Allocation

Optimal control allocation is based on the minimisation of a given cost function. Usually a quadratic norm is used, see [5] and [12]. A typical example of this approach is to use the 2-norm, yielding the problem:

Find \mathbf{u} such that:

$$\min_{\mathbf{u}} \frac{1}{2} \mathbf{u}^T \mathbf{u} \quad \text{subject to} \quad \mathbf{v}_c - B\mathbf{u} = 0 \quad (2.1)$$

Which has an analytical solution given by:

$$\mathbf{u} = B^T (BB^T)^{-1} \mathbf{v} \quad (2.2)$$

This analytical solution enables to exploit several advantages such as fast computation, and the introduction of weights allows the designer to shape the response. An application of this method to multi-rotor vehicles can be found in [9]. More on this will be developed on the control system design chapter.

Pseudoinverse Redistribution

The Pseudoinverse Redistribution method, see Jin [18], is an attempt to cope with the saturation of the actuators. The main strategy is first, to calculate a first solution based on the Pseudoinverse method. Second, to separate the saturated inputs from the others and set them to their maximum/minimum deflections. Third, to recalculate the problem by calculating a new Pseudoinverse with the unsaturated inputs to obtain the demanded control minus the actions obtained from the saturated inputs. If in this step new inputs are saturated the process is repeated again until a valid solution is found or no unsaturated controls are left.

This method results in a relatively small computational demand while in can deal with the saturation of the actuators. And, although it does not find an optimal solution, usually they are satisfactory for engineering purposes, see Jin [18].

Chapter 3

Vehicle Description

3.1 Introduction

This thesis stems from a project to design a novel dual axis tilt quadrotor that uses gyroscopic effects to explore an increase in the performance relative to a conventionally actuated quadrotor. This project is developed in two thesis, one by Y. Al-Rihani, [2], which develops the design and prototyping, and the present thesis which develops the mathematical model and the control system design of the new vehicle.

To carry out the mathematical model and the control design it is essential to give a picture of the designed vehicle. Hence, in this chapter a brief overview of the design procedure of the dual-axis tilt quadrotor is carried out. The focus is mainly on the development of the tilt mechanism and the designed parts. The main objective is to give an idea of the overall design. This chapter is adapted from Al-Rihani's Thesis,[2], the interested reader is referred to it for full information on the details of the design.

3.2 Requirements and Baseline Specifications

The requirements were to develop a novel quadrotor platform with two axes tilting capability in each rotor, to provide an agile actuation capabilities to the vehicle. Hence, the control inputs will be increased from 4 to 12.

Different design considerations are to be met in this design such as:

- The required tilting is up to $\pm 20^\circ$ for each axes with the possibility of tilting simultaneously and independently in both axes.
- Weight and inertia are to be minimal for agile maneuvering.
- Capable of carrying 500 gram or more of payload such as a camera system or sensors.
- Flight endurance of 10 minutes or more.

3.3 Tilting Rotor Design

3.3.1 Tilting Arm Design

The design is based around a new off the shelf component from servo city, it is the Servoblock [30] shown in figure A.9, it is a standard size servo holder aluminium bracket designed specially to increase the servo capability to carry lateral loads by transferring the load to the holding structure. It has one small bearing on the front bracket and a frame that attaches it to the servomotor.



Figure 3.1: Servo Block [30]

In figure 3.2 the design schematic is presented. The arm is designed such that one servoblock (1) will be used to rotate the whole arm, the arm is a round aluminum tube (4) that carries two brackets(6) that hold the second servo (2). The second servo tilts the motor holding bracket (5) using a push-pull arm (3).

Refer to Al-Rihani's thesis,[2], for a full description of the design procedure and the rationale behind this design. Based on the tilting mechanism concept that was selected, the following components were chosen.

ServoBlocks

The design was build around using Servoblocks from servo city [30] shown in figure 3.3(a), it is a combination of servo brackets, designed specially to increase the servo capability to carry lateral load by transferring the load to the brackets by one bearing in the front bracket. The attached frame is aligned with the servo axes. The servoblocks work with either a standard size Hitec or Futaba RC servos.

The rotor arm is chosen to be a 0.5" diameter hollow aluminium tube, as shown in figure 3.3(c), with 8" length. It will be mounted to the servoblock

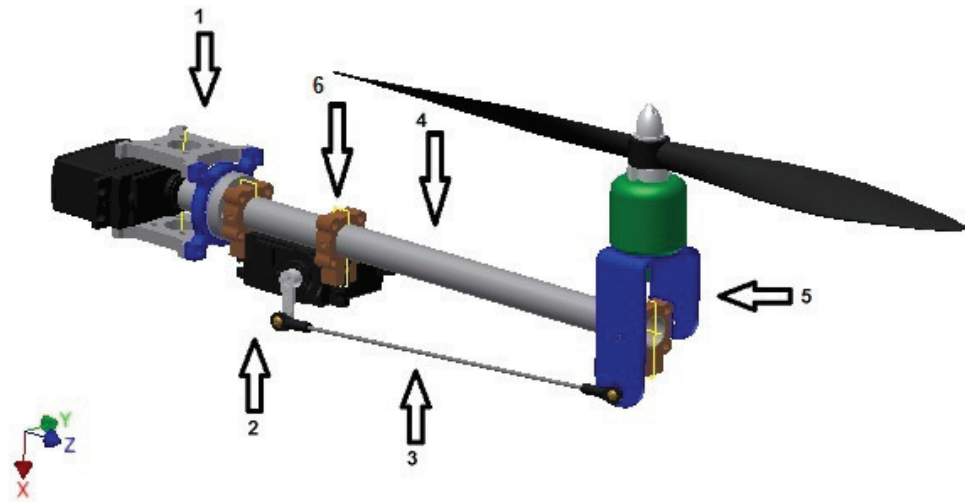


Figure 3.2: Tilting Arm Design

adapter using a compatible 0.770" aluminium tube clamping hubs as shown in figure 3.3(b). On the other end of the aluminum arm, an adapter from xaircraft [38] shown in figure 3.3(d) will be fixed to create a tilting swivel joint with the motor bracket mount.

Figure 3.4 shows the whole assembly design of these parts. Refer to Al-Rihani's thesis,[2], for a full description of the selection procedure.

Push-Pull Arm

As can be seen in figure 3.4, the responsible servo for the tilting the rotor outward and inward is near the central body. And to transfer the movement from the servo arm to the motor bracket at the other end of the arm, a push pull arm is needed for this purpose.

Three main parts were selected to create the push pull arm shown in figure 3.5(a) , a 4 mm carbon fiber tube, on both ends a threaded couplers shown in figure 3.5(b) and a M3 metal Clevis shown in figure 3.5(c), this will the flexibility to trim the arm length . Refer to Al-Rihani's thesis,[2], for a full description of the selection and design procedure.



Figure 3.3: Tilting Arm Parts



Figure 3.4: Tilting arm mechanism components



(a) Push Pull Arm



(b) Threaded couplers



(c) M3 metal Clevis

Figure 3.5: Push-Pull arm and its components

Servos

Servoblocks are designed to work with Futaba and Hitec RC servos only. The Hitec servo HS-7940TH shown in figure 3.6 was found to deliver the required torque demands while maintaining a very good speed. Table 3.1 shows the technical data for this servo. Refer to Al-Rihani's thesis,[2], for a full description of the dimensioning procedure.

Specifications	
Motor Type	Coreless
Bearing Type	Dual Ball Bearing
Speed (sec/ 60°) 6.0V/7.4V	0.07 / 0.06
Torque (kg/cm) 6.0V/7.4V	13.0 / 16.0
Size in Millimeters	39.88 x 20.07 x 38.10
Weight (g)	68.04

Table 3.1: Hitec servo HS-7940TH technical data

The servo will be used to rotate the arm at the servoblock in the vehicle central body and to be mounted on the each arm, closest as possible to the central body to tilt the motor-propeller set outward and inwards using a push pull arm.



Figure 3.6: RC Servos

3.4 Airframe, Powerplant and Avionics

3.4.1 Propulsion

The Propulsion system composed of three main units: the propeller, the motor and the motor speed controller ESC.

Propeller

The master airscrew 3 blade 12 x 6 propeller was found to be the most suitable from the options available in the market. Because it provided the desired thrust while maintaining good qualities at small advance ratios and a symmetric distribution of the inertia, necessary to avoid high frequency vibrations. A puller propeller shown in figure 3.7. Refer to Al-Rihani's thesis,[2], for a full description of the selection procedure.



Figure 3.7: Masterairscrew 12 x 6 3-blade [23]

Motor

The market has many options of outrunner brushless motors that can drive this size of propellers, to deliver needed thrust. The MK3638 Brushless motor from MikroKopter [25] was considered, it is designed to run propellers of 10" - 14" and can deliver a maximum power of 350 W, which is close to the needed excess power. The Technical specifications are listed in table 3.2 as provided by the manufacturer, and a picture of the motor is shown in figure 3.8. Refer to Al-Rihani's thesis,[2], for a full description of the selection procedure.

Electric Speed Controller (ESC)

The Electronic speed controller that was selected is Roxxy BI Control 930-6 from Robbe [29] shown in figure 3.9, it has a continuous current of 30A, and can be connected to up to 6 LiPo cells, and weights 29g. Refer to Al-Rihani's thesis,[2], for a full description of the selection procedure.

3.4.2 Sensors

A set of sensors are essential to close the control loop. The sensors selected are embedded in one unit as an Inertial Measurement Unit (IMU).

Inertial Measurement Unit IMU

There is a wide range of options regarding IMU equipment available in the market, all of them show similar performance figures. The SBG IG-500N, shown in figure 3.10 from SBG Systems [35], was already available in the lab. It is a high grade MEMS based system that has 3 Axis Gyroscopes, 3 Axis Accelerometers, 3 Axis Magnetometers, GPS receiver, Temperature Sensors and Pressure sensors. With all those sensors, the IG-500N has an embedded Extended Kalman Filter to fuse sensors data for more precision at a maximum frequency of 100 Hz. As its specifications matches the performance and precision required, it was used for the prototype. Refer to Al-Rihani's thesis,[2], for a full description of the sensor. Detailed technical specification can be found in the appendix E.



Figure 3.10: SBG IG-500N [35]

3.4.3 Power Source (Battery)

Motors Battery (4 cell Lipo)

The needed capacity depends on the required flight time. Using using a four cell lithium polymer battery, (14.8V to 16.8V) with a capacity of 5000 mAh, will last for around 13 minutes of hovering.

The selected battery to power the motors is a Vislero V2 14.8V 4S1P 5000mAh 20C shown in figure 3.11, the selected battery is four cells connected in parallel in flat package, it weights 520g, with capacity of 5000 mAh, and a discharge rate of 20C allowing for a maximum continuous withdraw of 100A. A summary of specifications are listed in table 3.3. Refer to Al-Rihani's thesis,[2], for a full description of the sizing and selection procedure.

Servos Battery (2 cell Lipo)

The second battery to power the servos and electronics is a 2 cell Lipo battery. Using a two cell lithium polymer battery, (7.4V to 8.4V) with a capacity of 3200 mAh, the Battery will last for around 12 Minutes.

The selected battery to power the servos and the avionics is 7.4V 2S1P 3200mAh 25C. It is two cells connected in parallel and was modified to flat package to reduce inertia. It weights 185g, with capacity of 3200 mAh, and a discharge rate of 25C allowing for a maximum continuous withdraw of 80A. The specifications are listed in table 3.3. Refer to Al-Rihani's thesis,[2], for a full description of the sizing and selection procedure.

	Motors Battery	Servos Battery
Voltage	14.7V	7.4V
Cell arrangement	4S1P	2S1P
Discharge rate	20C	25C
Capacity	5000mAh	3200mAh
Weight)	520g	185g

Table 3.3: Batteries Specifications



Figure 3.11: 4 cell flat battery

Battery Holder

Mikrokopter Battery Holder [25] shown in figure 3.12 was selected to carry a flat Lithium polymer battery. This holder weights 45 gram. It is made of light carbon fiber sheets, and is mounted using a rubber dampers to minimize vibrations.

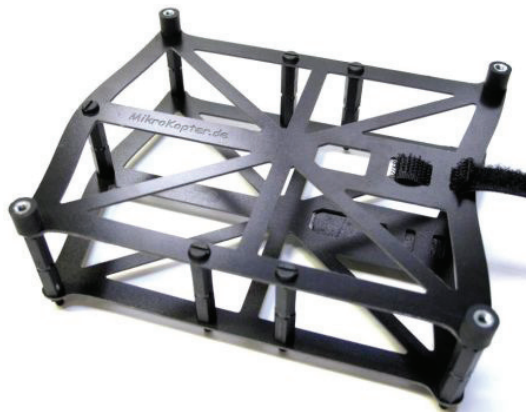


Figure 3.12: Mikrokopter Battery Holder

3.4.4 Flight Computer

Microcontroller

The vehicle was fitted with with the chipKIT Max32 shown in figure 3.13 from DIGILENT [8]. It is based on the Arduino open source hardware prototyping platform but it uses PIC32 microcontroller instead of ATmega2560 microcontroller for better performance as it is a 32bit microcontroller that runs at 80Mhz. It has 4 serial ports that are needed to communicate with the IMU, RC receiver, Servo controller and through the wireless to the Ground station. This board is fully compatible with Arduino codes and libraries, hence taking advantage of the huge community of developers around Arduino. Technical specifications are listed in table 3.4. Refer to Al-Rihani's thesis,[2], for a full description of the selection procedure.

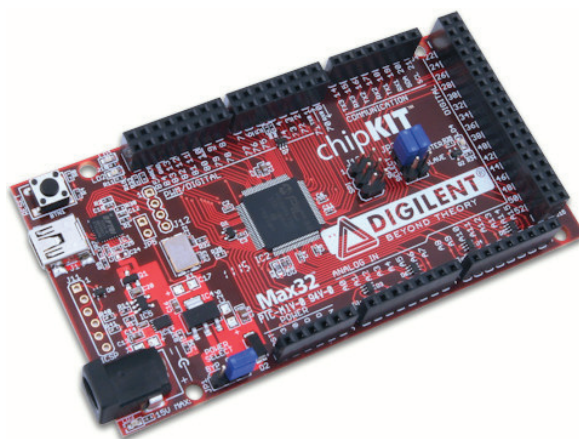


Figure 3.13: chipKIT Max32 Prototyping Platform [8]

Specifications	
Microcontroller	PIC32MX795F512L
Flash Memory	512K
RAM Memory	128K
Operating Voltage	3.3V
Operating Frequency	80Mhz
Typical operating current	90mA
Input Voltage (recommended)	7V to 15V
Input Voltage (maximum)	20V
I/O Pins	83 total
Analog Inputs	16
Analog input voltage range	0V to 3.3V
DC Current per pin	+/-18mA

Table 3.4: chipKIT Max32 specifications

Servos controller

To drive 8 servos and 4 brushless motors, the flight computer needs to dedicate 12 pins to generate the required PWM signals, instead, the decision was to use the Propeller Servo Controller USB from parallax [27]. Refer to Al-Rihani's thesis,[2], for a full description of the reasoning behind the selection and the advantages of this approach.

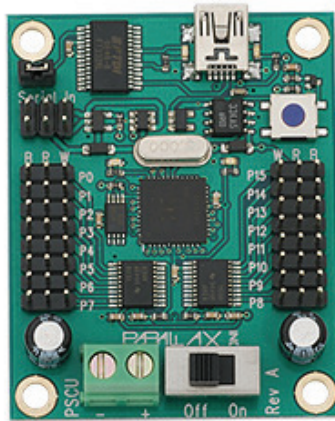


Figure 3.14: Propeller Servo Controller USB

3.4.5 Wireless Communication

Two types of wireless communication is needed between the vehicle and ground. Those are:

- Wireless Data link. This is needed to send and receive data from the ground station computer to the Flight computer.
- Radio Control Transmitter-Receiver kit. This is the typical manual way of controlling the aircraft just like a traditional RC hobby aircraft.

Refer to Al-Rihani's thesis,[2], for a full description of the selection procedure regarding the wireless communications.

Wireless Data link

The Xbee Pro module from Digi [17] was chosen as a data link between the vehicle and the Ground station computer. The xbee pro XBP24-BZ7PIT-004 module from Digi is shown in figure 3.15(a) . This transceiver module has 50mW output power, with theoretical range of 1 mile.

The Xbee Explorer Regulated board from Sparkfun [32] shown in figure 3.15(b) was selected to connect the xbee module on Vehicle to the The chipKIT Max32 through the serial port.

And a Xbee Explorer USB board also from Sparkfun [32] shown in figure 3.15(c) was selected to connect the xbee module on Ground to the Ground station laptop through the USB port.

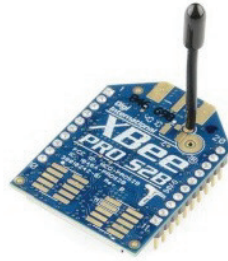
Radio Control

For manual control a radio control set, the Spektrum [33] DX6i transmitter and its AR6210 receiver, was chosen . It operates at a frequency of 2.4GHz. The system has a 6 channel, the main four channels are for controlling Throttle, Pitch, Roll and Yaw, and the other two are for controlling other functions.

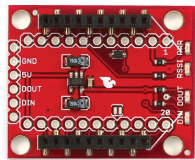
3.4.6 Final Mechanical Design

The design was done using Autodesk Inventor software [3] in three steps. Refer to Al-Rihani's thesis,[2], for a full description of the design procedure. These steps are:

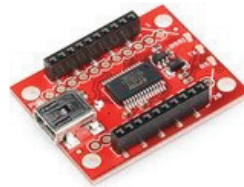
- All selected components were 3D modelled precisely.
- Custom design for some parts.
- Building a full 3D model for the whole vehicle and study different arrangements of the components to get the best CG location, Inertia and electronics layout.



(a) xbee pro [17]



(b) XBee Explorer Regulated [32]



(c) xbee Explorer USB[32]

Figure 3.15: Wireless Data Communication kit



(a) Spektrum AR6210 receiver [33]



(b) Spektrum DX6i transmitter [33]

Figure 3.16: Radio Control kit

3.4.7 Custom designed parts

Refer to Al-Rihani's thesis,[2], for a full description of the design of the parts.

Motor Bracket

In Quadrotors, the Motors are mounted directly in a way or another, to the arm. In this platform the motors need to be mounted to the vehicle arm but also need to be tilted. So this bracket shown in figure 3.17 was designed to carry the brushless motor while giving it the ability to tilt around the joint axis, see figure 3.23. The tilt angle is controlled by the push pull arm connected to the bracket.

The roles of this bracket can be summarised in the following points:

- To carry the motor.
- Create a swivel joint.
- Part of the push pull mechanism to tilt the rotor.

The bracket was manufactured from 2 mm Aluminium sheet metal, and weights 14g. For more details see Al-Rihani's thesis, [2].

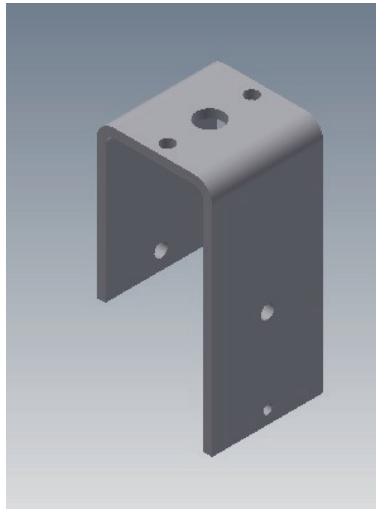


Figure 3.17: Motor bracket

Central Plates

The main structure of the central body of the vehicle is composed of two identical central Plates fixed above and below the servoblocks using precision drilled holes in a sandwich configuration. Figure 3.19 shows this arrangement. The resulting structure is to be strong against bending moments created by the thrust forces at the rotor ends and landing gear shocks.

The central Plate is shown in figure 3.18. The plates are made of 3 mm carbon fibre, and weight 102g. The landing gear will be attached to the lower plate and on top of the upper plate the electronics and battery holder will be mounted. Refer to Al-Rihani's thesis,[2], for a full description of the design procedure.



Figure 3.18: Central Plate

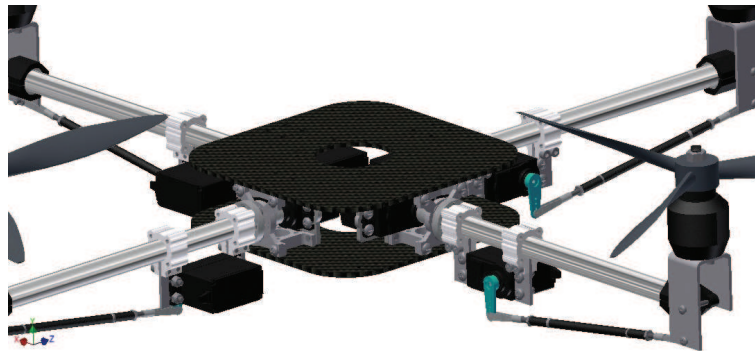


Figure 3.19: Central body structure

Landing Gear

Mikrokopter [25] large landing gear shown in figure 3.20 was selected, it carries the central body at a high of 160 mm above ground, together with the other components the propellers will be at a height of 270 mm above ground.

After testing the landing gear on the vehicle, it was noted that the vehicle wobble easily with any disturbance. So extra carbon fibre rods were used to stiffen the landing gear.



Figure 3.20: Mikrokopter landing gear

3.4.8 Description of the Design

As mentioned in section 3.3 the tilting rotor design is to use a servoblock and a Hitec servo HS-7940TH at the central body for each arm, the arrangement of the servoblocks in the central body can be seen in figure 3.21. For each arm, a 0.5" diameter hollow aluminum tube is to be fixed to the servoblock adapter by using a 0.770" aluminum tube clamping hub, and by using another clamping hub, the other Hitec HS-7940TH servo was mounted to both clamping hubs as shown in figure 3.22. Refer to Al-Rihani's thesis,[2], for a full description of the design and sizing procedure.

On the other side of the arm (Aluminum tube), a plastic mount from xaircraft was fixed, the internal diameter of the adapter is 16 mm, and the aluminum tube is 12.7 mm, so a custom made reduction aluminium tube was used inside plastic mount to firmly fix it to the arm. The plastic mount was used to carry the motor bracket but giving it the ability to rotate freely as shown in figure 3.23.

The tilting of the motor and its mounting bracket was controlled by pulling and pushing from the Hitec HS-7940TH servo, by means of a push pull arm and as seen in figure 3.22 the push pull arm and the motor bracket are designed to mimic the servo arm movement, i.e the servo arm rotation angle will be translated to an equivalently tilting angle of the motor adapter.

3.4.9 Electronics layout

The Avionics components such as the IMU, the Flight computer, wireless Data link, RC receiver and the Servo Controller were mounted on the upper central plate. The IMU, flight computer and servo controller were mounted using an 8 mm rubber damper to isolate any vibration from those components. The ESCs were mounted on the lower central plate, next to the servoblocks. Figure 3.24 shows this arrangement. Refer to Al-Rihani's thesis,[2], for a full description of the avionics and software systems.



Figure 3.21: Servo blocks in the central body

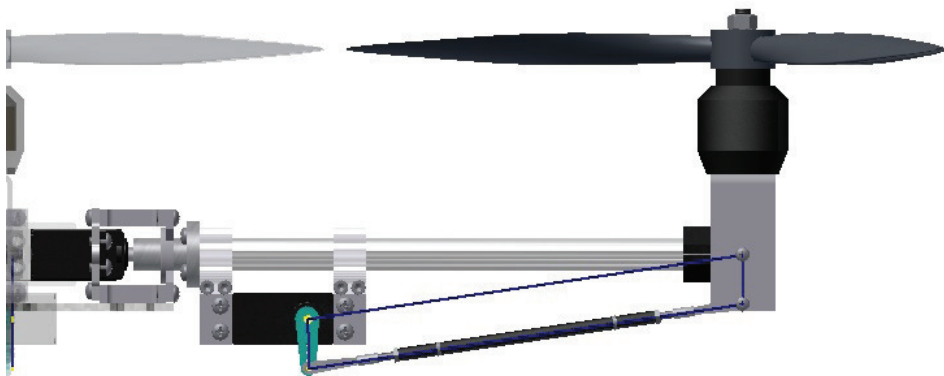


Figure 3.22: Tilting mechanism



Figure 3.23: Assembled Arm

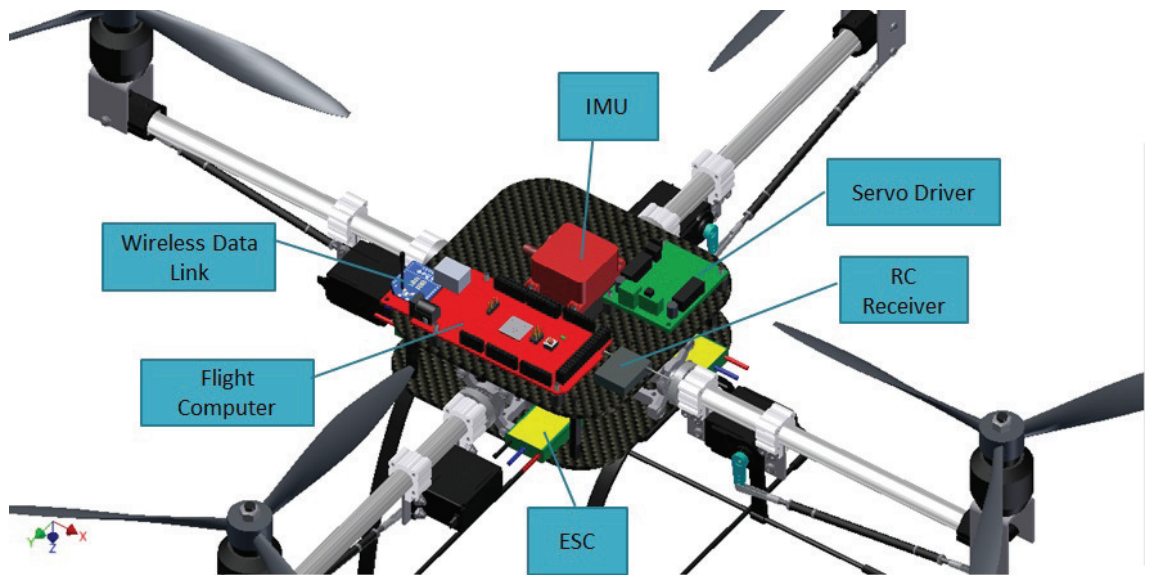


Figure 3.24: Avionics components arrangement

3.4.10 CG location

Several locations for the battery were considered, see Al-Rihani's thesis [2], for the details. Finally the most appropriate was found to be on top of the vehicle according to inertia and CG position.

From the CAD software, the inertia tensor obtained is listed in table 3.5. The CG is almost at the IMU base as shown in figure 3.25(a). According to the CAD software the difference between the CG and the IMU reference point is 14.7 mm in Z. Hence with reference to the IMU position the CG is located at 0 x, 0 y, and +14.7mm in z. See figure 3.25 for the illustration of the CG position. Refer to Al-Rihani's thesis,[2], for a full description of the rationale behind the CG location decision.

Mass	2.968 Kg
Ixx	49827 kg mm ²
Iyy	48993 kg mm ²
Izz	82777 kg mm ²
Ixy	12 kg mm ²
Ixz	35 kg mm ²
Iyz	295 kg mm ²

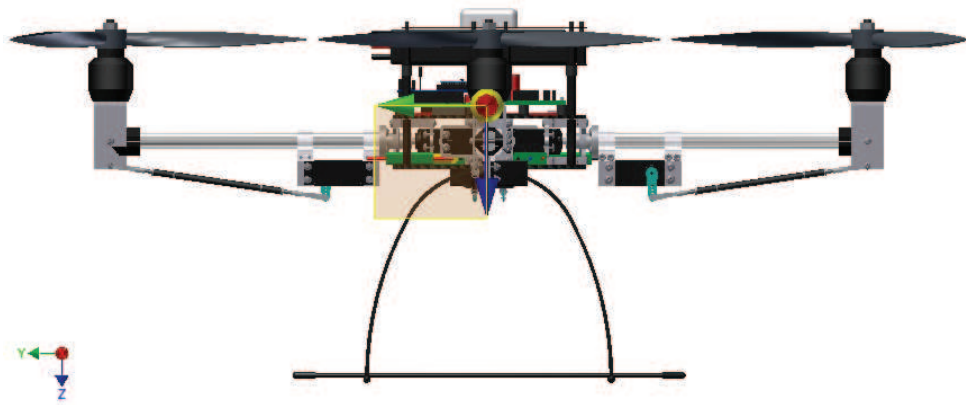
Table 3.5: Mass and Inertia around the CG obtained from CAD.

3.5 Mass Breakdown

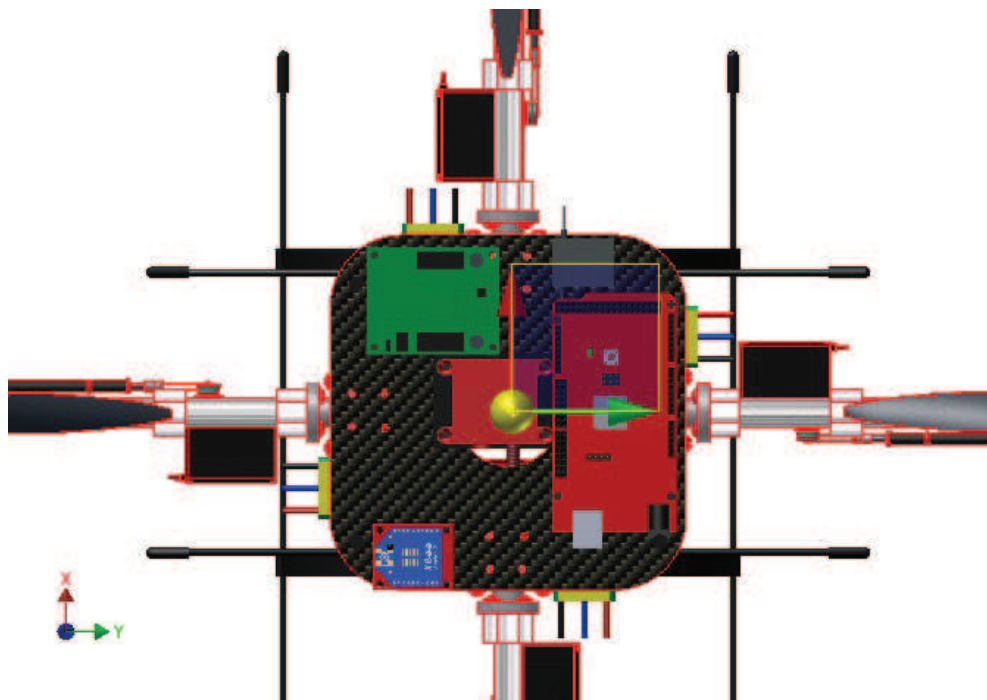
After the final design has been completed, all components have been selected, and the designed parts were manufactured the measured weight of each of the components that were selected and manufactured are shown in table 3.6. With a total mass of 3057g.

3.6 Prototype

The UAV first prototype was build according to the detailed design. As seen in Figure 3.26 the tilting mechanism shown as designed on the CAD software and the final prototype. Similarly, The electronics layout can be seen in figure 3.27 and the whole UAV can be seen in figure 3.28 in both 3D model and the prototype. Refer to Al-Rihani's thesis,[2], for a full description of the design. In appendix D a 3 view drawing of the vehicle is presented.



(a) Vertical CG location



(b) Vertical CG location

Figure 3.25: CG Location.

Component	Accurate weight (g)
IMU(SBG IG-500N)	44
IMU voltage level converter	10
Flight Computer (chipKIT Max32)	36
Servo controller	19
GPS antenna	38
Wireless (xbee pro)	2
Xbee explorer regulated	2
BATTERY (LiPo 14,8V 5350mAh)	504
BATTERY (LiPo 7.4V 3200mAh)	185
RC receiver(Spectrum)	5
Harnesses and connectors	243
Motor with adapter(MK3638)	4x 125
Propeller (3-blade 12 x 6)	4x 45
ESC (Roxxy BL 930-6)	4x 32
Motor holding bracket	4x 14
servoblock	4x 25
servo (HS-7940TH)	8x 66
Adapters and holders	4x30
Aluminum Arm	4x 15
Clamping hub	8x 9
Push Pull arm	4x 9
Arm tip mount	4x 5
Center plate	2x 100
Landing gear	55
Battery holder	41
Total	3057

Table 3.6: Breakdown of components and their weights

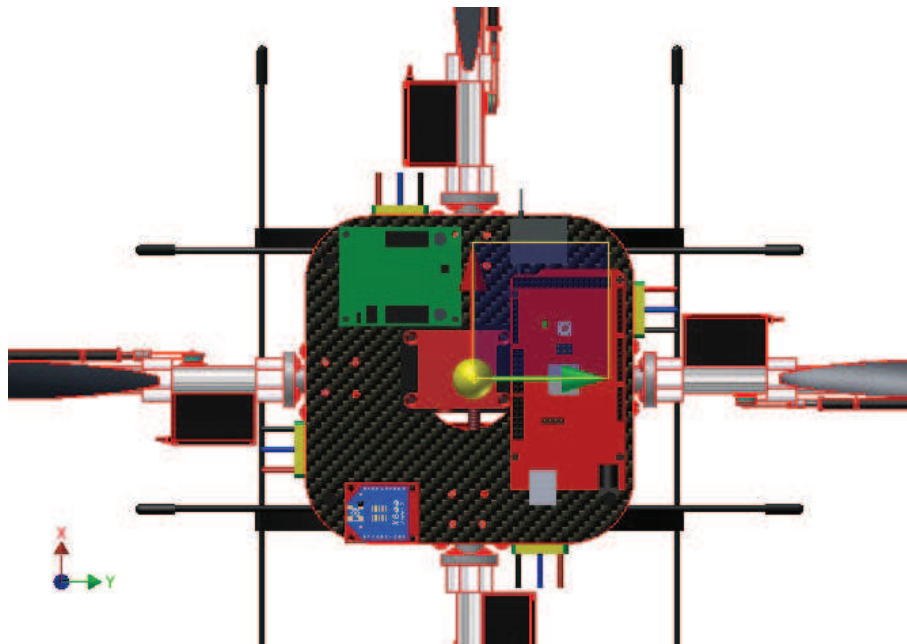


(a) 3D model

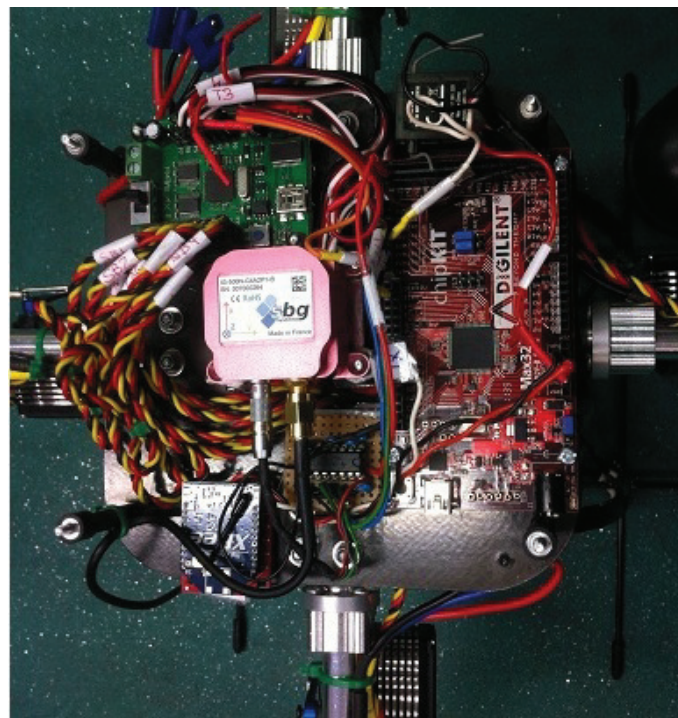


(b) Prototype

Figure 3.26: Dual axis Tilt rotor Arm mechanism



(a) 3D model



(b) Prototype

Figure 3.27: Electronics layout



(a) 3D model



(b) Prototype

Figure 3.28: Dual axis Tilt rotor UAV

Chapter 4

Modelling

4.1 Introduction

In this section the modelling of the most relevant actions on the vehicle is carried out. The two main actions on the vehicle are the gyroscopic effects and the aerodynamic thrust and drag torque.

The model of the vehicle objective is to provide support to the control system design. Hence, since the control system design aim is to develop a stabilising controller for hover or quasi-hover, i.e., small advance velocities, all the actions related to the advance of the vehicle are neglected, such as airframe aerodynamic drag and propeller angle of attack.

To model the gyroscopic effects a development of the Rigid Body equations of the tilting propeller is carried out. Starting from the Euler equation of motion, the reaction moments are developed as a function of the motion of the vehicle, the servoblock motion, the pushpull motion and the motor motion.

In order to accurately characterise the propeller Aerodynamic Thrust and torque, experiments are carried out. From the data gathered it is found that the propeller is accurately modelled by a constant thrust and torque coefficient.

To assess the suitability of the motor chosen an analysis is carried out quantifying its performance and efficiency is carried out. The motor controller, ESC, is also analysed to determine whether it's linear enough.

Fundamental to the development of the control law is the accurate model of the dynamic behaviour of the motors, hence, a series of experiments are carried out to find its transfer function in the frequency domain.

The rigid body equations give the moments of the exerted on to the vehicle based on the motion of the motion of the vehicle, the servoblock motion, the pushpull motion and the motor motion. Hence it is critical to model with high veracity the dynamics of the push pull and the servoblock servo. For this reason, a series of experiments are carried out, to identify a the transfer function

of the servomotors in the frequency domain.

Finally, everything is put together in the simulation model, in order to have a good basis onto which design the control system.

4.2 Rigid Body Modelling

The moments created by the propellers when they are tilted are modelled using the Euler equation of motion:

$${}^i\mathbf{M} = \frac{d}{dt} {}^i\mathbf{L} = {}^i\mathbf{I}^i\boldsymbol{\alpha} + {}^i\boldsymbol{\omega} \times {}^i\mathbf{I}^i\boldsymbol{\omega} \quad (4.1)$$

where ${}^i\mathbf{M}$ is the moment in the centre of gravity, ${}^i\mathbf{I}$ is the inertia tensor in the reference frame i respect to the CG, ${}^i\boldsymbol{\omega}$ is the total angular velocity and ${}^i\boldsymbol{\alpha}$ is the total angular acceleration of the body in the reference frame i , i.e. ${}^i\boldsymbol{\alpha} = \frac{d}{dt} {}^i\boldsymbol{\omega}$.

The equation 4.1 establishes, then, the relationship between the rotation motion of a spinning body and the actions (moments) applied onto its Centre of Gravity.

An analysis carried out trading off a 2-blade propeller against a 3-blade propeller showed that the 2-blade assembly induced high frequency vibration due to the asymmetry in the mass distribution, i.e. the Inertia tensor was not diagonal and $I_{xx} \neq I_{yy}$. For the details of this analysis see appendix B. Finally a 3 blade propeller was selected.

As the Rotating Assembly is, therefore, symmetric, the inertia tensor will be the same regardless of the orientation of the x and y axes, provided that z is along its symmetric axis.

In other words, the Inertia tensor will be the same for a frame attached to the Rotating Assembly and spinning with it (attached to the prop) or as if it is referred to a frame that is not spinning with it (motor stator) but that has the z axis in the same direction.

This removes the rotation asymmetry that causes the vibration aforementioned before and simplifies the analysis, since it removes the need for another frame attached to the propeller. The inertia tensor will then be:

$$\text{Rotor } \mathbf{I} = \text{Stator } \mathbf{I} = \begin{bmatrix} I_{xx} & 0 & 0 \\ 0 & I_{yy} & 0 \\ 0 & 0 & I_{zz} \end{bmatrix} \quad (4.2)$$

Hereafter the Reference Frame 3 will be the frame attached to the motor stator, and will be referred to also as the Rotating Assembly or Spinning Body Frame.

Frames Used

Three non inertial reference frames are used to describe the rotating motion of the spinning assembly. These are illustrated in figure 4.3.

- Reference Frame 1 (x_1, y_1, z_1) attached to the Vehicle.

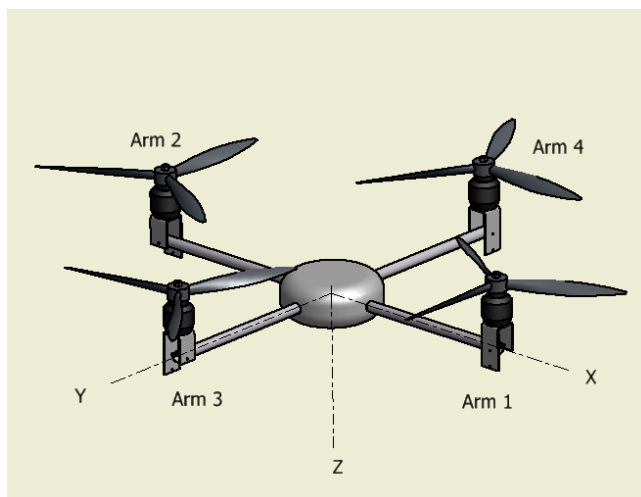


Figure 4.1: Body axes reference frame and arm numbering.

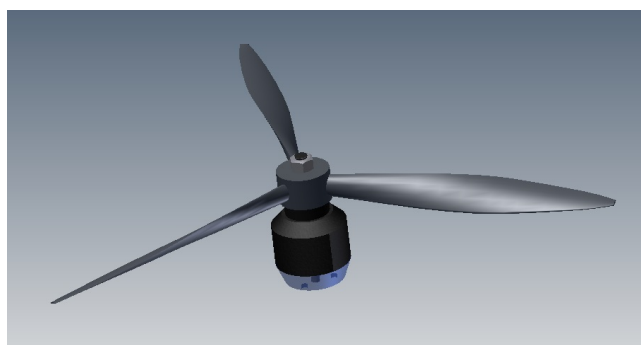


Figure 4.2: Spinning body studied, i.e. propeller+motor rotor.

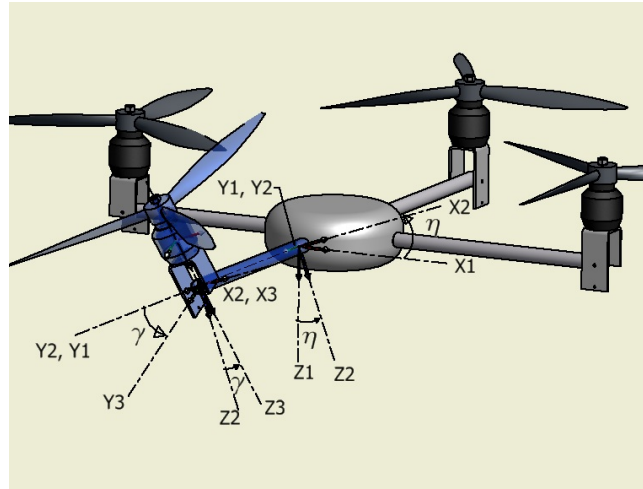


Figure 4.3: Reference frames used in the development.

- Reference Frame 2 (x_2, y_2, z_2) attached to the Servoblock, i.e. to the arm.
- Reference Frame 3 (x_3, y_3, z_3) attached to the motor stator, i.e. parallel to the Pushpull lever and the motor swivelling bracket.

Rotation Matrices

The relation between the representations of vectors in each frame is given by their respective rotation matrices. In the following the superscript denotes the frame in which the vector is expressed. Hence, to rotate an arbitrary vector \mathbf{v} from the Reference Frame 2 to the Reference Frame 1:

$${}^1\mathbf{v} = \mathbf{R}_{2to1} {}^2\mathbf{v} \quad (4.3)$$

Where \mathbf{R}_{2to1} is:

$$\mathbf{R}_{2to1} = \begin{bmatrix} \cos(\eta) & 0 & \sin(\eta) \\ 0 & 1 & 0 \\ -\sin(\eta) & 0 & \cos(\eta) \end{bmatrix} \quad (4.4)$$

As the rotation matrix is unitary and orthogonal, its transpose is equivalent to its inverse:

$$\mathbf{R}_{1to2} = \mathbf{R}_{2to1}^T = \begin{bmatrix} \cos(\eta) & 0 & \sin(\eta) \\ 0 & 1 & 0 \\ -\sin(\eta) & 0 & \cos(\eta) \end{bmatrix}^T = \begin{bmatrix} \cos(\eta) & 0 & -\sin(\eta) \\ 0 & 1 & 0 \\ \sin(\eta) & 0 & \cos(\eta) \end{bmatrix} \quad (4.5)$$

Similarly, the rotation matrices from the frames 3 to 2 and from the frames 2 to 3 are defined:

$$\mathbf{R}_{3to2} = \begin{bmatrix} 1 & 0 & 0 \\ 0 & \cos(\gamma) & -\sin(\gamma) \\ 0 & \sin(\gamma) & \cos(\gamma) \end{bmatrix} \quad (4.6)$$

$$\mathbf{R}_{2to3} = \begin{bmatrix} 1 & 0 & 0 \\ 0 & \cos(\gamma) & \sin(\gamma) \\ 0 & -\sin(\gamma) & \cos(\gamma) \end{bmatrix} \quad (4.7)$$

Now, combining these, the rotation matrices from 1 to 3 and from 3 to 1 can be obtained:

$$\mathbf{R}_{1to3} = \mathbf{R}_{2to3}\mathbf{R}_{1to2} = \begin{bmatrix} \cos(\eta) & 0 & -\sin(\eta) \\ \sin(\gamma)\sin(\eta) & \cos(\gamma) & \cos(\eta)\sin(\gamma) \\ \cos(\gamma)\sin(\eta) & -\sin(\gamma) & \cos(\gamma)\cos(\eta) \end{bmatrix} \quad (4.8)$$

$$\mathbf{R}_{3to1} = \begin{bmatrix} \cos(\eta) & \sin(\gamma)\sin(\eta) & \cos(\gamma)\sin(\eta) \\ 0 & \cos(\gamma) & -\sin(\gamma) \\ -\sin(\eta) & \cos(\eta)\sin(\gamma) & \cos(\gamma)\cos(\eta) \end{bmatrix} \quad (4.9)$$

Unit Vectors

As the different motions of the rotorcraft are expressed in the three above defined reference frames, it becomes necessary to define the respective unit vectors of these different reference frames with respect to a single common reference frame. The Euler equation holds for a reference frame in which the inertia tensor is constant. Due to the use of a 3-blade propeller, the inertia tensor is constant around the reference frame 3 as it has been explained before. Therefore the Reference Frame 3 must be the common reference frame in which all motions are to be described.

Hence, the unit vectors of the system 1 and 2 must be defined in terms of the Reference Frame 3.

Now, to define the Unit Vector in x direction of the Frame 1, \mathbf{i}_1 , expressed in the Frame 3, it is necessary to multiply the vector \mathbf{i}_1 by the rotation matrix \mathbf{R}_{1to3} that refers it to the Frame 3, i.e. \mathbf{R}_{1to3} . Therefore:

$${}^3\mathbf{i}_1 = \mathbf{R}_{1to3}{}^1\mathbf{i}_1 = \mathbf{R}_{1to3} \begin{bmatrix} 1 \\ 0 \\ 0 \end{bmatrix} = \begin{bmatrix} \cos(\eta) \\ \sin(\gamma)\sin(\eta) \\ \cos(\gamma)\sin(\eta) \end{bmatrix} \quad (4.10)$$

Similarly the vectors in the y and z axes can be defined:

$${}^3\mathbf{j}_1 = \begin{bmatrix} 0 \\ \cos(\gamma) \\ -\sin(\gamma) \end{bmatrix} \text{ and } {}^3\mathbf{k}_1 = \begin{bmatrix} -\sin(\eta) \\ \cos(\eta)\sin(\gamma) \\ \cos(\gamma)\cos(\eta) \end{bmatrix} \quad (4.11)$$

Likewise Unit Vectors of the frame 2 are expressed in the reference frame 3 as follows.

$${}^3\mathbf{i}_2 = \mathbf{R}_{2\text{to}3} {}^2\mathbf{i}_2 = \begin{bmatrix} 1 \\ 0 \\ 0 \end{bmatrix}, {}^3\mathbf{j}_2 = \mathbf{R}_{2\text{to}3} {}^2\mathbf{j}_2 = \begin{bmatrix} 0 \\ \cos(\gamma) \\ -\sin(\gamma) \end{bmatrix} \text{ and } {}^3\mathbf{k}_2 = \mathbf{R}_{2\text{to}3} {}^2\mathbf{k}_2 = \begin{bmatrix} 0 \\ \sin(\gamma) \\ \cos(\gamma) \end{bmatrix} \quad (4.12)$$

Angular Velocity

The total angular velocity in the spinning assembly is the sum of the 4 main rotations present. Once knowing all the Unit Vectors in the different reference frames it is possible to refer the different angular accelerations to the common reference frame, that is, the Reference Frame 3 or the Spinning Body Frame (see figures 4.2 and 4.3).

The first one, **rotation motion of the vehicle** itself, i.e. angular rates: p, q and r, these rates are given with reference to the vehicle's main body, i.e. Ref. Frame 1, thus:

$${}^3\boldsymbol{\omega}_{\text{vehicle}} = {}^3\mathbf{i}_1 p + {}^3\mathbf{j}_1 q + {}^3\mathbf{k}_1 r \quad (4.13)$$

The second one, the **rotation of the servoblock** shaft driving the entire arm assembly. This rotation vector is aligned with the arm, and thus with the vehicle frame, frame 1, along the y_1 axis. The servoblock deflection angle is noted as η , therefore the angular velocity induced by this tilting axis can be expressed as:

$${}^3\boldsymbol{\omega}_{\text{servoblock}} = {}^3\mathbf{j}_1 \dot{\eta} \quad (4.14)$$

The third rotation to consider is the one actuated by the **push-pull** servo, this is, the contribution of the push-pull motion about the second tilting axis of the rotor assembly. its reference rotation axis is along the hinge, that is Reference Frame 2 and its angle has been denoted γ thus:

$${}^3\boldsymbol{\omega}_{\text{pushpull}} = {}^3\mathbf{i}_2 \dot{\gamma} \quad (4.15)$$

Fourth and finally, the rotation generated by the **motor**, that is, the spinning propeller and outrunner. This vector will be expressed in the reference frame of the motor's stator, i.e. along the shaft of the motor. Therefore:

$${}^3\boldsymbol{\omega}_{\text{motor}} = {}^3\mathbf{k}_3 \Omega \quad (4.16)$$

Where Ω represents the angular rotation speed of the motor and thus propeller, Ω is a signed parameter based upon the convention that a clockwise from above rotation of the propeller is counted as positive due to the downwards orientation of the z_3 axis.

Summing up the total angular velocity of the rotating assembly expressed in the reference frame 3 is:

$${}^3\boldsymbol{\omega}_{\text{total}} = {}^3\boldsymbol{\omega}_{\text{vehicle}} + {}^3\boldsymbol{\omega}_{\text{servoblock}} + {}^3\boldsymbol{\omega}_{\text{pushpull}} + {}^3\boldsymbol{\omega}_{\text{motor}} \quad (4.17)$$

Expanding:

$${}^3\boldsymbol{\omega}_{\text{total}} = {}^3\mathbf{i}_1 p + {}^3\mathbf{j}_1 q + {}^3\mathbf{k}_1 r + {}^3\mathbf{j}_1 \dot{\eta} + {}^3\mathbf{i}_2 \dot{\gamma} + {}^3\mathbf{k}_3 \Omega \quad (4.18)$$

Now recalling the Unit Vectors definition and simplifying:

$${}^3\boldsymbol{\omega}_{\text{Total}} = \begin{bmatrix} \cos(\eta)p - r \sin(\eta) + \dot{\gamma} \\ \sin(\gamma)(\cos(\eta)r + p \sin(\eta)) + \cos(\gamma)(q + \dot{\eta}) \\ \cos(\gamma)(\cos(\eta)r + p \sin(\eta)) + \Omega - \sin(\gamma)(q + \dot{\eta}) \end{bmatrix} \quad (4.19)$$

4.2.1 Angular Acceleration

The angular acceleration is next to be derived. Note that, as the vectors are expressed in rotating frames, several cross product terms arise as the frames themselves rotate.

As with the angular velocity, the angular acceleration is given by the following contributions:

Following the same order as before, let us first derive the acceleration induced by the **vehicle's motion**, i.e. derivative of its angular rates. These rates are expressed in the vehicle frame and, consequently, in the reference frame 1. Thus:

$${}^3\boldsymbol{\alpha}_{\text{vehicle}} = {}^3\mathbf{i}_1\dot{p} + {}^3\boldsymbol{\omega}_{\text{vehicle}} \times {}^3\mathbf{i}_1p + {}^3\mathbf{j}_1\dot{q} + {}^3\boldsymbol{\omega}_{\text{vehicle}} \times {}^3\mathbf{j}_1q + {}^3\mathbf{k}_1\dot{r} + {}^3\boldsymbol{\omega}_{\text{vehicle}} \times {}^3\mathbf{k}_1r \quad (4.20)$$

Secondly, the acceleration caused by the commanded deflection of the **servoblock** tilting motion. As it is linked to the vehicle's main body, the cross product term will appear with the angular velocity of the vehicle: $\boldsymbol{\omega}_{\text{vehicle}}$. Such that:

$${}^3\boldsymbol{\alpha}_{\text{servoblock}} = {}^3\mathbf{j}_1\ddot{\eta} + {}^3\boldsymbol{\omega}_{\text{vehicle}} \times {}^3\mathbf{j}_1\dot{\eta} \quad (4.21)$$

Third, the acceleration due to the **push-pull** tilting mechanism comes third, and it is defined with respect to the reference frame 2. The total angular velocity of the reference frame 2 is the vehicle, ${}^3\boldsymbol{\omega}_{\text{vehicle}}$ angular velocity, added to the angular velocity of the servoblock, ${}^3\boldsymbol{\omega}_{\text{servoblock}}$, since it is attached to the arm which is rotating with the servoblock.

$${}^3\boldsymbol{\alpha}_{\text{pushpull}} = {}^3\mathbf{i}_2\ddot{\gamma} + ({}^3\boldsymbol{\omega}_{\text{vehicle}} + {}^3\boldsymbol{\omega}_{\text{servoblock}}) \times {}^3\mathbf{i}_2\dot{\gamma} \quad (4.22)$$

Finally, the angular acceleration generated by the **motor** spinning the propeller is expressed with respect to the motor mount or its stator, that is in the reference frame 3. The angular velocities to appear in this acceleration's cross product terms will be the sum of those generated by the vehicle itself, the servoblock and the pushpull mechanism. Thus:

$${}^3\boldsymbol{\alpha}_{\text{motor}} = {}^3\mathbf{k}_3\dot{\Omega} + ({}^3\boldsymbol{\omega}_{\text{vehicle}} + {}^3\boldsymbol{\omega}_{\text{servoblock}} + {}^3\boldsymbol{\omega}_{\text{pushpull}}) \times {}^3\mathbf{k}_3\Omega \quad (4.23)$$

The total angular acceleration of the propeller assembly can then be expressed as:

$$\begin{aligned}
{}^3\alpha_{\text{Total}} = & {}^3\mathbf{i}_1\dot{p} + {}^3\boldsymbol{\omega}_{\text{vehicle}} \times {}^3\mathbf{i}_1p + {}^3\mathbf{j}_1\dot{q} + {}^3\boldsymbol{\omega}_{\text{vehicle}} \times {}^3\mathbf{j}_1q + {}^3\mathbf{k}_1\dot{r} + {}^3\boldsymbol{\omega}_{\text{vehicle}} \times {}^3\mathbf{k}_1r + {}^3\mathbf{j}_1\ddot{\eta} \\
& + {}^3\boldsymbol{\omega}_{\text{vehicle}} \times {}^3\mathbf{j}_1\dot{\eta} + {}^3\mathbf{i}_2\ddot{\gamma} + ({}^3\boldsymbol{\omega}_{\text{vehicle}} + {}^3\boldsymbol{\omega}_{\text{servoblock}}) \times {}^3\mathbf{i}_2\dot{\gamma} + \\
& {}^3\mathbf{k}_3\dot{\Omega} + ({}^3\boldsymbol{\omega}_{\text{vehicle}} + {}^3\boldsymbol{\omega}_{\text{servoblock}} + {}^3\boldsymbol{\omega}_{\text{pushpull}}) \times {}^3\mathbf{k}_3\Omega \quad (4.24)
\end{aligned}$$

Resolving the terms into its components and simplifying results in:

$${}^3\boldsymbol{\alpha} = \begin{bmatrix} {}^3\alpha_x \\ {}^3\alpha_y \\ {}^3\alpha_z \end{bmatrix} \quad (4.25)$$

where:

$${}^3\alpha_X = \cos(\eta)\dot{p} - \sin(\eta)\dot{r} - (\cos(\eta)r + p\sin(\eta))\dot{\eta} + \Omega(\sin(\gamma)(\cos(\eta)r + p\sin(\eta)) + \cos(\gamma)(q + \dot{\eta})) + \ddot{\gamma} \quad (4.26)$$

$$\begin{aligned}
{}^3\alpha_Y = & \cos(\gamma)\dot{q} + \sin(\gamma)(\sin(\eta)\dot{p} + \cos(\eta)\dot{r}) - \Omega(\cos(\eta)p - r\sin(\eta) + \dot{\gamma}) + \\
& \sin(\gamma)(\cos(\eta)p - r\sin(\eta))\dot{\eta} + \dot{\gamma}(\cos(\gamma)(\cos(\eta)r + p\sin(\eta)) - \sin(\gamma)(q + \dot{\eta})) + \cos(\gamma)\ddot{\eta} \quad (4.27)
\end{aligned}$$

$$\begin{aligned}
{}^3\alpha_Z = & -\sin(\gamma)\dot{q} + \cos(\gamma)(\sin(\eta)\dot{p} + \cos(\eta)\dot{r}) + \cos(\gamma)(\cos(\eta)p - r\sin(\eta))\dot{\eta} \\
& - \dot{\gamma}(\sin(\gamma)(\cos(\eta)r + p\sin(\eta)) + \cos(\gamma)(q + \dot{\eta})) + \dot{\Omega} - \sin(\gamma)\ddot{\eta} \quad (4.28)
\end{aligned}$$

4.2.2 Total Moments

Introducing the calculated $\boldsymbol{\alpha}_{\text{Total}}$ and $\boldsymbol{\omega}_{\text{Total}}$ into equation 4.1, with the definition of the diagonal Inertia tensor, yields:

$${}^3\mathbf{M} = \begin{bmatrix} {}^3\mathbf{M}_x \\ {}^3\mathbf{M}_y \\ {}^3\mathbf{M}_z \end{bmatrix} \quad (4.29)$$

where:

$$\begin{aligned}
{}^3\mathbf{M}_x = & I_{zz}(\sin(\gamma)(\cos(\eta)r + p\sin(\eta)) + \cos(\gamma)(q + \dot{\eta}))(\cos(\gamma)(\cos(\eta)r + p\sin(\eta)) + \Omega \\
& - \sin(\gamma)(q + \dot{\eta})) + I_{yy}(\sin(\gamma)(\cos(\eta)r + p\sin(\eta)) + \cos(\gamma)(q + \dot{\eta}))(-\cos(\gamma)(\cos(\eta)r + p\sin(\eta)) - \Omega \\
& + \sin(\gamma)(q + \dot{\eta})) + I_{xx}(\cos(\eta)(\dot{p} + r(\sin(\gamma)\Omega - \dot{\eta})) + \cos(\gamma)\Omega(q + \dot{\eta}) - \sin(\eta)(\dot{r} + p(-\sin(\gamma)\Omega + \dot{\eta}))) + \ddot{\gamma} \quad (4.30)
\end{aligned}$$

$$\begin{aligned}
{}^3\mathbf{M}_y = & I_{zz}(-\cos(\eta)p + r\sin(\eta) - \dot{\gamma})(\cos(\gamma)(\cos(\eta)r + p\sin(\eta)) + \Omega - \sin(\gamma)(q + \dot{\eta})) + \\
& I_{xx}(\cos(\eta)p - r\sin(\eta) + \dot{\gamma})(\cos(\gamma)(\cos(\eta)r + p\sin(\eta)) + \Omega - \sin(\gamma)(q + \dot{\eta})) \\
& + I_{yy}(\cos(\gamma)\dot{q} - \Omega(\cos(\eta)p - r\sin(\eta) + \dot{\gamma}) + \sin(\gamma)(-\dot{\gamma}(q + \dot{\eta})) \\
& + \cos(\eta)(\dot{r} + p\dot{\eta}) + \sin(\eta)(\dot{p} - r\dot{\eta})) + \cos(\gamma)((\cos(\eta)r + p\sin(\eta))\dot{\gamma} + \ddot{\eta}) \quad (4.31)
\end{aligned}$$

$$\begin{aligned}
{}^3\mathbf{M}_z = & \cos(\gamma)(-(I_{xx}-I_{yy}+I_{zz})\dot{\gamma}(q+\dot{\eta})+\sin(\eta)((I_{xx}-I_{yy})qr+I_{zz}\dot{p}-(-I_{xx}+I_{yy}+I_{zz})r\dot{\eta})) \\
& + \cos(\eta)(I_{zz}\dot{r} + p((-I_{xx} + I_{yy})q + (-I_{xx} + I_{yy} + I_{zz})\dot{\eta})) \\
& + I_{zz}\dot{\Omega} + \frac{1}{2} \sin(\gamma)(2(-I_{xx} + I_{yy}) \cos(2\eta)pr - (I_{xx} - I_{yy})(p^2 - r^2) \sin(2\eta) \\
& - 2(I_{xx} - I_{yy} + I_{zz}) \cos(\eta)r\dot{\gamma} - 2(I_{xx} - I_{yy} + I_{zz})p \sin(\eta)\dot{\gamma} - 2I_{zz}(\dot{q} + \dot{\eta}))
\end{aligned} \tag{4.32}$$

The moments above are expressed in reference frame 3, generated about the CG of the full rotating assembly. These moments are the result of the actuated motion of all the described degrees of freedom of the rotorcraft, so the reactions on the airframe will be $-{}^3\mathbf{M}$. Additionally they still have to be translated to the body axis, i.e. into the frame 1. Thus, the total action of the tilting and rotating motions on the airframe is given by:

$${}^1\mathbf{M}_{\text{React}} = \mathbf{R}_{3\text{to}1}(-{}^3\mathbf{M}) \tag{4.33}$$

Now with the values calculated before it yields:

$${}^1\mathbf{M}_{\text{React}} = \begin{bmatrix} {}^3\mathbf{M}_{\text{React}_X} \\ {}^3\mathbf{M}_{\text{React}_Y} \\ {}^3\mathbf{M}_{\text{React}_Z} \end{bmatrix} \tag{4.34}$$

where:

$$\begin{aligned}
{}^1\mathbf{M}_{\text{React}_X} = & \frac{1}{4}(-2I_{xx}qr + I_{yy}qr + I_{zz}qr + 3I_{yy} \cos(2\gamma)qr - 3I_{zz} \cos(2\gamma)qr \\
& - 4I_{zz} \sin(\gamma)\Omega r + 2I_{yy}\dot{\eta}r + 2I_{zz}\dot{\eta}r + 2I_{yy} \cos(2\gamma)\dot{\eta}r - 2I_{zz} \cos(2\gamma)\dot{\eta}r - 2I_{xx}\dot{p} - I_{yy}\dot{p} \\
& - I_{zz}\dot{p} + I_{yy} \cos(2\gamma)\dot{p} - I_{zz} \cos(2\gamma)\dot{p} - 2I_{yy}p \sin(2\gamma)\dot{\gamma} + 2I_{zz}p \sin(2\gamma)\dot{\gamma} \\
& - \sin(2\eta)(4(I_{xx}-I_{yy})p \sin(\gamma)\Omega + 2(I_{yy}-I_{zz})r \sin(2\gamma)\dot{\gamma} - (2I_{xx}-I_{yy}-I_{zz})(\dot{r}+p(q+2\dot{\eta}))) \\
& - (I_{yy}-I_{zz}) \cos(2\gamma)(\dot{r}+p(q+2\dot{\eta}))) - \cos(2\eta)(4(I_{xx}-I_{yy})r \sin(\gamma)\Omega + 2(I_{zz}-I_{yy})p \sin(2\gamma)\dot{\gamma} \\
& + (2I_{xx} - I_{yy} - I_{zz})(\dot{p} - r(q + 2\dot{\eta})) + (I_{yy} - I_{zz}) \cos(2\gamma)(\dot{p} - r(q + 2\dot{\eta}))) \\
& - 2 \cos(\eta)(2(I_{xx} - I_{yy} + I_{zz}) \cos(\gamma)\Omega(q + \dot{\eta}) + (I_{yy} - I_{zz}) \sin(2\gamma)(q - r + \dot{\eta}) \\
& (q+r+\dot{\eta})+2I_{xx}\ddot{\gamma})-2 \sin(\eta)(-2(-I_{xx}+I_{yy}+I_{zz}) \sin(\gamma)\Omega\dot{\gamma}-2I_{xx}(q+\dot{\eta})\dot{\gamma}+2(I_{yy}-I_{zz}) \\
& \cos(2\gamma)(q + \dot{\eta})\dot{\gamma} + 2I_{zz} \cos(\gamma)\dot{\Omega} - (I_{yy} - I_{zz}) \sin(2\gamma)(pr - \dot{q} - \dot{\eta}))
\end{aligned} \tag{4.35}$$

$$\begin{aligned}
{}^1\mathbf{M}_{\text{React}_Y} = & \frac{1}{4}(-2I_{xx} \sin(2\eta)p^2 + I_{yy} \sin(2\eta)p^2 + I_{zz} \sin(2\eta)p^2 - 4I_{xx} \cos(2\eta)rp \\
& + 2I_{yy} \cos(2\eta)rp + 2I_{zz} \cos(2\eta)rp - 4I_{xx} \sin(\eta)\dot{\gamma}p + 2I_{xx}r^2 \sin(2\eta) - \\
& I_{yy}r^2 \sin(2\eta) - I_{zz}r^2 \sin(2\eta) - 2I_{yy}\dot{q} - 2I_{zz}\dot{q} - 4I_{xx} \cos(\eta)r\dot{\gamma} - 4(I_{xx}-I_{yy}-I_{zz}) \cos(\gamma)\Omega(\cos(\eta)p \\
& - r \sin(\eta) + \dot{\gamma}) + 2(I_{yy}-I_{zz}) \sin(2\gamma)(-\sin(\eta)(qr+\dot{p}) + \cos(\eta)(pq-\dot{r}) + 2\dot{\gamma}(q+\dot{\eta})) + 4I_{zz} \sin(\gamma) \\
& \dot{\Omega} - 2I_{yy}\ddot{\eta} - 2I_{zz}\ddot{\eta} - 2(I_{yy}-I_{zz}) \cos(2\gamma)(\dot{q} + (\cos(\eta)r + p \sin(\eta))(\cos(\eta)p - r \sin(\eta) + 2\dot{\gamma}) + \dot{\eta}))
\end{aligned} \tag{4.36}$$

$$\begin{aligned}
{}^1\mathbf{M}_{\text{React}z} = & \frac{1}{4}(-2(I_{yy} - I_{zz}) \sin(2\gamma) \sin(\eta)p^2 - (4(I_{yy} - I_{zz}) \cos(2\gamma)\dot{\eta} \sin^2(\eta) \\
& + (2(-2I_{xx} + I_{yy} + I_{zz}) \cos^2(\eta) - (I_{yy} - I_{zz}) \cos(2\gamma)(\cos(2\eta) - 3))q \\
& - 4(I_{zz} + (I_{yy} - I_{xx}) \cos(2\eta)) \sin(\gamma)\Omega + 2(I_{yy} - I_{zz}) \cos(\eta) \sin(2\gamma)(r + 2 \sin(\eta)\dot{\gamma}) + \\
& 2(I_{yy} + I_{zz} + (-2I_{xx} + I_{yy} + I_{zz}) \cos(2\eta))\dot{\eta})p - 2I_{xx}\dot{r} - I_{yy}\dot{r} - I_{zz}\dot{r} + I_{yy} \cos(2\gamma) \\
& \dot{r} - I_{zz} \cos(2\gamma)\dot{r} - 2I_{yy}r \sin(2\gamma)\dot{\gamma} + 2I_{zz}r \sin(2\gamma)\dot{\gamma} - \cos(2\eta)((-2I_{xx} + I_{yy} + I_{zz} + (I_{zz} - I_{yy}) \cos(2\gamma))\dot{r} + \\
& 2(I_{yy} - I_{zz})r \sin(2\gamma)\dot{\gamma}) - \sin(2\eta)(4(I_{yy} - I_{xx})r \sin(\gamma)\Omega + (2I_{xx} - I_{yy} - I_{zz})(r(q + 2\dot{\eta}) - \dot{p}) \\
& + (I_{yy} - I_{zz}) \cos(2\gamma)(r(q + 2\dot{\eta}) - \dot{p})) - 2 \sin(\eta)(- (I_{yy} - I_{zz}) \sin(2\gamma)(q + \dot{\eta})^2 \\
& - 2(I_{xx} - I_{yy} + I_{zz}) \cos(\gamma)\Omega(q + \dot{\eta}) - 2I_{xx}\dot{\gamma}) - 2 \cos(\eta)(-2(-I_{xx} + I_{yy} + I_{zz}) \sin(\gamma)\Omega\dot{\gamma} \\
& - 2I_{xx}(q + \dot{\eta})\dot{\gamma} + 2(I_{yy} - I_{zz}) \cos(2\gamma)(q + \dot{\eta})\dot{\gamma} + 2I_{zz} \cos(\gamma)\dot{\Omega} + (I_{yy} - I_{zz}) \sin(2\gamma)(\dot{q} + \dot{\eta}))
\end{aligned}
\tag{4.37}$$

4.3 Aerodynamic Modelling

In this section the Aerodynamic forces and moments acting on the vehicle will be studied. The frame of the vehicle is very small, and the total wet area is also very small, therefore the analysis will focus only on the propellers since its forces and moments are orders of magnitude larger than all the other aerodynamic effects such as the airframe drag.

A common rule of thumb is to compare the airspeed of the vehicle to the linear velocity of the rotating blade at $\frac{3}{4}$ of the Radius. In this case, this comparison gives that the vehicle speed is orders of magnitude smaller and, hence, the Hover or Quasi-Hover hypothesis can be assumed. Given that, then, that the main aerodynamic forces and moments applied onto the vehicle will be the Thrust and the Aerodynamic Drag Torque.

In order to model those effects, a classical approach in Aeronautical Engineering has been followed by describing them in terms of dimensionless coefficients. Its development, for example, can be seen in [21]. In this case the thrust will be represented by C_T such that:

$$T = \rho A (\Omega R)^2 C_T \tag{4.38}$$

And the Torque coefficient will be represented by C_Q such that:

$$Q = \rho A (\Omega R)^2 R C_Q \tag{4.39}$$

Where ρ represents the air density, A is the area of the rotor disk, R its radius and Ω is the angular velocity of the propeller.

Usually, in the literature of quadrotor design, analytical calculations are conducted to obtain the Thrust and Torque coefficients of the propellers, see [4]. These calculations are mostly based on Blade Element Theory and Momentum theory. Also, another alternative would be to use Goldstein's Vortex

Theory of Screw Propellers, see [?]. All these methods require more or less an extensive geometric description of the propeller. Since the manufacturer was not able to provide this information and the measuring of it was a challenge in itself, it was decided instead to measure experimentally the propeller characteristics. Suitable facilities weren't available to measure these coefficients over a wide range of flight conditions, i.e. different Angles of Attack, Sideslip, Advance Velocity and Vertical Velocity. Thus the measurements were performed in only static rig for both Thrust and Torque across all the range of attainable rpm regimes. The results obtained from these rig tests will permit us to determine the coefficients C_T and C_Q to model the thrust and torque production of the platform. Considering that the initial controller is meant to stabilise the vehicle around a stable hover condition, it is not expected that this shortcoming will have major repercussions on the performance of the controller.

In the following, the procedure to obtain C_T and C_Q will be described. The experimental setup is described in detail in A, but for convenience is summarised here. The motor is mounted on a L-shaped hinged stand, so that the force is transmitted to a balance which measures the thrust, see figure 4.4. The torque is measured in a separate test by using the same assembly with the motor mounted perpendicular to the L-shaped stand, see 4.5. The voltage supplied was 16 volt and current was displayed by a power supply. A weather station measured Temperature, Pressure and Humidity, necessary to estimate the density. And a laser interferometer accurately measured the angular velocity of the propeller Ω , see figure 4.6.

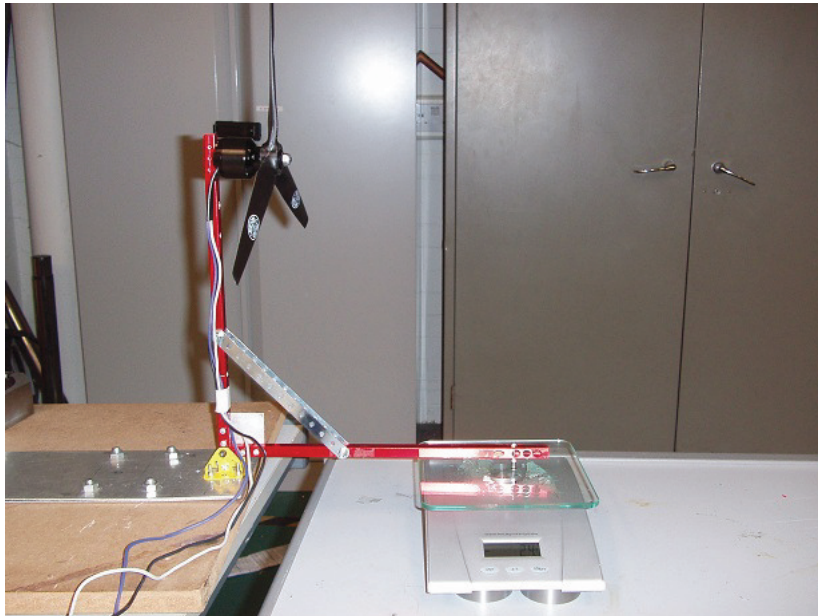


Figure 4.4: Thrust Measurement Stand.



Figure 4.5: Torque Measurement Stand .

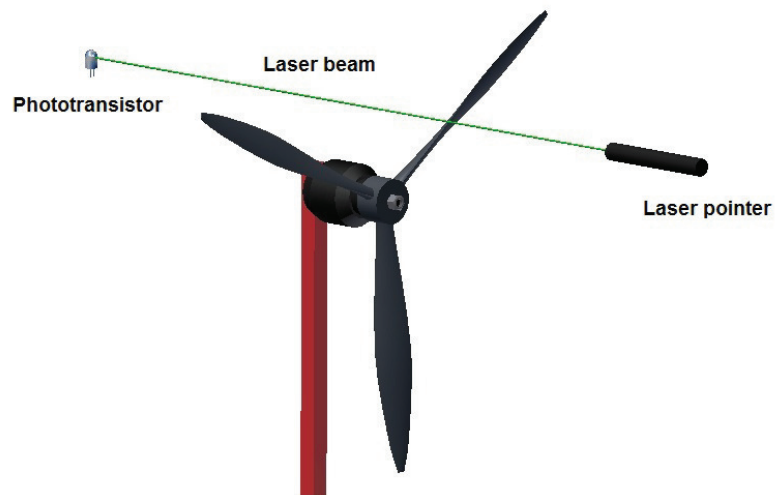


Figure 4.6: Laser Interferometer Setup.

Aerodynamic Analysis

From the recorded data in the tests the coefficients were found by calculating the slopes of the curves T vs $\rho A(\Omega R)^2$ and Q vs $\rho A(\Omega R)^2 R$. These are shown in figures 4.7 and 4.8, and the slopes of the fitted curves are the Thrust (C_T) and Torque (C_Q) coefficients respectively. It was found that the thrust coefficient was $C_T = 0.013$ and the torque coefficient was $C_Q = 0.0013$. According to the momentum theory, the factor of merit of a rotor is (see [21]):

$$FM = \frac{\text{Ideal Power}}{\text{Power in the Prop Hub}} = \frac{P_{\text{ideal}}}{P_{\text{Induced}} + P_{\text{Profile}}} = \frac{C_{P_{\text{ideal}}}}{C_{P_{\text{Total}}}} = \frac{\frac{C_T^{\frac{3}{2}}}{\sqrt{2}}}{C_P} = 0.79 \quad (4.40)$$

Numerically the power coefficient is equal to the torque coefficient, therefore, with the aforementioned values, the figure of merit of the propeller is: $FM = 0.79$.

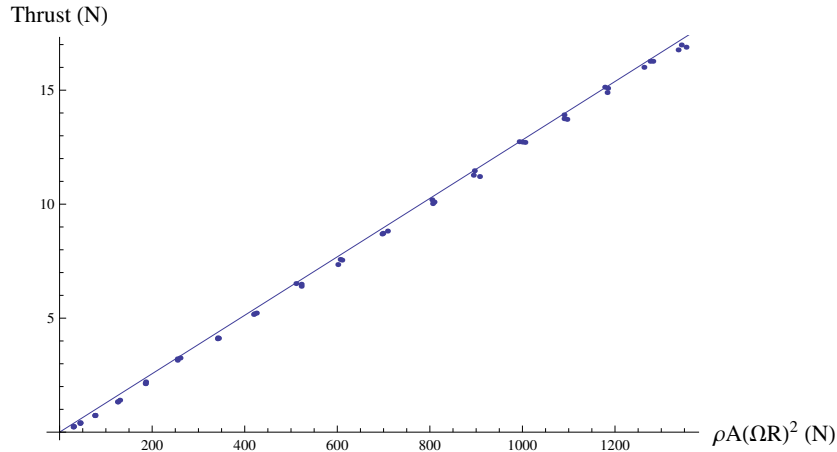


Figure 4.7: Thrust vs $\rho A(\Omega R)^2$.

4.4 Motopropulsive Group Modelling and Characterisation

Two main tests were conducted static and dynamic. The static tests were performed to assess the performance and the suitability of the propeller and the motor, assessing variables such as thrust torque and current consumption. The dynamic tests were conducted with the aim of introducing a realistic representation of the behaviour of the controller-motor-propeller system in the simulation model.

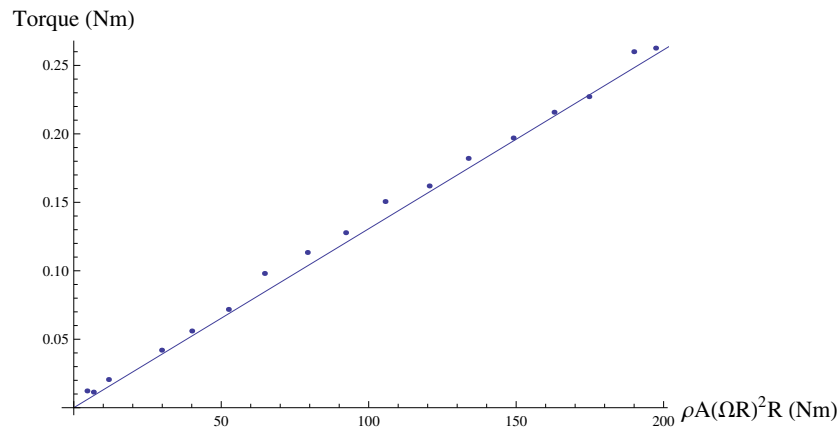


Figure 4.8: Torque vs $\rho A(\Omega R)^2 R$.

4.4.1 Static Testing

In the static testing 3 main aspects were assessed:

1. **Motor Performance.** Analysing the quality of the behaviour of the motors selected and how efficient they are.
2. **Motor Controller Characterisation.** Analysis of the linearity and characteristics of the motor controller (ESC).
3. **Global Propulsive Performance.** Assessment of the overall propulsive system: i.e. Propeller+Motor+ESC. And assessment of its efficiency.

Description of the experimental Set-Up for static testing.

The setup for the motor testing is described in detail in appendix A. In the following the main details are summarised. A power supply provided power to the motor at 16V and displayed the current. A static balance recorded the thrust or the torque load, depending on the test. A weather station recorded pressure, temperature and humidity in order to calculate air density. And a laser interferometer based on a phototransistor, a laser and an oscilloscope provided the angular velocity of the propeller at every blade pass. The tests were conducted using the Master Airscrew 12 x 6 3-blade Propeller and also using the ESC Roxy BI Control 930-6 to drive the motor phases.

Motor Performance Tests.

To accurately assess the suitability of the motor selected, the MK3638, reliable data describing the power output and efficiency was needed. The manufacturer of the motor, Mikrokopter, only provided poorly documented tests with rough data describing only current and thrust, and declined to provide any further details. Therefore a thorough testing and analysis was needed to validate the suitability of the power plant and to analyse the performance and

endurance of the whole vehicle.

According to the manufacturer, the specifications of the motor are shown in table 3.2.

In the test, current, torque and angular velocity of the motor were recorded. In this way, in order to assess the efficiency of the motor-controller system the mechanical power output was analysed against the electrical power input. The mechanical power output is computed from the angular velocity and torque and the electric power is computed from the voltage and the current. In figure [?] mechanical power is plotted against the electric power. The fitting, then yields the curve:

$$P_{\text{Elect.}} = 1.1719 + 1.4271P_{\text{Mech}} + 0.0019P_{\text{Mech}}^2 \quad (4.41)$$

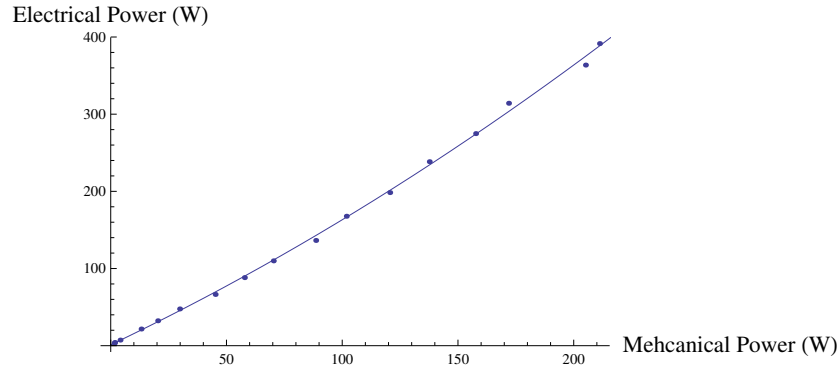


Figure 4.9: Mechanical Power vs Electric Power.

The efficiency of the motor-ESC system is defined as:

$$\eta_{\text{Motor+ESC}} = \frac{\text{Mechanical Power Output}}{\text{Electrical Power Input}} \quad (4.42)$$

Therefore from equation 4.41:

$$\eta_{\text{Motor+ESC}} = \frac{P_{\text{Mech}}}{1.1719 + 1.4271P_{\text{Mech}} + 0.0019P_{\text{Mech}}^2} \quad (4.43)$$

Then, equation 4.43 is plotted in figure 4.10 alongside the efficiency calculated from the raw experimental data.

ESC Performance

Brushless DC motors need a controller to energise their coils according to the desired angular velocity. The control signal is sent via a PWM signal where the length of the high pulse determines the angular velocity of the motor. As it is a common practice in RC the high pulse was set to be between 1mS and 2mS. Thus 1mS meant 0% of throttle and 2mS meant 100%.

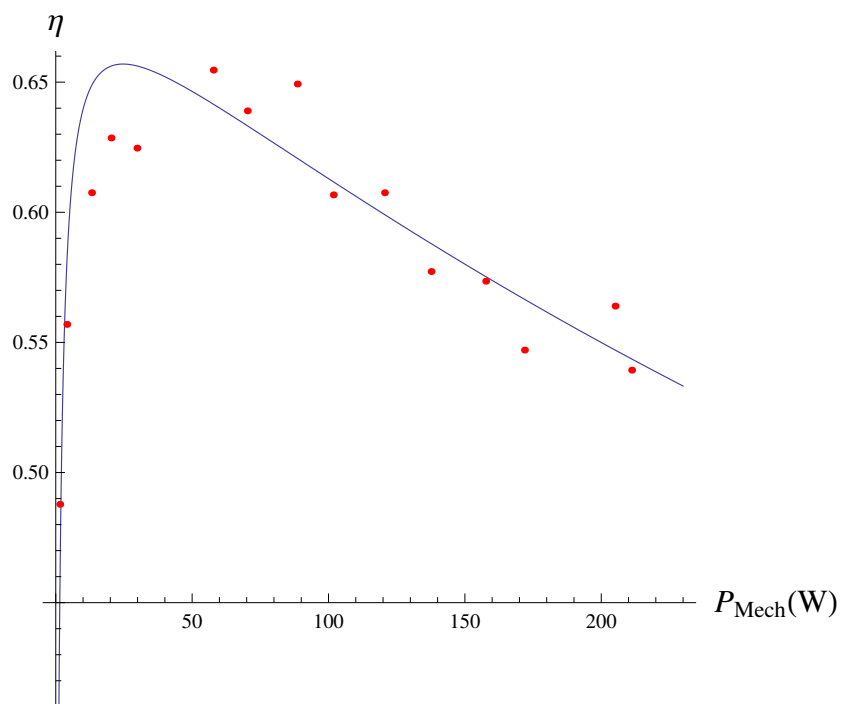


Figure 4.10: Efficiency vs Mechanical Power Output. From fitted curve (eq. 4.43) and raw data.

As before all the testing is described in appendix A. To assess the linearity of the controller, the angular speed in steady state has been plotted against the throttle position from 0 to 1, sent to the ESC, in figure 4.11. It can be seen that around the nominal working point, i.e. 50% of throttle it exhibits very linear behaviour although in the edges, near 0% and 100%, the nonlinearities begin to arise.

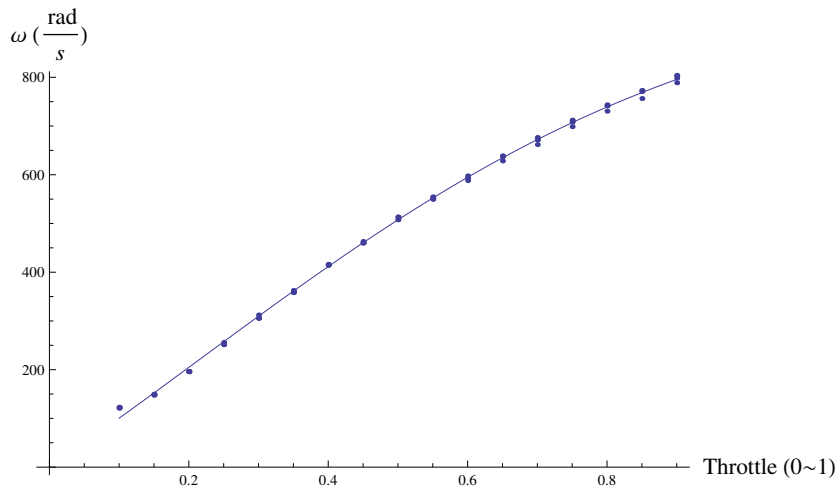


Figure 4.11: Throttle Position vs Angular Velocity of the Propeller, Steady state.

To assess the behaviour of the ESCs on their role of drivers of thrust generating devices, the throttle vs thrust is plotted in figure 4.12 around its nominal operating point. As it can be seen, the ESC shows a linear behaviour near the operating point of feasible thrust demands.

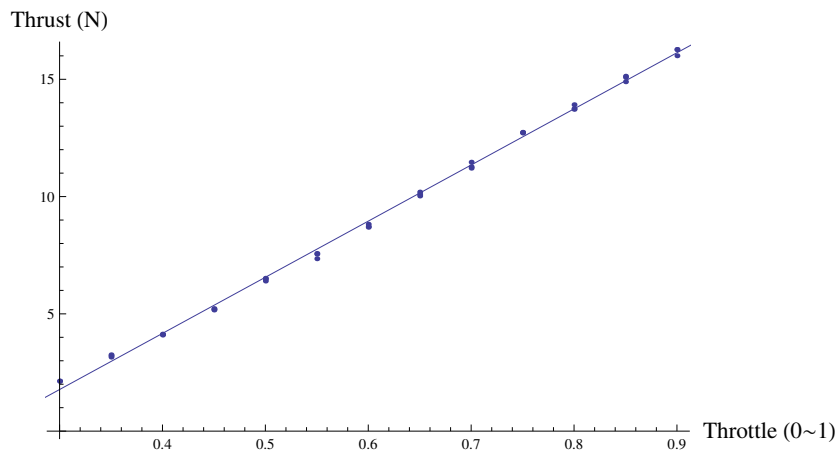


Figure 4.12: Thrust vs Throttle, Controller Linearity.

Global Performance

To assess the performance of the system a useful index must be defined. Efficiencies are always what you obtain over what you pay for it. In this case what we get is the Aerodynamic Thrust and what we pay for is the Electric Power. Thus the efficiency at hover can be defined as:

$$\eta_{\text{Hover}} = \frac{\text{Ideal Hover Power}}{\text{Electrical Power}} = \frac{P_{\text{Ideal}}}{P_{\text{Electrical}}} \quad (4.44)$$

This parameter therefore captures the quality of the combined system of the propeller and the motor.

Based on momentum theory, see [21], the ideal power coefficient, P_{Ideal} , is given by:

$$C_{P_{\text{Ideal}}} = \frac{C_T^{\frac{3}{2}}}{\sqrt{2}} \quad (4.45)$$

From the given definitions for the thrust and torque coefficients then:

$$P_{\text{Ideal}} = \frac{T^{3/2}}{\sqrt{2S\rho}} \quad (4.46)$$

Therefore, from 4.44

$$\eta_{\text{Hover}} = \frac{P_{\text{Ideal}}}{P_{\text{Electrical}}} = \frac{T^{3/2}}{IV} \quad (4.47)$$

All parameters in equation 4.47 were measured in the experiments, these are plotted in figure 4.13.

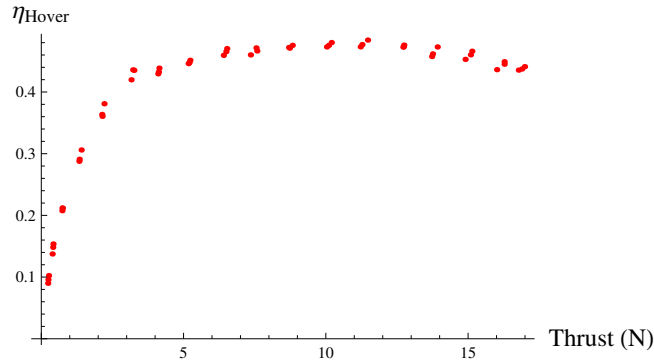


Figure 4.13: Hovering Efficiency vs Thrust Generated.

From figure 4.13, it can be concluded that above 5 Newtons of thrust the system is more or less constant in its efficiency that allows for a large operating range, in terms of different payloads and endurances without a major loss in efficiency and thus performance. The ramp until 3.5N is likely to be caused by a laminar to turbulent transition on the blades of the propeller, this is further explained in A.

4.4.2 Dynamic Modelling of the Motors.

In order to simulate effectively the vehicle's dynamics, it is fundamental to have an accurate model of its main control action generators, that is, the motors. To achieve this, a series of experiments were conducted to gather information about the system behaviour.

The approach followed for modelling the motor was simply to identify its transfer function from throttle input in (%) to angular velocity (rad/s) output. These parameters depend strongly upon the whole motopropulsive system that is: the motor itself, the speed controller and the propeller.

The vehicle weight is around 3Kg thus each motor will carry at a nominal point 7.5N. Therefore, a series of sinusoidal inputs of the same amplitude and different frequencies were fed around this nominal point and the steady state response in rad/s was recorded with a common time base with the input fed.

The experimental setup is described in detail in appendix A. To summarise, it consists of a rig where the motor is fixed so that the propeller crosses a laser beam that is energising the base of a PNP phototransistor, thus closing the circuit when the beam is hitting the base, and opening it every time a blade crosses the beam. Both the output of the phototransistor and the PWM signal input to the ESC were monitored for all the frequencies. See figure 4.6.

The sequence followed in these experiments is summarised in figure 4.14. First the data is gathered. Second it is processed in a way that pulses are converted into variables of interest. Third, a sinusoid is fitted with a common time reference both for the input and the output. And finally, fourth, all the frequencies fed are put into a common bode plot and transfer function is fitted.

Once both the data from the interferometer and the PWM signal were gathered with a common time reference, both trains of pulses had to be converted to meaningful parameters.

The PWM signal was converted into a sampled signal at every pulse with a value equivalent to the high pulse, hence containing the throttle position at each pulse.

The signal from the interferometer was converted into a sampled signal with a shared time reference with PWM, with a value equivalent to the inverse of 3 times (3-blade propeller) the time elapsed between two rising flanks, that is, the propeller frequency. The whole process is illustrated in figure 4.15.

With the data ready in terms of throttle vs time and angular velocity vs time a sinusoidal function of the form:

$$F(t) = B + A \sin(2\pi ft + \phi) \quad (4.48)$$

For both the input and the output for all the frequencies tested, a sample result for the fitting of an input signal is shown in figure: 4.16.

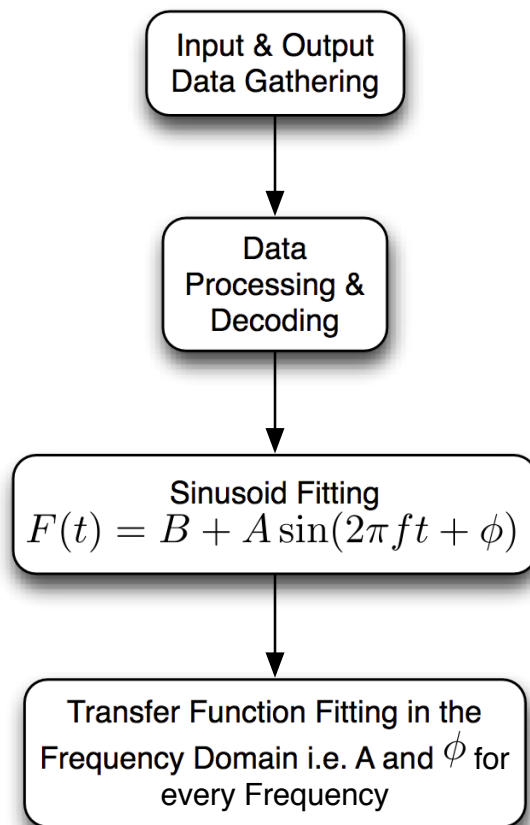


Figure 4.14: Description of the Frequency Domain identification process

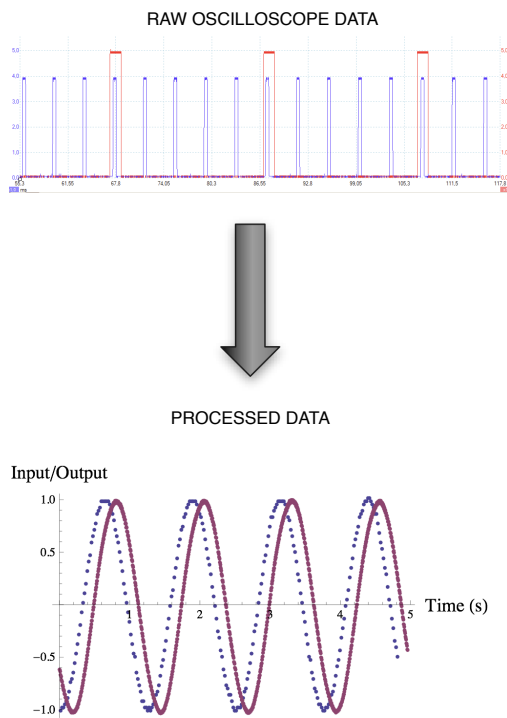


Figure 4.15: Description of the frequency domain data processing. Blue is input and red is output, in order to be able to plot them in the same picture they've both been normalised with amplitude one and zero average.

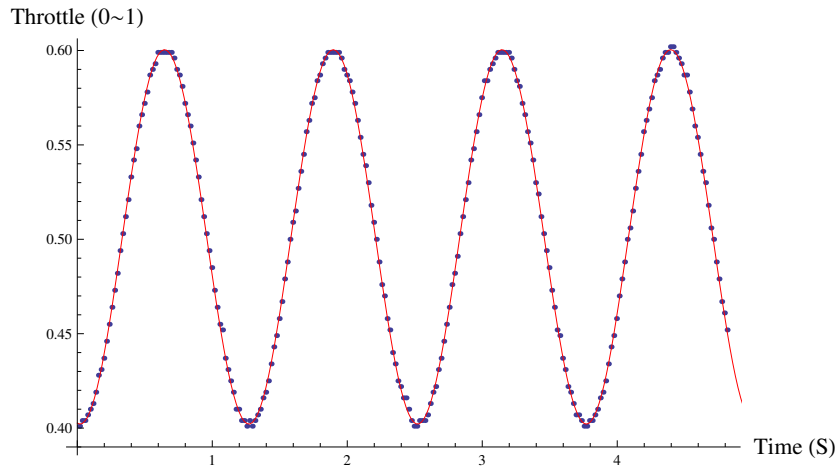


Figure 4.16: Sample of a fitted sinusoidal to a throttle input of 0.8Hz frequency.

With all the information of amplitude and phase for input and output for every frequency, they were all put together in the bode plot shown in figure 4.17

Once the data was in the frequency domain, it was possible to find the underlying dynamical model. It is very clear from the Gain Bode plot that there is a pole due to the -20dB per decade and so it had to be a first order system.

To find the exact time constant and the gain a minimisation problem was set up by fitting a first order function in the frequency domain to match the points gathered. This problem was solved using a least squares approach of the decimal logarithms of the gain, so that the results were balanced for all the spectrum of attainable frequencies. The resulting transfer function was found to be:

$$G_{\text{motor}} = \frac{\text{Angular Velocity}}{\text{Throttle Input}} = \frac{\Delta\omega \left(\frac{\text{rad}}{\text{s}}\right)}{\Delta\tau (0 \text{ to } 1)} = \frac{9.19026}{(1 + 0.1621s)} \quad (4.49)$$

The results of this fit are shown in figure 4.18

The phase, though, was not represented by the first order model and therefore a pure delay had to be added to model the lag that was present in the experimental data. A similar approach was followed to that in the fitting the Gain was carried out, but this time using the Phase to find the best fit for the delay time constant. The motor then was represented by a first order system and a pure delay. The final result for the transfer function of the motor was then:

$$G_{\text{motor}} = \frac{\text{Angular Velocity}}{\text{Throttle Input}} = \frac{\Delta\omega \left(\frac{\text{rad}}{\text{s}}\right)}{\Delta\tau (0 \text{ to } 1)} = \frac{e^{-0.035s} 9.19}{(1 + 0.16s)} \quad (4.50)$$

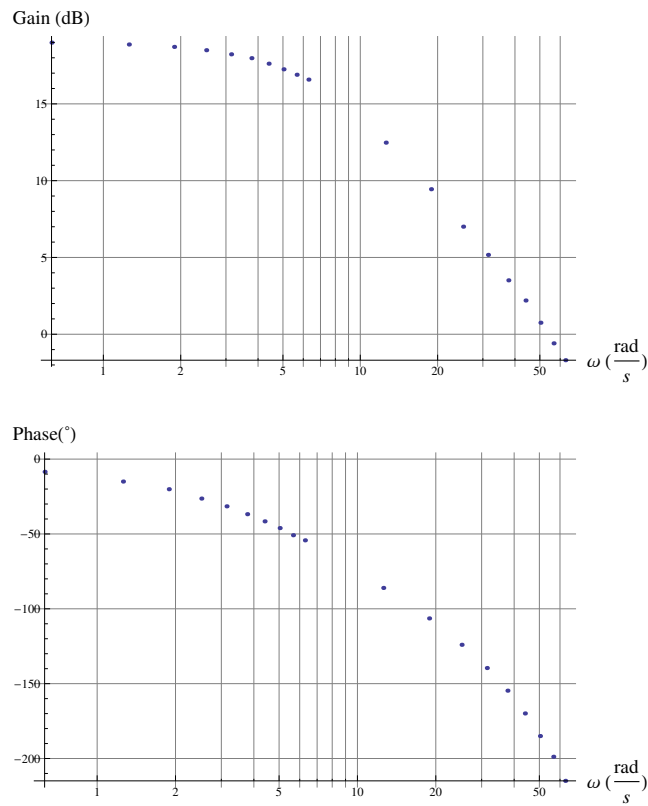


Figure 4.17: Phase and Gain for all the frequencies fed into the motor around the 50% throttle operating point. Note that the input throttle from 0 to 1 and the output is in radian per second. Therefore an offset in the gain is due to unit scaling.

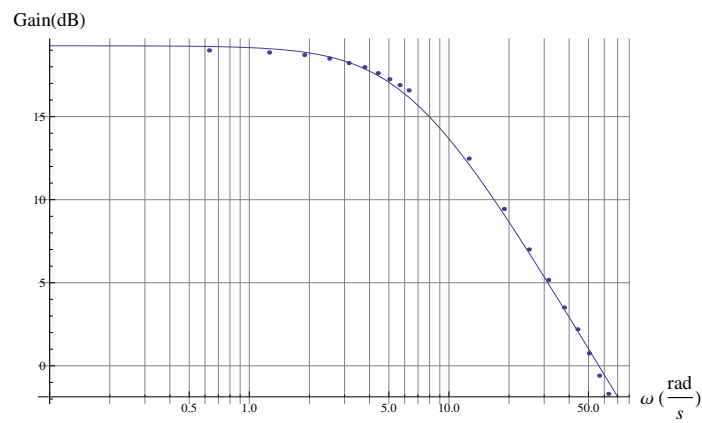


Figure 4.18: Frequency domain motor transfer function gain fit.

The results are shown in the Bode Plot of figure 4.19 alongside the experimental data obtained.

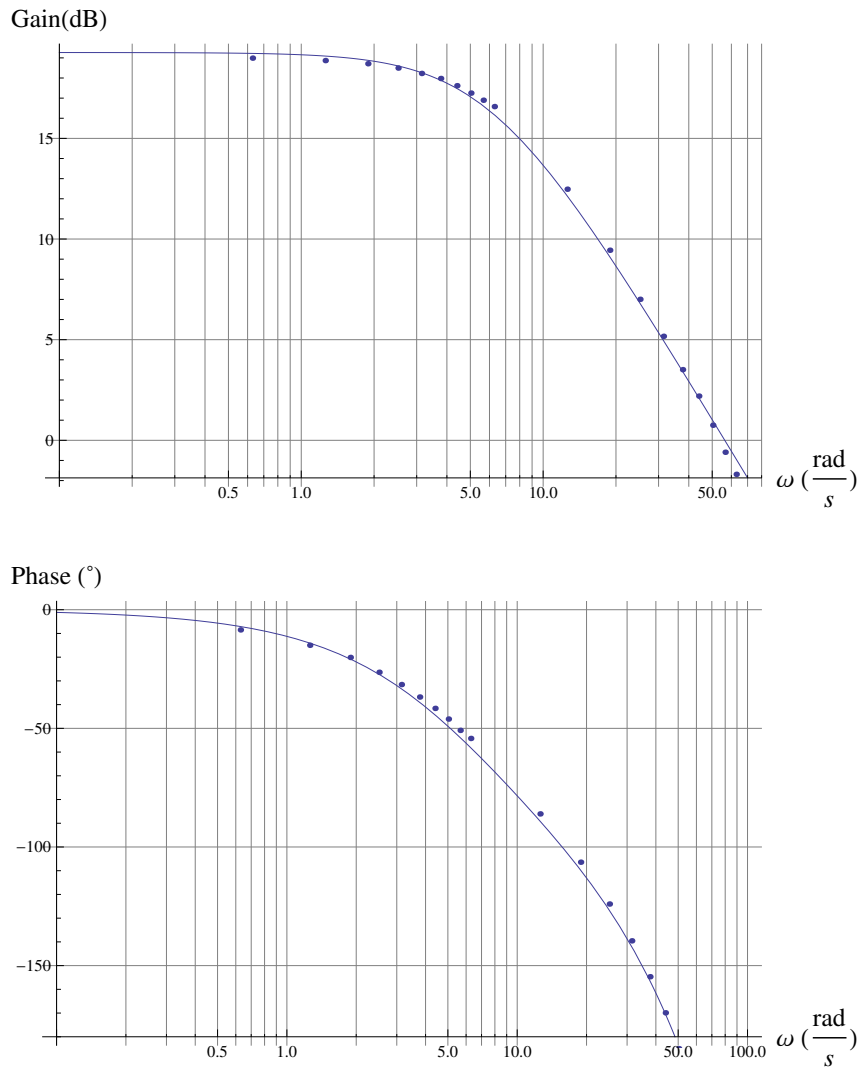


Figure 4.19: Frequency domain motor transfer function gain and phase fit.

4.5 Servo Motor Modelling

4.5.1 Introduction

A servomotor is a device that receives an angle as input encoded in a PWM signal and moves its lever to the position requested. They are widely used in the RC hobby market due to their compact size, ease of use, simplicity and low weight compared to traditional DC motor and driving circuitry.

On the other hand, their dynamics are not trivial; since they implement an internal controller to regulate their position, their input and output are thus position. The whole servomotor is composed essentially by a DC motor with gearbox, a potentiometer and a driver circuit with a controller.

Essentially the working principle is: a position signal is fed into the internal microcontroller that then drives an amplifier that drives the coils of the motor according to a regulator that reads the feedback from the potentiometer. In the work by [36] the authors describe a physical model of a servo of the same characteristics as the one used in this project.

In order to deduce the dynamic characteristics of the internal structure of the servo, the approach followed has been purely a black box system ID, instead of trying to produce the model from physical principles, i.e. simply finding the transfer function between the input and the output regardless of the internal “nuts and bolts”. That is, several input signals have been fed and the output has been recorded. From that data then a transfer function model has been fitted in the frequency domain to give a picture of the dynamic behaviour of this position-in position-out system.

In the vehicle, servomotors are used to drive both the servo block mechanism and the push pull mechanism, and the servo used is the HS-7940TH. Although all the servos are exactly the same they drive slightly different inertias at different gearing ratios, so a full model of the arm was constructed to independently produce the system identification data. See figure 4.20 for the illustration of the servoblock motion and figure 4.21 for the illustration of the pushpull motion.

The accuracy of this model is critical because as can be seen in the rigid body modelling section, a huge control action depends upon the angular rates $\dot{\eta}$ and $\dot{\gamma}$. And therefore the control system design will be dependant on whether this estimates are accurate.

4.5.2 Experimental Setup.

The exact details of the experimental setup for the servo model system identification are given in appendix A. The details of it are summarised here for convenience.

The input signal to the servo is a PWM signal in which the length of the high pulse signifies the angle of the servo. Therefore initially a mapping is conducted in which the length of the high pulse, mS, is mapped against the

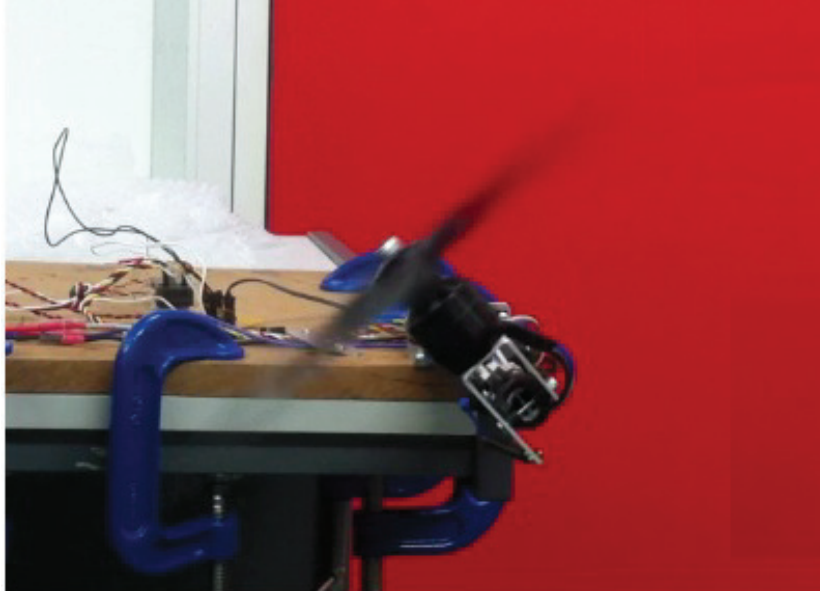


Figure 4.20: Servoblock motion testing on the prototype arm.

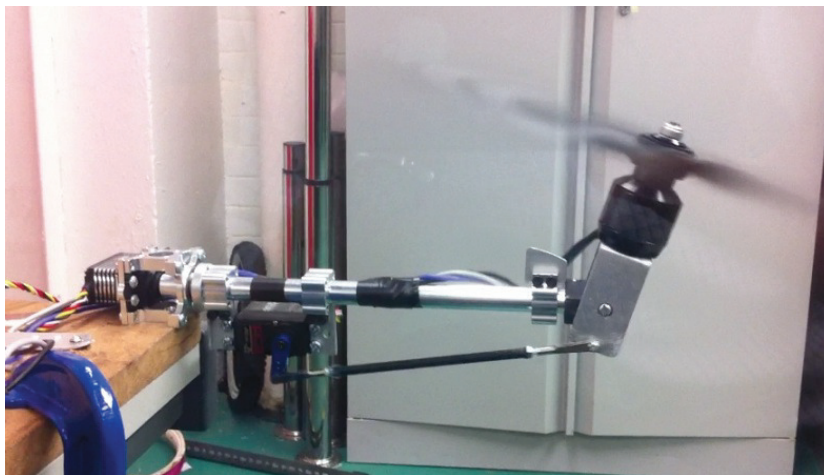


Figure 4.21: Pushpull motion testing on the prototype arm.

angle (rad). In practice the angle of the servo can not be measured directly but it can be easily modified to fit a wire to the internal potentiometer. Therefore a mapping between the voltage of the potentiometer and the angle was also conducted. These mappings resulted in the acquisition of the gains to relate both, PWM mS to requested angle and voltage to the actual angle.

According to the manufacturer, the operating voltage for the servos is 7.4V, that's why all the tests have been conducted feeding a nominal 7.4V from a power supply to the servos including the mapping.

As with the motor system identification a usb oscilloscope was set up to read the input PWM signal sent to the servo and the output in this case the voltage of the potentiometer. The strategy followed in the feeding of the signals was the same as with the motor, that is, several sinusoids were fed over a range of relevant frequencies and the amplitude and phase were obtained and used to get a picture of the dynamic response and fitting a transfer function.

One of the main issues encountered was the significant amount of high frequency noise found in the potentiometer signal. This problem was solved by using a low pass filter, available into the PicoScope software of the USB oscilloscope, with a cutoff frequency two orders of magnitude higher than the actual sinusoids, that is around 100Hz to 700Hz, depending on the test.

The processing of the raw data coming from the oscilloscope was basically identifying the high pulse length of the PWM of the input, the same way as with the motor, and filtering the noise of the feedback. This is illustrated in figure 4.22.

Once this data was available, a sinusoidal function was fitted in the same way as described in the motor system ID, to obtain phase (ϕ) and gain (A) for every frequency.

During all the tests, the propeller was running at nominal rpm that is around 5000 rpm which generates a nominal thrust of 7.5N.

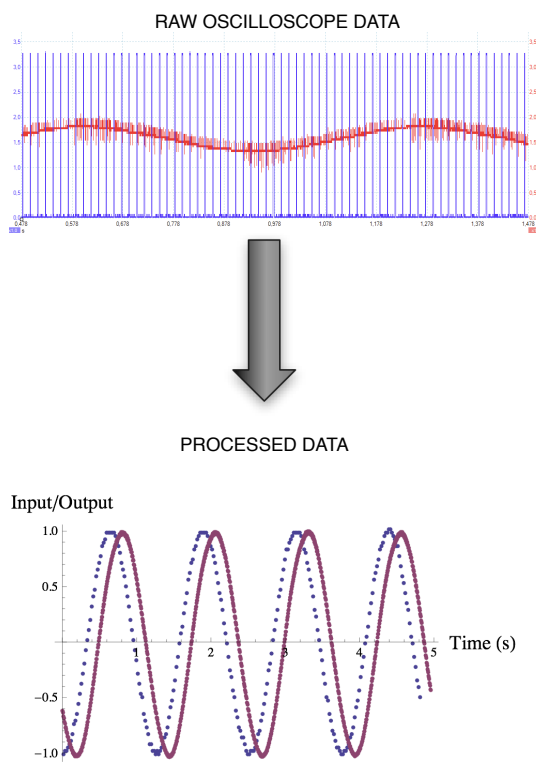


Figure 4.22: Data processing for the servo sinusoid System Identification. Blue is input and red is output.

4.5.3 Servoblock system ID

Once all the processing was carried out, the phase and gain of the servoblock servo is illustrated in the bode plot of figure 4.23.

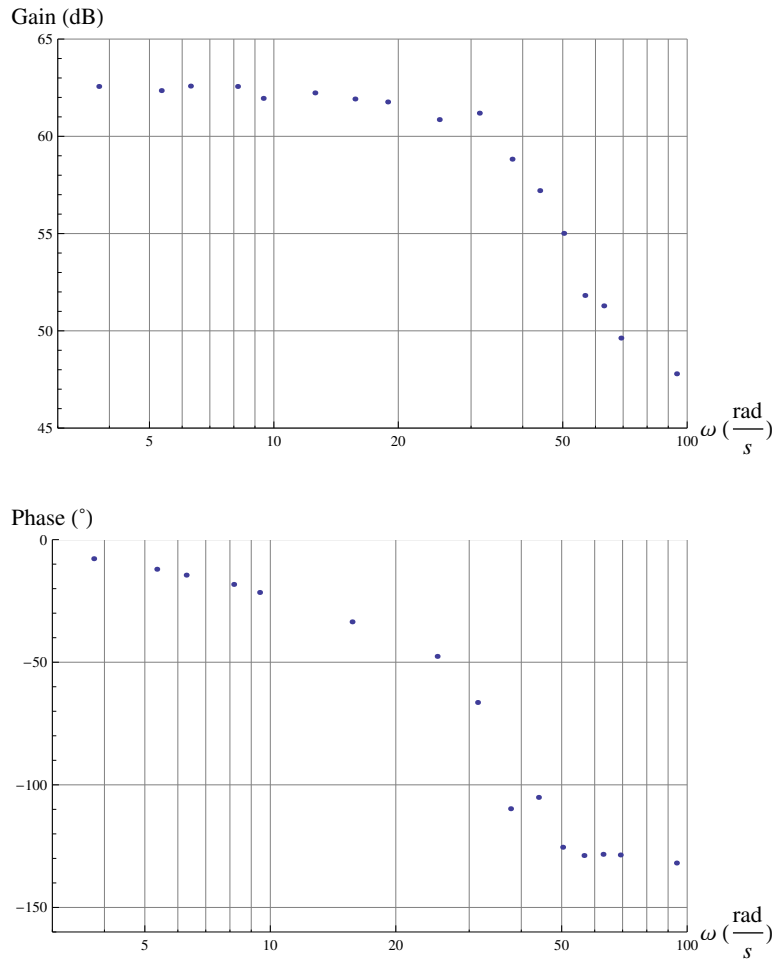


Figure 4.23: Frequency domain servoblock transfer function gain and phase fit.

As it can be seen in figure 4.23, the gain shows a negative slope of about -40dB, per decade therefore a second order system will represent this behaviour accurately. With a minimisation of the least squares difference between the experimental data and the function in both in dB, the parameters of the function were found yielding the transfer function:

$$G_{\text{servoblock}} = \frac{\text{Feedback Volts}}{\text{Pulse Uptime}} = \frac{\Delta V \text{ Volts}}{\Delta t \text{ (S)}} = \frac{1.60544 \times 10^6}{1228.05 + 49.1806s + s^2} \quad (4.51)$$

The results of this fit are illustrated in figure 4.24. For the simulation model though, the input will be servo position in radians and the output actual servo

position in radians, therefore the transfer function has to be scaled, yielding:

$$G_{\text{servoblock}} = \frac{\text{Actual Angle}}{\text{Requested Angle}} = \frac{\eta \text{ (rad)}}{\eta_{\text{Requested}} \text{ (rad)}} = \frac{1228.05}{1228.05 + 49.1806s + s^2} \quad (4.52)$$

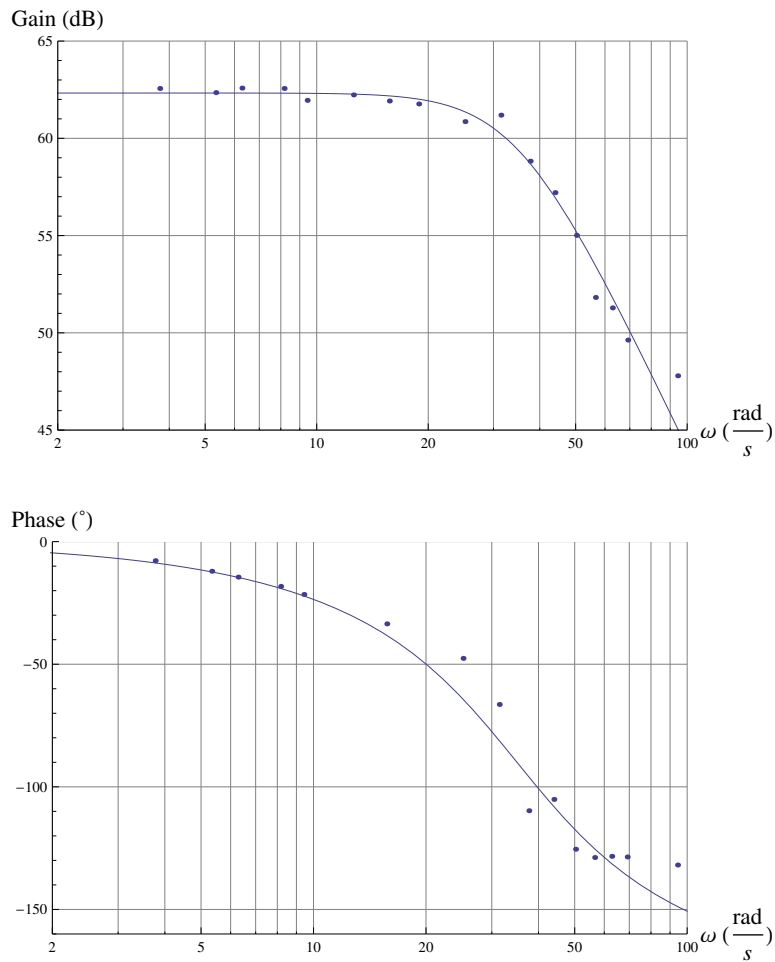


Figure 4.24: Frequency domain servoblock transfer function gain and phase fit.

4.5.4 Push Pull system ID

Similarly as before, the phase and gain of the pushpull servo is illustrated in the bode plot of figure 4.25. It can be seen that at high frequencies there is a larger scatter than with the servoblock. This is likely to be caused by the existence of play and backlash in the mechanical transmission of the motion from the servo to the motor mount.

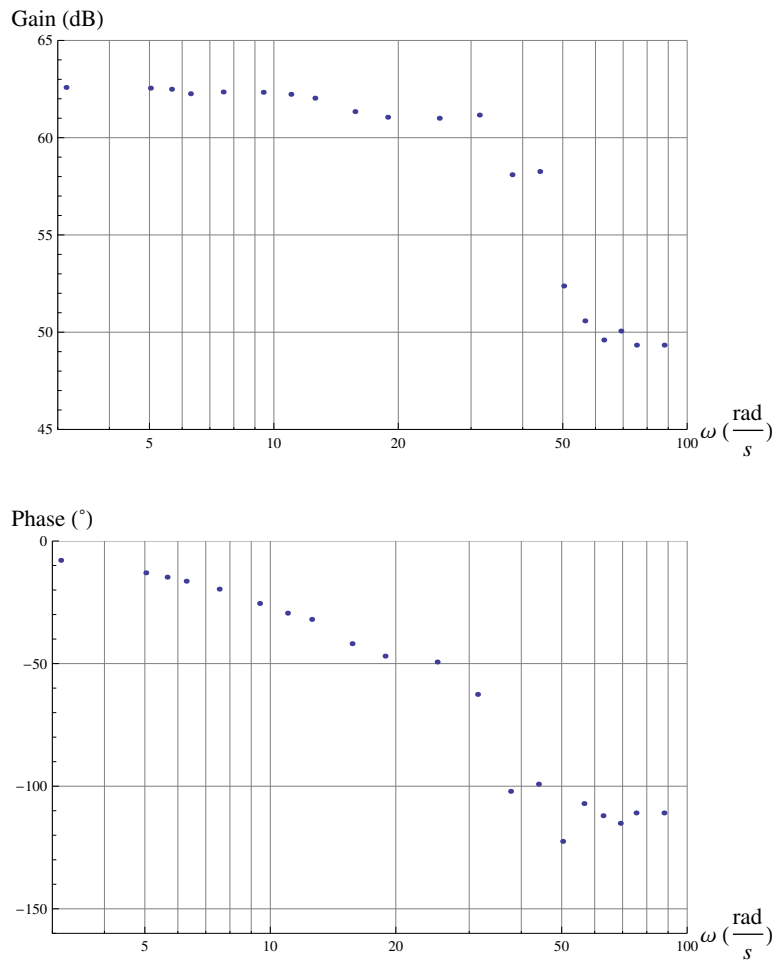


Figure 4.25: Frequency domain Push Pull transfer function gain and phase fit.

As before in figure 4.25, the gain shows a negative slope of about -40dB per decade therefore a second order system will accurately represent this behaviour. Fitting a second order system the transfer function is:

$$G_{\text{pushpull}} = \frac{\text{Feedback Volts}}{\text{Pulse Uptime}} = \frac{\Delta V \text{ Volts}}{\Delta t \text{ (S)}} = \frac{1.58939 \times 10^6}{1212.73 + 51.105s + s^2} \quad (4.53)$$

The results of this fit are illustrated in figure 4.26. For the simulation model though the input will be servo position in radians and servo output in radians, so the transfer function has to be scaled, yielding:

$$G_{\text{pushpull}} = \frac{\text{Actual Angle}}{\text{Requested Angle}} = \frac{\gamma \text{ (rad)}}{\gamma_{\text{Requested}} \text{ (rad)}} = \frac{1212.73}{1212.73 + 51.105s + s^2} \quad (4.54)$$

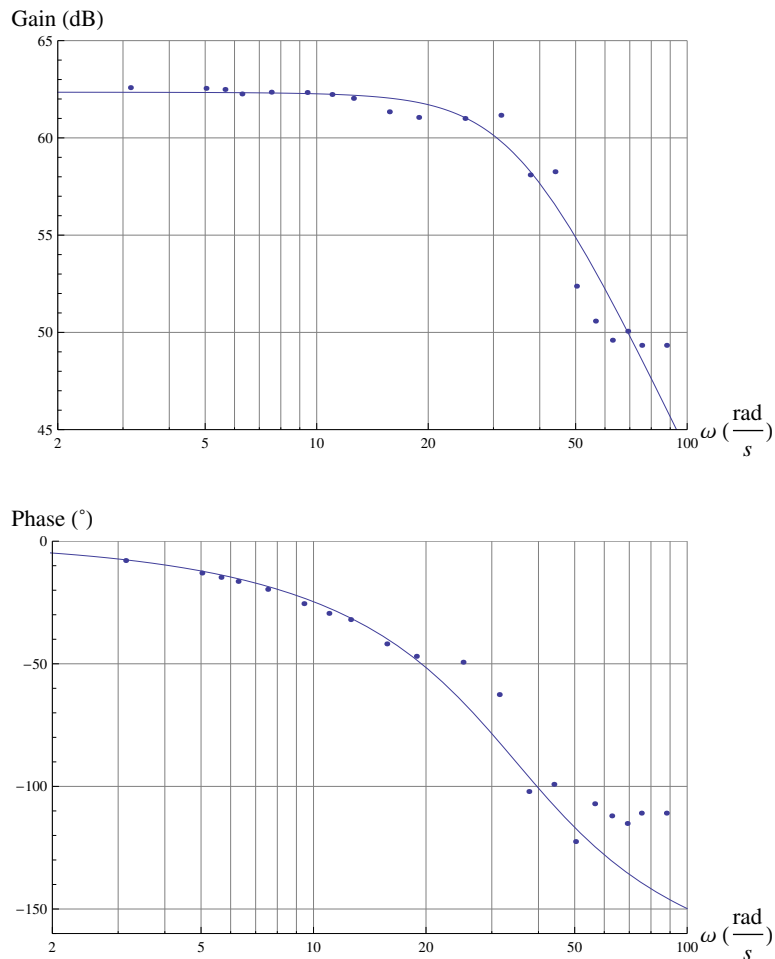


Figure 4.26: Frequency domain Push Pull transfer function gain and phase fit.

4.6 Equations of motion

The equations of motion used in the development of the model are the standard full 6 degree of freedom for a rigid aircraft. Its development can be found in any serious book about Flight Dynamics, the interested reader can refer for example to Cook [7] or Stengel [34].

$$\begin{cases} X = m(\dot{u} + qw - rv) \\ Y = m(\dot{v} + ru - pw) \\ Z = m(\dot{w} + pv - qu) \\ L = I_x\dot{p} - I_{yz}(r^2 - p^2) - I_{xy}(\dot{p} + pq) - I_{xy}(\dot{q} - rp) - (I_y - I_z)qr \\ M = I_y\dot{q} - I_{zx}(r^2 - p^2) - I_{xy}(\dot{p} + qr) - I_{yz}(\dot{r} - pq) - (I_z - I_x)rp \\ Z = I_z\dot{r} - I_{xy}(p^2 - q^2) - I_{yz}(\dot{q} + rp) - I_{zx}(\dot{p} - qr) - (I_x - I_y)pq \end{cases} \quad (4.55)$$

For the representation of the angles, the Euler formulation was chosen, therefore, the Euler angular rates were given, as a function of p, q and r by:

$$\begin{bmatrix} \dot{\phi} \\ \dot{\theta} \\ \dot{\psi} \end{bmatrix} = \begin{bmatrix} 1 & \sin \phi \tan \theta & \cos \phi \tan \theta \\ 0 & \cos \phi & -\sin \phi \\ 0 & \frac{\sin \phi}{\cos \theta} & \frac{\cos \phi}{\cos \theta} \end{bmatrix} \begin{bmatrix} p \\ q \\ r \end{bmatrix} \quad (4.56)$$

In the Simulink simulation model, all this equations will be mechanised by the use of the Aerospace Toolbox block 6DOF, Euler Formulation.

4.7 Simulation Model

4.7.1 Main Structure

All these modelling equations were implemented in the simulation model. The main structure of the simulation model can be seen in figure 4.27. It is composed of 4 main blocks:

- **Controller:** From the sensor reading, it issues the virtual control commands, it will be further described in the Control Design chapter.
- **Control Allocator:** This block contains the logic that distributes the virtual input demands into the individual control inputs, it will be further described in the Control Design chapter.
- **Vehicle Dynamics:** Contains the actuator equations and the equations of motion that have been developed in this chapter. The internal workings of this block will be further developed.
- **Sensor (IMU):** Represents the sensor suite, in this case it simulates the IMU and the inherent noise.

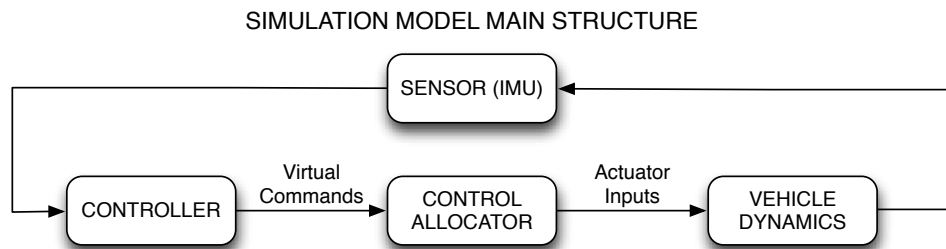


Figure 4.27: Main structure of the simulation model.

The implementation of this block in Simulink can be seen in figure C.1.

4.7.2 Vehicle Dynamics Block

In figure 4.28 the inside of the vehicle dynamics block is shown. It is composed by:

- **Actuator:** Contains the action of the individual arms, both aerodynamic and rigid body. Its inputs are both the rotation motion of the vehicle and the control inputs.
- **Gravity:** Generates the gravitational forces and projects it into body axis. In this case there are no moments since the EOM are centered in the CG.
- **Perturbation:** Contains the terms to generate perturbations to test the controllers.
- **6DOF Equations of Motion:** Is composed of the 6DOF equations of motion described in this chapter: equations 4.55 and 4.56. These equations are centred in the CG, therefore all forces and moments which are inputed to it have to be transported to the CG.

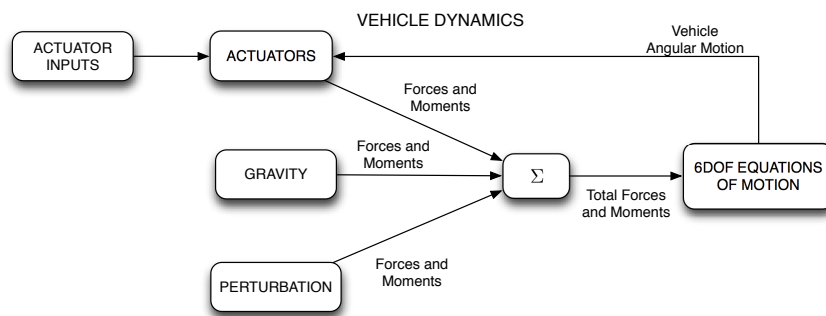


Figure 4.28: Inside of the Vehicle Dynamics Block.

The implementation of this block in Simulink can be seen in figure C.2.

4.7.3 Actuators Block

The actuators block, see figure 4.29, is composed of the four arms of the vehicle. Each of them generates forces and moments according to the control inputs and according to the rotation of the vehicle. The inside of each of the blocks is the same, and implements all the dynamics and aerodynamics developed in this chapter. The only change on each arm block is the projection of the axis to account for the position of each individual arm. Note that the layout of the arms is the same as in the vehicle, Arm 1 is the front, 2 the back, 3 the right and 4 the left.

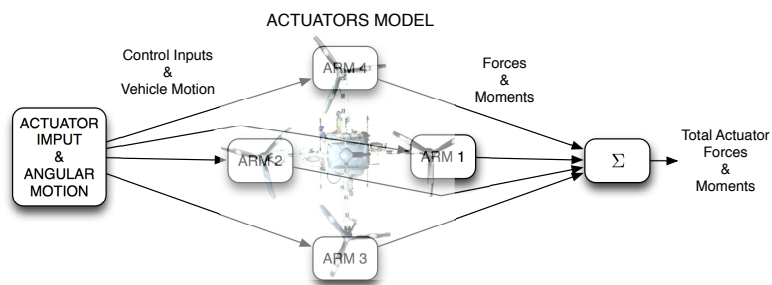


Figure 4.29: Actuator Block, generates the forces and moments from the control inputs and the angular motion.

The implementation of this block in Simulink can be seen in figure C.3.

4.7.4 Standard Actuator Block

The Standard Actuator block, see figure 4.30, is the block that mechanises all the equations developed in this chapter. The approach followed was to project calculate the forces and moments for a Standard Arm, that is, the one described in the Rigid Body section and then rotate the forces and moment vectors according to each individual arms.

First there is the individual actuators dynamics which creates the motion that is fed to the aerodynamic equations and the rigid body equations. They are:

- **Motor Dynamics:** Reads the control input for the motor and outputs the angular velocity, Ω , and angular acceleration, $\dot{\Omega}$, of the rotation assembly. According to the dynamics developed in this chapter, equation A.1. If the propeller in this arm is rotating anticlockwise from above then it outputs the negated angular velocity: $-\Omega$, and angular acceleration: $-\dot{\Omega}$.
- **Push Pull Dynamics:** Reads the control input to the Push Pull and through the Push Pull dynamics developed in this chapter (equation A.3) outputs the angle γ , the angular velocity $\dot{\gamma}$ and the angular acceleration $\ddot{\gamma}$.

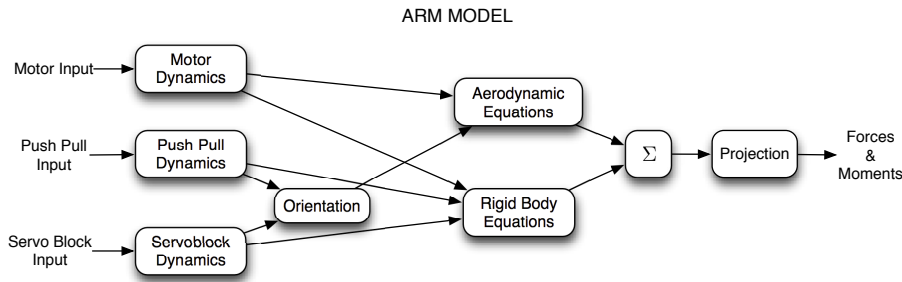


Figure 4.30: Standard Actuator model, mechanises the dynamics: Rigid Body and Aerodynamics of an arm.

- **Servo Block Dynamics:** From the input to the Servoblock servo generates the angle η , angular velocity $\dot{\eta}$ and angular acceleration $\ddot{\eta}$ using the transfer function developed in this chapter (equation A.2).

The Aerodynamic and Rigid Body blocks take the motion of the individual actuator, Motor, Push Pull and Servoblock and calculate the Forces and Moments that they create. That is thrust and its torque in the CG, drag torque, and the gyroscopic or rigid body moments. Its blocks are:

- **Aerodynamic Block:** This block generates the thrust (equation 4.38), the moment that the thrust generates around the CG and the drag torque (equation 4.39) from the spinning propeller motion Ω . It does so from the equations derived in the aerodynamic section taking into account the orientation of the tilted propeller i.e. η and γ .
- **Rigid Body Block:** Mechanises the equations derived in the Rigid Body section (equation 4.34). That is, it generates the gyroscopic (Rigid Body) moments from the rotating propeller motion Ω , the angular motion of the body, $p \ q \ r \ \dot{p} \ \dot{q} \ \dot{r}$, the motion of the servoblock $\eta \ \dot{\eta} \ \ddot{\eta}$ and the motion of the pushpull $\gamma \ \dot{\gamma} \ \ddot{\gamma}$.

Once the Forces and Moments have been computed around the CG in body axis created by the Standard Arm, they have to be projected in each of the four individual arms. To clarify this as an example let's see the difference between Arm 1 and 2. They both create the same forces and moments when they are fed the same control inputs or the same vehicle motion, but the axis of its components is different with respect to the body axis. So the magnitude of the forces and moments is the same the only difference is the directions. Hence, there is no need to re-derive all the rigid body equations as it can simply be rotated accordingly to the position of each arm. This is taken into account with by the projection block.

The implementation of a sample arm, Arm 1, block in Simulink can be seen in figure C.4, and the Simulink implementation of the internal workings of the standard arm can be seen in figure C.5.

Chapter 5

Control System Design

5.1 Introduction

In this chapter the control system will be developed. The general architecture of the control system is shown in figure 5.1. The control system is based on two main components, the control law and the control allocator. The control law is a SCAS that system receives the pilot commands from the transmitter and the motion information from the IMU sensor and issues the required rolling, pitching yawing moments and thrust. The Control Allocator, takes the rolling, pitching yawing moments and thrust and distribute them among the 12 actuators.

The control allocator development is carried out in the first section. In this section, first, a brief introduction to what is a control allocator is given. Second, the reasons to chose a Weighted Pseudoinverse Control Allocator are argued. Third, the required control effectiveness matrix or B Matrix is derived base upon approximation of the nonlinear equations. And, fourth and finally, the selection of the weight matrix is carried out to shape the blend of actuators to obtain the desired response.

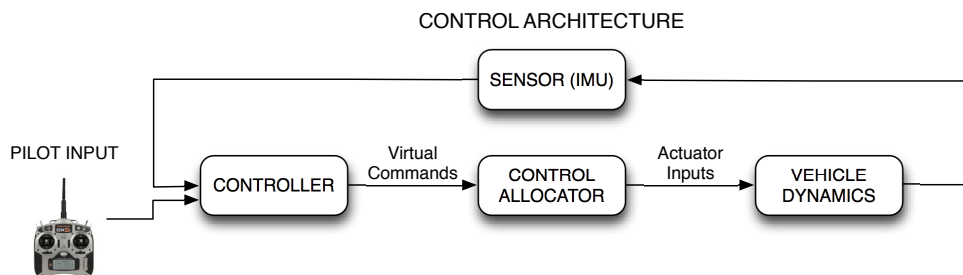


Figure 5.1: Main structure of the control system.

From the transmitter the pilot will issue commands of Roll angle, Pitch angle, Yaw angle and total thrust. The architecture of the design is, hence, a SCAS system has been designed to control the Angles while the thrust is directly feed-through to the allocator. The design of the SCAS system is based on the fact that from the IMU high quality measurements of the Angles and the Angular rates are available, thus, a PD control has been chosen as a simple but effective solution.

The design of the gains of the PD controller has been carried out independently for each axis, as independent SISO systems, since little interaction exists between the different axes and their actuators are modelled around hover state. The critical angles for the stability of the vehicle are Roll and Pitch, while the Yaw is only important for the orientation. Hence to design for the gains for Pitch and Roll, which happen to be identical since the vehicle is symmetric, a simplified model has been constructed and a closed loop transfer functions shaping techniques have been used. Then, a comparison against a conventionally actuated quadrotor is carried out, showing an increase in the performance and stability of the new actuation strategy. And, based on the results obtained, some improvement suggestions are made to exploit in full the potential of this gyroscopic actuation strategy.

This chapter is in common with Al-Rihani's thesis, [2].

5.2 Control Allocator

5.2.1 Introduction

The vehicle has 12 control inputs, one motor, one servoblock and one pushpull for each of the 4 arms. The system is also highly nonlinear, as it can be seen in the equations of the modelling chapter. Hence, designing a control system can be very challenging if all the control inputs have to be managed in the same design process. That is why, it arises the need to abstract from those 12 inputs several meaningful control commands, such as force and moment commands, which will allow to design a much simpler controller. This approach is usually undertaken is the design of control system for air vehicle. To do that, it is needed some kind of logic to distribute this commanded forces and moments into a combination of the different actuators. In other words, since it does not exist a direct relationship (in terms of meaningful moments) between the actuator effects and the its commands, an algorithm is needed to translate, for example, a pitch command into a combination of the vehicle's physical actuators. It was consequently decided that a control allocator would be the best alternative

In this section, first, the control allocation problem is outlined. Second, it is motivated the use of a linear control allocation method based on a Weighted Pseudoinverse. Third, the control effectiveness or B matrix is developed. And, fourth and finally, the selection of the weights for the control allocation is carried out in order to shape the dynamic response of the actuators.

Nonlinear Control Allocation

First, let us set up the nonlinear control allocation problem (the following derivation was adapted from [19]). Consider the system given by:

$$\dot{\mathbf{x}} = f(t, \mathbf{x}, \mathbf{v}) \quad (5.1)$$

$$\mathbf{v} = h(t, \mathbf{x}, \mathbf{u}) \quad (5.2)$$

where $t \geq 0$ is time, $\mathbf{x} \in \mathbb{R}^r$ is the state vector, $\mathbf{u} \in \mathbb{R}^m$ is the physical actuators input vector and $\mathbf{v} \in \mathbb{R}^n$ is the virtual control commands vector. And the virtual control commands are issued by a controller, k , such that:

$$\mathbf{v}_c = k(t, x) \quad (5.3)$$

The control allocation problem is to solve the system of algebraic equations 5.2 with respect to the control input vector \mathbf{u} so that $\mathbf{v} = \mathbf{v}_c$. Since only over-actuated ($m > n$) systems are being considered, there are, in general, infinite solutions that make $\mathbf{v} = \mathbf{v}_c$. A cost function is usually established, $J(t, \mathbf{x}, \mathbf{u})$ to discriminate between “good” and “bad” solutions of the problem. This cost function may include criteria such as energy consumption, total deflection and saturation limits among others. Thus, the nonlinear control allocation can be casted down to:

$$\min_{\mathbf{u}} J(t, \mathbf{x}, \mathbf{u}) \quad \text{subject to} \quad \mathbf{v}_c - h(t, \mathbf{x}, \mathbf{u}) = 0 \quad (5.4)$$

If properly set up, this nonlinear optimisation problem could yield to optimal solutions, but, there is no general analytical solution for this problem. As a consequence, an online numerical scheme should be applied. However, running an online optimisation algorithm would require a high computational power that was not available onboard with the flight computer that the vehicle has.

To overcome this problem, the sight was turned to linear control allocation. Because, in linear control allocation there are, in contrast, several methods based on analytical solutions that require minimal computational power. Hence, it was decided to linearise the function h , $\mathbf{v} = h(t, x, u) \approx B\mathbf{u}$ and use conventional linear control allocation techniques.

This decision has several drawbacks and advantages. Among the drawbacks is that the Allocator will be satisfactory as long as the linearisation assumption hold. And the advantages are that since it is a much more studied field closed form analytical solutions exists such that require much less computational power than a online optimisation scheme for a nonlinear allocator.

Linear Control Allocation

In order to be able to use linear control allocation techniques, the approach followed in the project was to linearise the function $h(t, \mathbf{x}, \mathbf{u})$ such that:

$$\mathbf{v} = h(t, \mathbf{x}, \mathbf{u}) \approx B\mathbf{u} \quad (5.5)$$

This means that the virtual commands must be expressed as a linear combination of the physical control inputs. In equation 5.5, B matrix is the control effectiveness matrix, and it contains all the linear relationships between virtual commands and physical control inputs. The way to find the B matrix will be developed later on in this section. Now the linear control allocation problem will be introduced.

The classical linear control allocation problem can be defined as below. *Given the virtual control command \mathbf{v} , find the physical control input command \mathbf{u} such that*

$$\mathbf{v} = B\mathbf{u} \quad (5.6)$$

where $\mathbf{u} \in \mathbb{R}^m$ is the physical actuators input vector, $\mathbf{v} \in \mathbb{R}^n$ is the virtual control commands vector and $B \in \mathbb{R}^{n \times m}$ is the control effectiveness matrix. The actual actuators have a bounded envelope of attainable actions given by:

$$\underline{\mathbf{u}} \leq \mathbf{u} \leq \bar{\mathbf{u}} \quad (5.7)$$

where $\bar{\mathbf{u}}$ and $\underline{\mathbf{u}}$ are, respectively, the upper and lower saturation limits of the actuators physical input.

When $m > n$ the system is overactuated, that is, it has more physical control inputs than control objectives. In general, an infinite number of solutions exists so the most suitable one has to be selected. This depends, again, on the cost function $J(\mathbf{u})$, which includes the different relevant fitness criteria and costs to rank the different combinations of \mathbf{u} that give the same commanded \mathbf{v}_c . Therefore, the control allocation problem becomes:

$$\min_{\mathbf{u}} J(\mathbf{u}) \quad \text{subject to} \quad \mathbf{v}_c - B\mathbf{u} = 0 \quad (5.8)$$

The reason to use control linear allocation was, fundamentally, the existence of analytical solutions. Depending on the cost function $J(\mathbf{u})$ this problem will have an analytical solution or will have none at all. Looking in the literature, it was found that the most appropriate was to set up a cost function that minimise the controller deflection to prevent the problem of the servos saturating due to its small deflection envelope. The cost function, $J(\mathbf{u})$, given by:

$$J(\mathbf{u}) = \frac{1}{2} \mathbf{u}^T \mathbf{u} \quad (5.9)$$

when minimised, it minimises the total deflection, hence, helping to prevent actuator saturation, and thus, alleviating the servo saturation risk. Now, if all the constraints of the control inputs are raised, there is, a very elegant, analytical solution given by:

$$\mathbf{u} = B^T (BB^T)^{-1} \mathbf{v} \quad (5.10)$$

If $\frac{1}{2} \mathbf{u}^T \mathbf{u}$ is minimised, the total control action is consequently minimised, thus it can be seen as a minimum distance, minimum energy, or minimum deflection approach.

This solution is extremely valuable, since it allows a pre-computation of the matrix $B^T(BB^T)^{-1}$ and its implementation with a very small computation load while maintaining the optimality of the solution. This is called the Pseudoinverse method, since $B^T(BB^T)^{-1}$ represents the pseudoinverse of B and is one of the most used methods in practical control allocation with many applications across different fields.

A variation of this method is the Weighted Pseudoinverse method, which includes the positive diagonal matrix $W \in \mathbb{R}^{m \times m}$ in the cost function to scale the different control inputs. W could be used to rank relevance or cost of the different physical control inputs. Thus, in this method $J(\mathbf{u})$ is given by:

$$J(\mathbf{u}) = \frac{1}{2} \mathbf{u}^T W \mathbf{u} \quad (5.11)$$

and the solution to the problem:

$$\min_{\mathbf{u}} \frac{1}{2} \mathbf{u}^T W \mathbf{u} \quad \text{subject to} \quad \mathbf{v}_c - B \mathbf{u} = 0 \quad (5.12)$$

is given by:

$$\mathbf{u} = W^{-1} B^T (B W^{-1} B^T)^{-1} \mathbf{v} \quad (5.13)$$

Consequently the matrix $B^* \in \mathbb{R}^{m \times n}$ can be defined, its called the Weighted Pseudoinverse Matrix and is given by:

$$B^* = W^{-1} B^T (B W^{-1} B^T)^{-1} \quad (5.14)$$

Which leads to the very simple, yet effective, control allocator logic given by:

$$\mathbf{u} = B^* \mathbf{v}_c \quad (5.15)$$

Which allows to, given the virtual control command \mathbf{v}_c , find the “best” combination of physical actuators \mathbf{u} , according to $\frac{1}{2} \mathbf{u}^T W \mathbf{u}$, by doing just a simple matrix multiplication by a vector.

The main advantages of this method are:

- It is **optimal**, as it optimises the function $\frac{1}{2} \mathbf{u}^T W \mathbf{u}$. The designer can, therefore, shape the W , knowing that optimality is guaranteed as long as the constraints are not violated and the linearity is maintained.
- It is **analytical**, and consequently, B^* can be calculated beforehand. Or, at least, recalculated online much faster than a numerical optimisation scheme. If B^* is pre-calculated, the only computation to be carried out onboard is a matrix multiplication by a vector, $B^* \mathbf{v}$, to find out the input vector \mathbf{u} and allowing for fast loop executions even in relatively simple microcontrollers.
- It allows to **choose the preferred actuators**. The use of the W weighting matrix allows to discriminate between the different inputs, hence, enabling the designer to rank them and shape the response. It also allows to introduce criteria such as minimum drag or minimum energy in the selection of the weights in W .

- It can be used in **fault tolerant** systems. If some logic of fault detection had to be introduced, this could cope with actuator failures. By zeroing the columns of the B matrix corresponding to the faulty actuators and calculating the new B^* online it could readapt the allocator requiring relative small computation time. And, if B^* is recalculated, there is no need to retune the controller since the new B^* would use the remaining actuators to obtain the virtual commands issued by the controller.

Nevertheless this approach also has caveats, they mainly are:

- It assumes **linearity**, so it only works as long as the linearisation assumptions hold. It could also be recalculated online by setting B as a function of the states x and recalculating it at every loop B^* , although neither optimality nor robustness are guaranteed.
- It does not include the **saturation constraints**. There are some solutions, however, that exist for this situation, one of them is Pseudoinverse Redistribution (PIR). PIR is based on setting the saturated actuators to the saturation points and zeroing its columns in the B matrix, recalculating submatrices of B^* to find the new combinations of the remaining non-saturated actuators and executing this process recursively while unsaturated actuators exist. This approach, although is not optimal, it could be executed relatively fast and yield solutions equal or relatively close to the desired commands.

The controller was aimed to be a stability control augmentation system, SCAS, around the hover state and not to separate excessively from the operating point, so it was considered that neither linearity nor saturation would become a problem. Thus, given the advantages outlined before, it was decided that the best way to go to obtain a working allocator was to use the Weighted Pseudoinverse approach.

5.2.2 Control Allocation for Dual Axis Tilt Rotorcraft

The control allocation problem for the dual-axis tilt rotorcraft will be formulated throughout this section.

The controller has to be a Stability Control Augmentation System that receives the Pitch, Roll and Thrust from the pilot transmitter and the vehicle motion from the sensor and issues the virtual commands, 3 control moments and the desired total thrust. The structure is illustrated in figure 5.2.

Thus, the virtual commands are:

$$\mathbf{v} = \begin{bmatrix} M \\ N \\ L \\ T \end{bmatrix} \quad (5.16)$$

where M , N , and L are the Roll, Pitch and Yaw moments and T is the Thrust. The physical control inputs are:

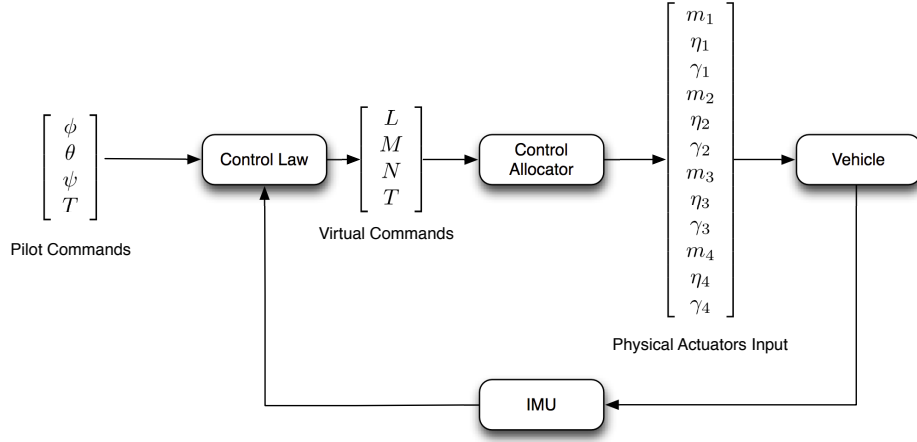


Figure 5.2: Main structure of the control system.

$$\mathbf{u} = \begin{bmatrix} m_1 \\ \eta_1 \\ \gamma_1 \\ m_2 \\ \eta_2 \\ \gamma_2 \\ m_3 \\ \eta_3 \\ \gamma_3 \\ m_4 \\ \eta_4 \\ \gamma_4 \end{bmatrix} \quad (5.17)$$

where m is the motor input, η the servoblock input, γ the pushpull command and subscripts denote the number of the arm.

The control allocator used will be the linear Weighted Pseudoinverse method described in the previous section, therefore, the dimensions of matrices for the solution of the control allocator of the vehicle will be:

$$B \in \mathbb{R}^{4 \times 12} \quad W \in \mathbb{R}^{12 \times 12} \quad B^* \in \mathbb{R}^{12 \times 4} \quad (5.18)$$

Find the actuators commands \mathbf{u} such that:

$$\mathbf{v} = B\mathbf{u} \quad (5.19)$$

subject to:

$$\underline{\mathbf{u}} \leq \mathbf{u} \leq \bar{\mathbf{u}} \quad (5.20)$$

where $\mathbf{u} \in \mathbb{R}^{12}$ is the physical actuators input vector, $\mathbf{v} \in \mathbb{R}^4$ is the virtual control commands vector and $B \in \mathbb{R}^{4 \times 12}$ is the control effectiveness matrix.

where B is the control effectiveness matrix, \mathbf{u} is the actual control inputs to the vehicle and $\bar{\mathbf{u}}$ and $\underline{\mathbf{u}}$ are the upper and lower limits.

5.2.3 Derivation of the submatrix B for the standard arm

The linearisation of the actuator function will be carried out in this section, whose aim is to find the matrix B so that:

$$\mathbf{v} = h(t, \mathbf{x}, \mathbf{u}) \approx B\mathbf{u} \quad (5.21)$$

where $t \geq 0$ is time, $\mathbf{x} \in \mathbb{R}^r$ is the state vector, $\mathbf{u} \in \mathbb{R}^m$ is the physical actuators input vector and $\mathbf{v} \in \mathbb{R}^n$. And the function h is a nonlinear function of the time, t , the state vector, \mathbf{x} , and the physical control inputs \mathbf{u} that maps the effects of the physical control inputs to the Roll, Pitch, Yaw moments and thrust.

Then, finding B will be to find a reasonable approximation by which, independently of the state and time, Roll, Pitch, Yaw moments and thrust, can be approximated as a linear combination of the physical control commands. In order to accomplish this, the approach followed was to analyse each effect of each actuator, in terms of moments and forces, and to approximate it in a linear manner.

Previous Remarks

Instead of developing all the relationships for every single actuators, taking advantage of the symmetry of the vehicle, all the derivation process for the B matrix will be carried out with respect a so-called standard arm which is described in Figure 5.3. This is the same approach followed with the derivation of the rigid body equations. The standard arm is, thus, in the position of Arm 3 in the vehicle, the propeller rotates clockwise from above, which means that the angular velocity is positive. Once the relations are known for the standard arm, the ones for the other arms can be derived by simply rotating the reference frame accordingly and introducing whether the angular velocity is positive or negative.

Qualitative Comparison of Actuator Features

In the following section, a linearisation of the control actions will be carried out. However, it is worthy to have a previous look at the different time scales and characteristics of the actuators. Let us compare the two main actuator actions present in this vehicle:

- **Thrust.** It is the main aerodynamic force and it creates moments by differential thrust of the motors. Its dynamics is given by the transfer function of the motor:

$$G_{\text{motor}} = \frac{e^{-0.035s}9.19}{(1 + 0.16s)} \quad (5.22)$$

The actions are given by the thrust itself and so, it is steady in time.

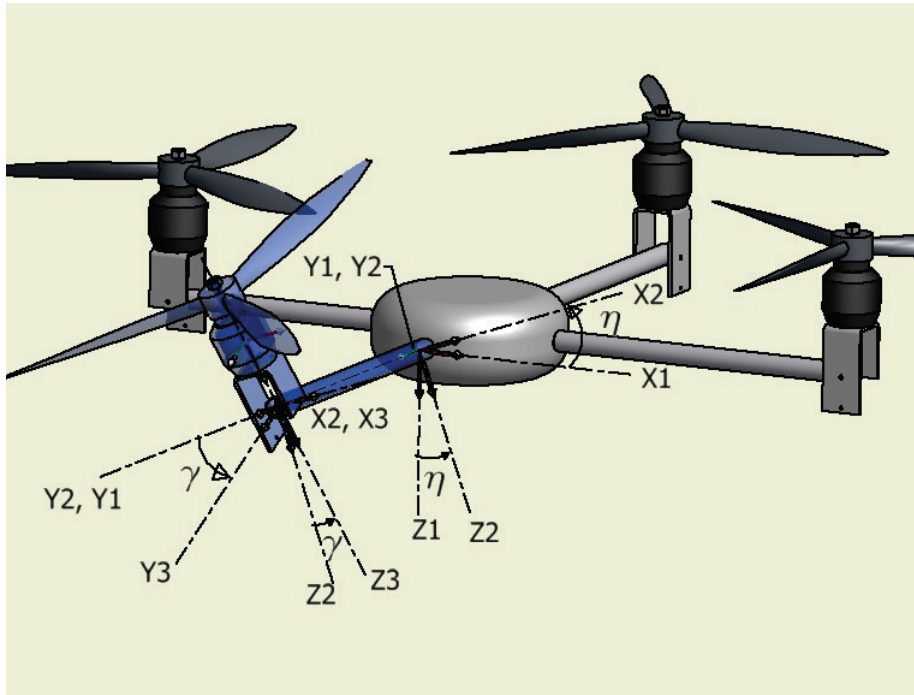


Figure 5.3: Standard Arm and definition of the angles.

- **Gyroscopic Effects.** They are moments that are due to terms of the kind $M = J\Omega\dot{\eta}$. Therefore their dynamics are given by the transfer functions of the servos:

$$G_{\text{servoblock}} = \frac{1228.05}{1228.05 + 49.18s + s^2} \quad (5.23)$$

Their actions are given by the derivative terms of η , so they will only exist if η is changing, that is, during the time that the servo moves from the previous position to the next position. Thus, they will decay with time.

Now let's compare them, the gyroscopic effects are transient and ephemeral. They all depend on time derivatives which in turn depend upon the dynamics of the servoblock servo the characteristics of its dynamics are (from equation 5.23) $\omega_n \approx 35$ and $\xi \approx 0.7$ which yield a settling time (95%) of $t_{s\text{Servo}} \approx \frac{3}{\xi\omega_n} = 0.12\text{s}$. But this effect decays in time, so that the moment appears while the servo is travelling to the requested position but it disappears when it stops. By contrast to the Motor dynamics are relatively slower. They are composed by a first order system with a time constant $\tau_{\text{Motor}} = 0.16$ and a pure delay with a delay time of $\theta = 0.035\text{s}$. Hence, its settling time is given by $t_{s\text{Motor}} \approx 3\tau + \theta = 0.52\text{s}$. Its effects, however, do not decay in time as it happens with the gyroscopic effects.

Two clearly differentiated time scales appear, on one side the fast and transient gyroscopic effects and, on the other, the slow and steady effects from the motor. To illustrate this, let's compare the pitching moment response to a step of both actions. In figure 5.4, the gyroscopic effect of the servoblock ($\dot{\eta}\Omega J$) is illustrated. As it can be seen it is a very fast "spike" with relatively large amplitude that disappears with time. On the other hand, in figure 5.5, the torque generated by a differential command in the motors is shown compared to the gyroscopic effect, and it is slower although its action does not decay with time.

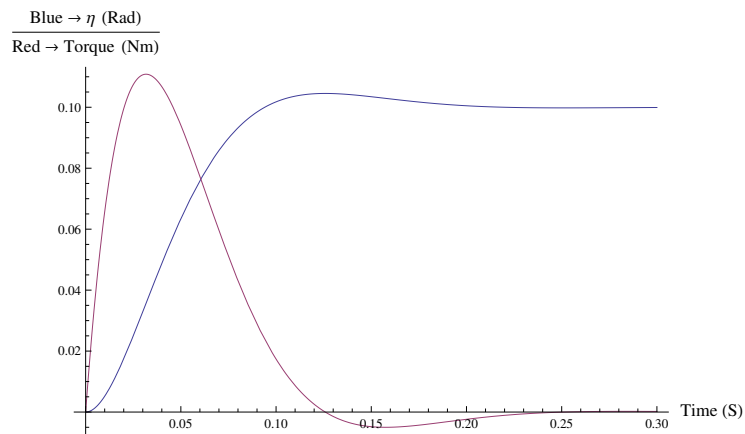


Figure 5.4: Response of the servo and the gyroscopic pitching moment to an input of 0.1(rad) in the servoblock servo at time 0. Note time scale $\approx 0.2s$

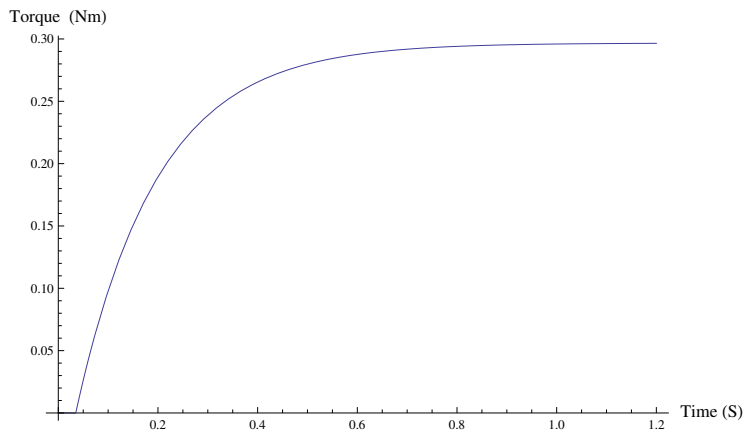


Figure 5.5: Pitching moment response generated by the motors following a differential step of 1% in throttle at time 0. Note time scale $\approx 0.8s$

Hereafter an analysis of the linearisation of each actuator's effects will be carried out, starting with the motors, following with the servoblock servo and finishing with the pushpull servo.

Action of the Motor

The actions with respect to the centre of gravity created by the motor are described as follows:

Thrust. It has been seen in the modelling chapter that it depends linearly upon the throttle command, refer to figure 4.12, therefore, it can be linearised around an operating point, in this case 50% throttle, so that the thrust is expressed by:

$$T = \mu(U_{0_Motor} + \Delta U_{Motor}) = T_0 + \Delta T_{Motor} \quad (5.24)$$

where μ is the slope of the Throttle vs Thrust line.

This way the virtual command ΔT is related to the motor input by:

$$\Delta T_{Motor} = \mu(\Delta U_{Motor}) \quad (5.25)$$

The thrust also creates another moment, the **thrust torque**, as the application point of the thrust is not in the CG and therefore it creates a moment around the CG. The moment will then be given by

$$\Delta \mathbf{M}_{Motor} = \mathbf{r}_{Hub2CG} \times \Delta \mathbf{T}_{Motor} = \begin{bmatrix} 0 \\ L \\ -H \end{bmatrix} \times \begin{bmatrix} 0 \\ 0 \\ -\mu(\Delta U_{Motor}) \end{bmatrix} = \begin{bmatrix} -L\mu(\Delta U_{Motor}) \\ 0 \\ 0 \end{bmatrix} \quad (5.26)$$

where \mathbf{r}_{Hub2CG} is the position vector from the CG to the propeller hub, the point of application of the thrust force. L is the length of the arm, from the CG, and H is the height of the propeller hub respect to the CG.

The other action created by the motor is the **drag torque**. Like the thrust it also exhibits a linear behaviour, then, similarly to equation 5.27 it can be defined as:

$$Q = \pm\kappa(Q_0 + \Delta U_{Motor}) \quad (5.27)$$

and

$$\Delta Q = \pm\kappa(\Delta U_{Motor}) \quad (5.28)$$

where κ is the slope of the Throttle vs Drag Torque line. This torque is dependant on the direction of rotation, its direction can be $+z$ or $-z$, it will be either positive if it is rotating clockwise from above or negative if it is rotating anticlockwise from above.

Summing up all this contributions the virtual commands generated by the motor are then:

$$B_{Motor} = \begin{bmatrix} 0 \\ 0 \\ 0 \\ \mu \end{bmatrix} + \begin{bmatrix} 0 \\ 0 \\ \pm\kappa \\ 0 \end{bmatrix} + \begin{bmatrix} -L\mu \\ 0 \\ 0 \\ 0 \end{bmatrix} = \begin{bmatrix} -L\mu \\ 0 \\ \pm\kappa \\ \mu \end{bmatrix} \quad (5.29)$$

Action of the Servoblock Servo

In the previous chapter it has been shown that the actuators create two main actions: those given by the aerodynamics and those created by the rigid body or gyroscopic effects. In order to develop a linearised approximation to be used in the B matrix of the effects of the servoblock, the approach will follow two sides, the Aerodynamic and the Rigid Body.

The main aerodynamic action is the thrust, hence, the effect of the Servoblock will be the projection of this thrust and the torques that this projections create. In order to find out the projection originated due to a small angle η of servoblock, the rotation matrix must be firstly found:

$$R_{\text{ServoBlock}} = \begin{bmatrix} \cos \eta & 0 & \sin \eta \\ 0 & 1 & 0 \\ -\sin \eta & 0 & \cos \eta \end{bmatrix} \quad (5.30)$$

η is small and so the trigonometric functions are approximated:

$$R_{\text{ServoBlock}} \approx \begin{bmatrix} 1 & 0 & \eta \\ 0 & 1 & 0 \\ -\eta & 0 & 1 \end{bmatrix} \quad (5.31)$$

Therefore to project the thrust:

$$\mathbf{T}_{\text{Servoblock}} = R_{\text{ServoBlock}} \mathbf{T}_0 = \begin{bmatrix} 1 & 0 & \eta \\ 0 & 1 & 0 \\ -\eta & 0 & 1 \end{bmatrix} \begin{bmatrix} 0 \\ 0 \\ -T_0 \end{bmatrix} = \begin{bmatrix} -T_0 \eta \\ 0 \\ -T_0 \end{bmatrix} \quad (5.32)$$

Now, it is only relevant the part proportional to the deflection angle η therefore, the term in the z axis must be dropped yielding:

$$\Delta \mathbf{T}_{\text{Servoblock}} = \begin{bmatrix} -T_0 \\ 0 \\ 0 \end{bmatrix} \eta \quad (5.33)$$

Then, the action of the servoblock will be the **moment** created by the **projection of the thrust** in the x axis, which is:

$$\Delta \mathbf{M}_{\text{ServoblockThrust}} = \mathbf{r}_{\text{Hub2CG}} \times \Delta \mathbf{T}_{\text{Servoblock}} = \begin{bmatrix} 0 \\ L \\ -H \end{bmatrix} \times \begin{bmatrix} -T_0 \\ 0 \\ 0 \end{bmatrix} \eta = \begin{bmatrix} 0 \\ HT_0 \\ LT_0 \end{bmatrix} \eta \quad (5.34)$$

Hence, the B matrix column of the servoblock contribution from the thrust terms is:

$$B_{\text{ServoblockThrust}} = \begin{bmatrix} 0 \\ HT_0 \\ LT_0 \\ 0 \end{bmatrix} \quad (5.35)$$

Now, let us analyse the Rigid Body or Gyroscopic terms.

Our objective is to find a way to embed in the B matrix the effect of the Rigid Body motion. In the previous chapter, the equations of the Rigid Body moments have been developed. They result in equation 4.34, which includes all the motions, the vehicle, the servoblock, the pushpull and the motor. At this point, the focus is on the servoblock action. By removing from equation 4.34 the terms dependant on the vehicle $p \ q \ r \ \dot{p} \ \dot{q} \ \dot{r}$ and on the motion of the pushpull $\gamma \ \dot{\gamma} \ \ddot{\gamma}$, and assuming that the angular velocity of the propeller is constant or quasi constant, $\dot{\Omega} \approx 0$, it yields the relationship between servoblock actuation and the moments that it creates:

$$\Delta \mathbf{M}_{\text{ServoblockGyro}} = \begin{bmatrix} -I_{xx}\Omega \cos(\eta)\dot{\eta} + I_{yy}\Omega \cos(\eta)\dot{\eta} - I_{zz}\Omega \cos(\eta)\dot{\eta} \\ -I_{yy}\ddot{\eta} \\ I_{xx}\Omega \sin(\eta)\dot{\eta} - I_{yy}\Omega \sin(\eta)\dot{\eta} + I_{zz}\Omega \sin(\eta)\dot{\eta} \end{bmatrix} \quad (5.36)$$

Since the rotating assembly is symmetric, 3-blade prop, so $I_{yy} = I_{xx}$. Defining $I = I_{yy} = I_{xx}$ and $I_{zz} = J$, gives:

$$\Delta \mathbf{M}_{\text{ServoblockGyro}} = \begin{bmatrix} -J\Omega \cos(\eta)\dot{\eta} \\ -I\ddot{\eta} \\ J\Omega \sin(\eta)\dot{\eta} \end{bmatrix} \quad (5.37)$$

Continuing with the analysis, around the operating point, η is small and so the trigonometric terms can be approximated by $\sin \eta \approx \eta$ and $\cos \eta \approx 1$. Hence:

$$\Delta \mathbf{M}_{\text{ServoblockGyro}} = \begin{bmatrix} -J\Omega\dot{\eta} \\ -I\ddot{\eta} \\ J\Omega\eta\dot{\eta} \end{bmatrix} \quad (5.38)$$

Now, to simplify this further, an analysis of the order of magnitude of each term will be conducted. Taking into account that the inertia tensor of the propeller spinning assembly is given by:

$$\mathbf{I}_{\text{blade}} = \begin{bmatrix} 69.4 & 0 & 0 \\ 0 & 69.4 & 0 \\ 0 & 0 & 110.9 \end{bmatrix} \text{ kg mm}^2 \quad (5.39)$$

Around the operating point the variables involved have the following orders of magnitude:

- Inertia $J \approx 10^{-4}$
- Inertia $I \approx 10^{-5}$
- Angular velocity $\Omega \approx 10^2$
- Deflection angle $\eta \approx 10^{-1}$
- Deflection angle rate $\dot{\eta} \approx \frac{\eta}{t_{\text{servo}}} \approx \frac{10^{-1}}{10^{-1}} \approx 1 = 10^0$
- Rate of the deflection angle rate $\ddot{\eta} \approx \frac{\dot{\eta}}{t_{\text{servo}}} \approx \frac{10^0}{10^{-1}} \approx 10 = 10^1$

Introducing this into equation 5.38:

$$\begin{bmatrix} -J\Omega\dot{\eta} \\ -I\ddot{\eta} \\ J\Omega\eta\dot{\eta} \end{bmatrix} \approx \begin{bmatrix} -10^{-4}10^210^0 \\ -10^{-5}10^1 \\ 10^{-4}10^210^{-1}10^0 \end{bmatrix} = \begin{bmatrix} -10^{-2} \\ -10^{-4} \\ 10^{-3} \end{bmatrix} \quad (5.40)$$

from where it can be concluded that the most relevant action of the servoblock from the gyroscopic effects is the term in x that is:

$$\Delta\mathbf{M}_{x_{\text{ServoblockGyro}}} = -J\Omega\dot{\eta} \quad (5.41)$$

which, on the other hand, is the classical shape that the equations of the gyroscopic effect take in its simplest form.

This angle, is governed by the servo motor dynamics, equation 5.23. To express $\dot{\eta}$ iproportionally to η , it is assumd that the angular rate $\dot{\eta}$ is the average, that is the steady state value η divided by the rise time $t_r = \frac{\pi - \arctan \frac{\sqrt{1-\xi^2}}{\xi}}{\omega_n \sqrt{1-\xi^2}} = 0.09$, i.e. $\dot{\eta} \approx \frac{\eta}{t_r}$. Note that this is somehow unrealistic since even though the magnitude might be close as it is the average, it does not reflect the transient nature of the motion.

Then, $\Delta\mathbf{M}_{x_{\text{ServoblockGyro}}}$ the **action of the servoblock from the gyroscopic effects** can be simplified by using the approximation of the average angular rate described before, hence:

$$\Delta\mathbf{M}_{x_{\text{ServoblockGyro}}} = -J\Omega\dot{\eta} \approx -J\Omega\frac{\eta}{t_r} \quad (5.42)$$

$$B_{\text{ServoblockGyro}} = \begin{bmatrix} \frac{-J\Omega}{t_r} \\ 0 \\ 0 \\ 0 \end{bmatrix} \quad (5.43)$$

Now summing up the two contributions from the Thrust Projection side and from the gyroscopic side we have that the action of the servoblock is given by:

$$B_{\text{Servoblock}} = B_{\text{ServoblockThrust}} + B_{\text{ServoblockGyro}} = \begin{bmatrix} 0 \\ HT_0 \\ LT_0 \\ 0 \end{bmatrix} + \begin{bmatrix} \frac{-J\Omega}{t_r} \\ 0 \\ 0 \\ 0 \end{bmatrix} = \begin{bmatrix} \frac{-J\Omega}{t_r} \\ HT_0 \\ LT_0 \\ 0 \end{bmatrix} \quad (5.44)$$

Action of the Push-Pull Servo

Similarly as with the Servoblock, the actions of the push-pull servo are in both sides, from the gyroscopic effects and from the moments created by the projection of thrust.

The thrust rotation is given by the rotation matrix of the push pull, which can be simplified due to the fact that γ is bounded and relatively small:

$$R_{\text{Push Pull}} = \begin{bmatrix} 1 & 0 & 0 \\ 0 & \cos(\gamma) & -\sin(\gamma) \\ 0 & \sin(\gamma) & \cos(\gamma) \end{bmatrix} \approx \begin{bmatrix} 1 & 0 & 0 \\ 0 & 1 & -\gamma \\ 0 & \gamma & 1 \end{bmatrix} \quad (5.45)$$

Now rotating the nominal thrust \mathbf{T}_0 gives:

$$T_{\text{Push-Pull}} = R_{\text{Push Pull}} \mathbf{T}_0 = \begin{bmatrix} 1 & 0 & 0 \\ 0 & 1 & -\gamma \\ 0 & \gamma & 1 \end{bmatrix} \begin{bmatrix} 0 \\ 0 \\ -T_0 \end{bmatrix} = \begin{bmatrix} 0 \\ -\gamma T_0 \\ T_0 \end{bmatrix} \quad (5.46)$$

Similarly, as has been done with the servoblock, only the term proportional to γ is kept:

$$\Delta \mathbf{T}_{\text{Push Pull}} = \begin{bmatrix} 0 \\ -T_0 \\ 0 \end{bmatrix} \gamma \quad (5.47)$$

The actual action that the push pull creates is the **moment of the projected thrust** $\Delta \mathbf{T}_{\text{Push Pull}}$

$$\Delta \mathbf{M}_{\text{Push Pull}} = \mathbf{r}_{\text{Hub2CG}} \times \Delta \mathbf{T}_{\text{Push Pull}} = \begin{bmatrix} 0 \\ L \\ -H \end{bmatrix} \times \begin{bmatrix} 0 \\ -T_0 \\ 0 \end{bmatrix} \gamma = \begin{bmatrix} HT_0 \\ 0 \\ 0 \end{bmatrix} \gamma \quad (5.48)$$

Therefore, the B matrix column of the push pull contribution from the thrust terms is:

$$B_{\text{Push Pull Thrust}} = \begin{bmatrix} HT_0 \\ 0 \\ 0 \\ 0 \end{bmatrix} \gamma \quad (5.49)$$

Now the analysis of the gyroscopic effects of the Push Pull will be carried out. To uncover the effect of the Push Pull from the full equations of the rigid body, equation 4.34, all the other terms must be removed. These terms are those dependant on the vehicle motion, $p \ q \ r \ \dot{p} \ \dot{q} \ \dot{r}$, and those on the motion of the servoblock $\eta \ \dot{\eta} \ \ddot{\eta}$. It has also been assumed that the angular velocity of the propeller is constant or quasi constant, $\dot{\Omega} \approx 0$. All these simplifications yield the relationship between Push Pull actuation and the moments created by the gyroscopic effects:

$$M_{\text{Push Pull}} = \begin{bmatrix} -I_{xx}\Omega \cos(\gamma)\dot{\gamma} + I_{yy}\Omega \cos(\gamma)\dot{\gamma} + I_{zz}\Omega \cos(\gamma)\dot{\gamma} \\ -I_{xx}\Omega \sin(\gamma)\dot{\gamma} + I_{yy}\Omega \sin(\gamma)\dot{\gamma} + I_{zz}\Omega \sin(\gamma)\dot{\gamma} \end{bmatrix} \quad (5.50)$$

Likewise the simplifications carried out before with the Servoblock, introducing that the inertia tensor is symmetric and that $I_{yy} = I_{xx}$. Naming $I =$

$I_{yy} = I_{xx}$ and $I_{zz} = J$. And also approximating the trigonometric functions yield:

$$M_{\text{Push Pull}} = \begin{bmatrix} -I\ddot{\gamma} \\ J\Omega\dot{\gamma} \\ J\Omega\gamma\dot{\gamma} \end{bmatrix} \quad (5.51)$$

The transfer function of the Push Pull servo is very similar in terms of its characteristics to that of the servoblock, therefore the same order of magnitude analysis holds true for this case. Hence the terms in x and z can be neglected and it can be assumed that the only relevant term is the term in y:

$$M_{y\text{Push Pull}} = J\Omega\dot{\gamma} \quad (5.52)$$

And introducing an equivalent approximation for the angular rate, $\dot{\gamma} \approx \frac{\gamma}{t_r}$:

$$M_{y\text{Push Pull}} = J\Omega\dot{\gamma} \approx J\Omega\frac{\gamma}{t_r} \quad (5.53)$$

Whose contribution to the B matrix column of the Push Pull is:

$$B_{\text{Push Pull}_{\text{Gyro}}} = \begin{bmatrix} 0 \\ \frac{J\Omega}{t_r} \\ 0 \\ 0 \end{bmatrix} \quad (5.54)$$

Since the dynamics of both servos are very similar from now on, $t_{r\text{Servoblock}} \approx t_{r\text{Pushpull}} \approx t_r$.

Summarising the B column of the push pull is given by the sum of the contribution of the thrust and the contribution of the rigid body or gyroscopic terms.

$$B_{\text{Push Pull}} = B_{\text{Push Pull}_{\text{Thrust}}} + B_{\text{Push Pull}_{\text{Gyro}}} = \begin{bmatrix} HT_0 \\ 0 \\ 0 \\ 0 \end{bmatrix} + \begin{bmatrix} 0 \\ \frac{J\Omega}{t_r} \\ 0 \\ 0 \end{bmatrix} = \begin{bmatrix} HT_0 \\ \frac{J\Omega}{t_r} \\ 0 \\ 0 \end{bmatrix} \quad (5.55)$$

Submatrix B of the Standard Arm

Once the action of each individual actuator in the standard arm is known, it is time to join them up in the same B sumatrix:

$$B_{\text{Standard Arm}} = [B_{\text{Motor}} \quad B_{\text{Servoblock}} \quad B_{\text{Push Pull}}] = \begin{bmatrix} -L\mu & \frac{-J\Omega}{t_r} & HT_0 \\ 0 & HT_0 & \frac{J\Omega}{t_r} \\ \pm\kappa & LT_0 & 0 \\ \mu & 0 & 0 \end{bmatrix} \quad (5.56)$$

5.2.4 B matrix

With the submatrix B known for the standard arm, $B_{\text{Standard Arm}}$, obtaining the B matrix of all the arms is just a matter of rotating the axes. If $R_{\text{Standard 2 n}}$ is the rotation matrix from the standard arm to Arm n, then:

$$B_{\text{Arm n}} = R_{\text{Std2n}} B_{\text{Standard Arm}} \quad (5.57)$$

where R_{Std2n} is the rotation matrix of the axes from the standard arm to the arm number n .

Hence, the last step is to introduce whether the propellers are turning clockwise or anticlockwise in the signs of κ and Ω and assembling all the submatrices B for each arm to form the final B matrix:

$$B = [B_{\text{Arm 1}} \quad B_{\text{Arm 2}} \quad B_{\text{Arm 3}} \quad B_{\text{Arm 4}}] \quad (5.58)$$

expanding:

$$B = \begin{bmatrix} 0 & HT_0 & \frac{J\Omega}{t_r} & 0 & -HT_0 & \frac{J\Omega}{t_r} & -L\mu & \frac{J\Omega}{t_r} & HT_0 & L\mu & \frac{J\Omega}{t_r} & -HT_0 \\ L\mu & \frac{J\Omega}{t_r} & -HT_0 & -L\mu & \frac{J\Omega}{t_r} & HT_0 & 0 & HT_0 & -\frac{J\Omega}{t_r} & 0 & -HT_0 & -\frac{J\Omega}{t_r} \\ -\kappa & LT_0 & 0 & \kappa & LT_0 & 0 & \kappa & LT_0 & 0 & -\kappa & LT_0 & 0 \\ \mu & 0 & 0 & \mu & 0 & 0 & \mu & 0 & 0 & \mu & 0 & 0 \end{bmatrix} \quad (5.59)$$

Equation 5.59 defines the matrix that linearly approximates the physical control inputs to the virtual control commands, forces and moments, by $B\mathbf{u} \approx \mathbf{v}$. At this stage it must be remembered that this is only an approximation in order to use linear control allocation techniques and that the full equivalence between forces and moments should be sought by assembling all the full non-linear equations developed in the modelling chapter. To illustrate it:

$$B\mathbf{u} = \begin{bmatrix} 0 & HT_0 & \frac{J\Omega}{t_r} & 0 & -HT_0 & \frac{J\Omega}{t_r} & -L\mu & \frac{J\Omega}{t_r} & HT_0 & L\mu & \frac{J\Omega}{t_r} & -HT_0 \\ L\mu & \frac{J\Omega}{t_r} & -HT_0 & -L\mu & \frac{J\Omega}{t_r} & HT_0 & 0 & HT_0 & -\frac{J\Omega}{t_r} & 0 & -HT_0 & -\frac{J\Omega}{t_r} \\ -\kappa & LT_0 & 0 & \kappa & LT_0 & 0 & \kappa & LT_0 & 0 & -\kappa & LT_0 & 0 \\ \mu & 0 & 0 & \mu & 0 & 0 & \mu & 0 & 0 & \mu & 0 & 0 \end{bmatrix} \begin{bmatrix} m_1 \\ \eta_1 \\ \gamma_1 \\ m_2 \\ \eta_2 \\ \gamma_2 \\ m_3 \\ \eta_3 \\ \gamma_3 \\ m_4 \\ \eta_4 \\ \gamma_4 \end{bmatrix} \approx \begin{bmatrix} M \\ N \\ L \\ T \end{bmatrix} = \mathbf{v} \quad (5.60)$$

B represents the relation between the inputs, servo angles demands and throttle and the moments created. The units are not the same, so in order to avoid the problems that the different order of magnitudes embedded in the unit representation of the inputs could create, it was decided that the B matrix should be normalised so that all the inputs range from -1 to 1 regardless of whether they are deflection angles or throttle positions. The following has been adapted from the work by [18]. The new normalised B matrix will be represented by \hat{B} . To do so a matrix E is defined whose diagonal term is given by the maximum absolute of the actuator limits, that is, $E_{ii} = \max(|\underline{u}_i|, |\bar{u}_i|)$. Then the normalised B matrix will be given by: $\hat{B} = BE$. Therefore all the inputs will be given by $\hat{\mathbf{u}} = E^{-1}\mathbf{u}$ which is normalised, i.e., $-1 \leq \hat{u}_i \leq 1$.

5.2.5 Weighted Pseudoinverse Control Allocator

The Weighted Pseudoinverse method presents numerous advantages, outlined before, besides its simplicity. For this reason it was the method selected for this project. Now the selection of the weights to design the allocator will be carried out.

In order to design the control allocator, and also the control system, the main focus was on the pitching and rolling motions since, in general terms in this kind of platform, is critical for stability. A very small angle in roll or pitch, and the vehicle will drift due to the projection of thrust. While, on the other hand, the yawing motion is a concern for the orientation of the platform only. The vehicle is symmetric, therefore, the pitching and the roll dynamics and actuation. Hence, although the analysis in the following will be carried out in terms of the pitching moment.

In section 5.2.3 the different qualitative features of the actuator's response has been analysed. Due to its importance they will be summarised now, the main characteristics are described in table 5.2.5. The gyroscopic action is fast and decays with time while the propulsive or motor action is rather slow but persistent in time. The best way to understand its features is by visualising the step response of each actuator. In figure 5.6 the normalised step response of a gyroscopic pitching moment and a propulsive pitching moment are shown together.

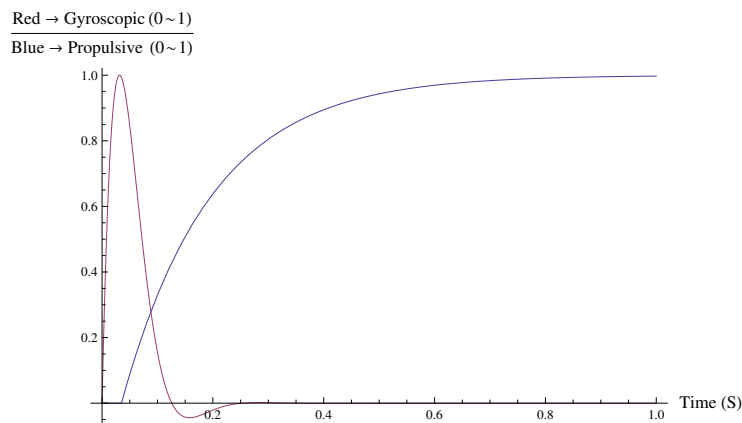


Figure 5.6: Normalised pitching moment response generated by the motors following a differential step and the servo gyroscopic effects following a step at time 0. Note difference in time scales.

The selection of the weighting matrix will decide which is the mix of actuators, and therefore, it will shape the dynamics of the response, how much is fast "spike" and how much is slow motor in figure 5.6. One of main objectives when the tilting feature was added to a conventional quadrotor design was to increase the bandwidth of the actuators exploiting the fact that the servos are

Action	t_r (S)	Permanent
Propulsive	0.12	No
Gyroscopic	0.48	Yes

Table 5.1: Comparison of the speed of te response of both control actions.

much faster than the motors.

The Bandwidth is tightly coupled to the settling time of the response, therefore, reducing the settling time would improve, i.e. increase, the bandwidth of the actuators. At first, it seems that the more servo action in the mix, the faster the system will be, but that would led to an unacceptable overshoot. And too small servo weighting would led to a slow response, like the one of a standard quadrotor. Therefore a trade-off must be found between overshoot and settling time.

The selection of the weights was carried out by using the normalised B matrix, \hat{B} , to avoid that the units could create any undesired scalings. Thus, the control allocator matrix is, then, \hat{B}^* and is given by:

$$\hat{B}^* = W^{-1} \hat{B}^T (\hat{B} W^{-1} \hat{B}^T)^{-1} \quad (5.61)$$

Which, as a reminder, solves the problem:

$$\min_u \frac{1}{2} \mathbf{u}^T W \mathbf{u} \quad \text{subject to} \quad \mathbf{v}_c - B \mathbf{u} = 0 \quad (5.62)$$

The weights of the W matrix are to be selected so that they blend both the gyroscopic effects and the motor action. The higher the element of an actuator is, the higher the cost it will have, and the more it will be minimised, i.e., the least used will be. To do this, a weight w_{motor} such that $0 < w_{\text{motor}} < 1$ was added in the elements corresponding to the motors and a weight $w_{\text{gyro}} = \frac{1-w_{\text{motor}}}{2}$ was added in the elements corresponding to the servos. So that for each arm all the weights were 1, i.e., $1 = w_{\text{gyro}} + w_{\text{gyro}} + w_{\text{motor}}$. Thus, the larger w_{motor} the smaller the use of the motors will be and the larger the use of the servos will be. Summing up, the weighting matrix is given by:

$$W = \begin{bmatrix} w_{\text{motor}} & & & & & & & \\ & w_{\text{gyro}} & & & & & & \\ & & w_{\text{gyro}} & & & & & \\ & & & w_{\text{motor}} & & & & \\ & & & & w_{\text{gyro}} & & & \\ & 0 & & & & \ddots & & \\ & & & & & & & w_{\text{gyro}} \end{bmatrix} \quad \text{where:} \quad w_{\text{gyro}} = \frac{1-w_{\text{motor}}}{2} \quad (5.63)$$

By selecting w_{motor} the relation between motor actuation and gyroscopic, or servo actuation, was altered. Thus, allowing to blend of the servo “kick” and the motor actuation to shape the response of the actuators. This mixing con-

cept is illustrated in figure 5.7.

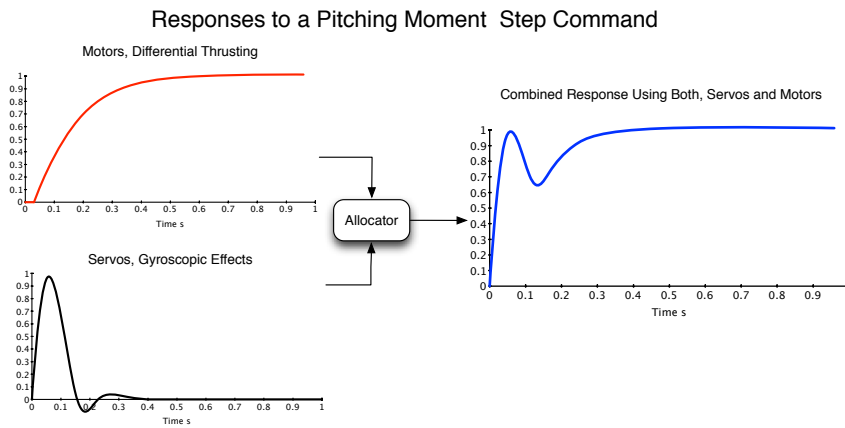


Figure 5.7: Illustration of the concept of the control allocator as a “mixer” of the two kinds of effectors. Note that all the responses are normalised.

To decide which the best blend of actuators was, the full nonlinear simulink model mechanising all the equations (and described in the previous section) was used. Several weights were tested by spanning w_{motor} from 0 to 1, and the response to a step at time 0 in the pitching moment was recorded and normalised. The result is shown in figure 5.8.

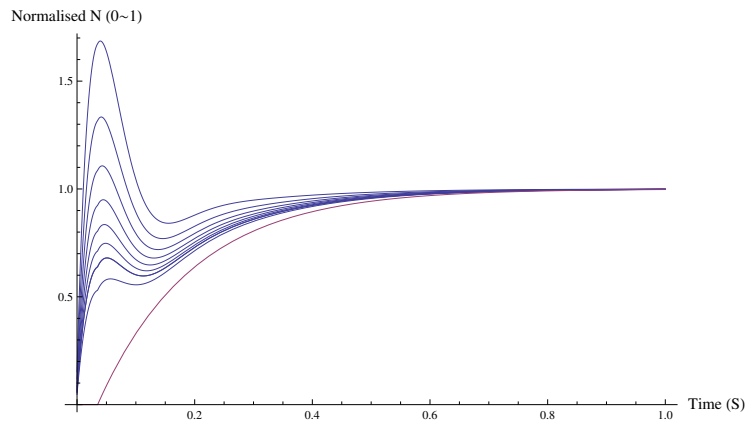


Figure 5.8: Normalised pitching moment response generated by the allocator for different weights w_{motor} ranging from 0 to 1. Note the red line when $w_{\text{motor}} \approx 0$, thus, being basically executed by the motors alone.

From figure 5.8 it can be inferred that too large values of w_{motor} yield responses that have a significant overshoot, while small values of w_{motor} make

the response visibly slower. Another issue to take into account is that, the larger the use of the servos, the larger is the likelihood of them being saturated.

As a trade-off between speed and excessive overshoot, it was decided that a 15% of overshoot would be desirable. To find which was the weight that gave 15% of overshoot, an interpolation from the previous tested weights with its corresponding overshoots was carried out. The solution yielded that the value w_{motor} that makes the overshoot 15% given by $w_{\text{motor}} = 0.994$.

In figure 5.9 the response to a step with the combination given by $w_{\text{motor}} = 0.994$ is shown. In table 5.2.5 all the performance parameters are summarised and compared. It is clear that the response with allocator is faster than with differential thrusting. In the step response, the more evident improvement is on the rise time, which is halved with respect to the motors differential thrusting. The settling time, also, experiences an improvement of almost 20% with respect to the motors differential thrusting. This faster response is also obvious from the bode plot of both effectors shown in figure 5.10, where the new actuator suite brings an order of magnitude improvement in bandwidth. Specially relevant in this figure is the evidence that the non-minimum phase behaviour introduced by the time delay in the motor response is greatly improved by the introduction of the new actuators.

In figure 5.9 the responses for several pitching moments demands ranging from 0 to 1 Nm are shown to demonstrate the linearity of the actuators. This means that range no saturation has occurred and that within this range of demands linearity constraints are not violated. Thus, it can be concluded that the approximations incurred in the linearisation of the control actions in order to obtain the B matrix are relatively accurate in this range. And thus, the B matrix gives a good approximate picture of the control actions. Hence, the control allocator designed based on \hat{B}^* was adopted for the vehicle control. Simulation tests showed that the actuator demands, even when the vehicle was suffering severe perturbations remained below 1Nm, thus, further reinforcing the validity of the allocator designed.

Allocator	Rise T. t_r (s)	Settling T. t_s (s)	Bandwidth. ($\frac{rad}{s}$)
Combination, $w_{\text{motor}} = 0.994$	0.024	0.42	100
Motors Only $w_{\text{motor}} = 0$	0.52	0.52	6.1
Improvement	95%	20%	$\approx 1600\%$

Table 5.2: Comparison of the speed of the response of both control actions.

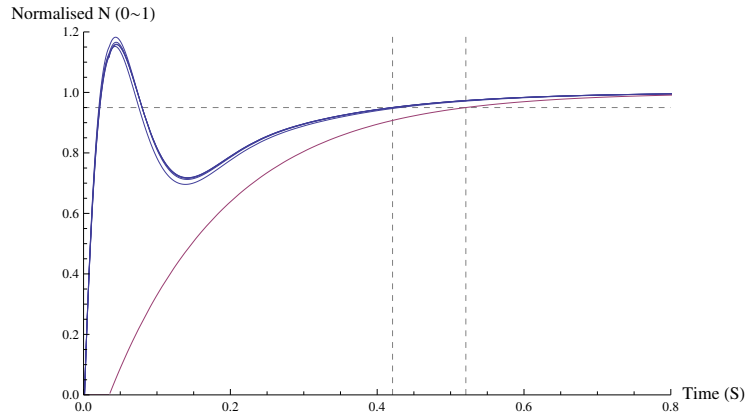


Figure 5.9: Resulting allocator with $w_{\text{motor}} = 0.994$. Blue lines show the responses for several Pitching Moment (N) step commands from 0 to 1 Nm. The red line represents the response when $w_{\text{motor}} \approx 0$. Note the dashed lines showing the settling time (95%) for the two actuator combinations.

5.3 Controller

5.3.1 Introduction

In this section the design of the control law is carried out. First, a simplified plant model is derived in order to tune the controller. Second a methodology to tune the gains of the PD controller described. Third, the performance of the vehicle is compared against a baseline vehicle that would result from conventional actuation. And, fourth and finally, some improvements to de vehicle suggestions are made as a result of the control design.

5.3.2 Simplified Plant Model for Controller Design

Pitch/Roll Dynamics model

In order to apply classical SISO Loop Shaping techniques to the vehicle a simplified model was needed. This model has to capture all the relevant dynamics, thus, the approach followed was to model the vehicle as a mass in the space and the actuators were approximated by a linear transfer function was found to model the actuators.

The dynamics of a mass free in the space with a single rotation axes are given by:

$$I\ddot{\theta} = M(v_p) \quad (5.64)$$

where I is the vehicle moment of Inertia around the y axis, M is the moments in the y axis applied onto the airframe, i.e., pitching moments. And v_p is the pitching moment command.

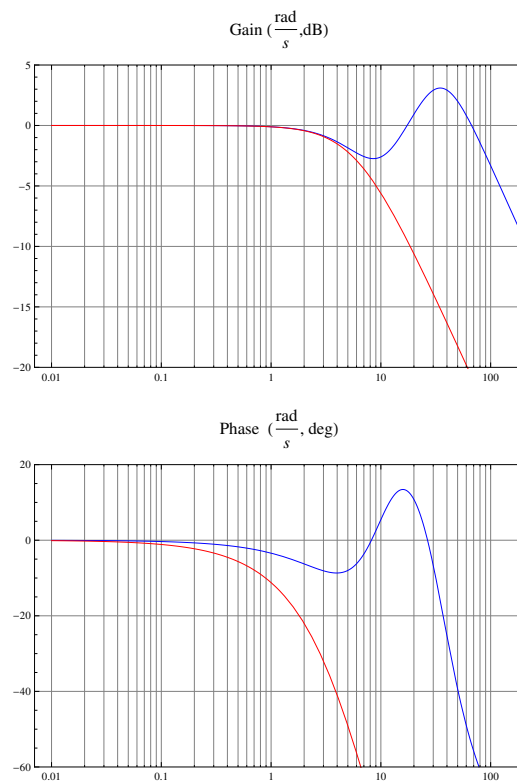


Figure 5.10: Frequency response of the different sets of effectors. Blue using weighted pseudoinverse allocator and red using differential thrusting approach.

Now, taking the Laplace transform and assuming that $M(v_p)$ can be represented by a transfer function $M = G_{\text{Actuators}}v_p$ equation 5.64 yields:

$$s^2 I \theta = G_{\text{Actuators}} v_p \quad (5.65)$$

which can be rearranged to give the open loop transfer function:

$$\frac{\theta}{v_p} = \frac{G_{\text{Actuators}}}{s^2 I} \quad (5.66)$$

Figure 5.11 shows the block diagram of the open loop pitching dynamics.

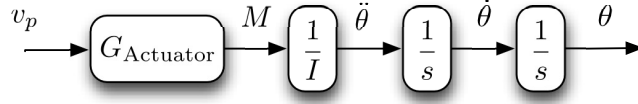


Figure 5.11: Simplified Open Loop Pitching Dynamics. Where θ is the pitch angle, v_p pitching moment command, and N the pitching moment.

Now, the only remaining part of the model is $G_{\text{Actuators}}$. The approach followed to find $G_{\text{Actuators}}$ was first, in the full 6DOF nonlinear model, a step in pitching moment demand was introduced and the resulting moments by the actuators was recorded. And, second, based on the fact that the main contribution on the effectors is given by the differential thrusting, the gyroscopic effects and the thrust vectoring a transfer function that was a linear combination of the normalised transfer functions of the motor effect, servo position and servo velocity, was defined as an approximation:

$$G_{\text{Actuators}} = a\hat{G}_{\text{Motor}} + (b + cs)\hat{G}_{\text{Servo}} \quad (5.67)$$

With the transfer function $G_{\text{Actuators}_{\text{fit}}}$ the analytical step response was calculated in terms of a , b and c . Then, a least squares problem was set up and solved by finding the coefficients a , b and c that fitted the analytical step response of $G_{\text{Actuators}_{\text{fit}}}$ to the response of the full nonlinear model. The results were $c = 0.5$ $b = 0.45$, $c = 0.05$ and the resulting transfer function:

$$G_{\text{Actuators}} = \frac{e^{-0.035s}}{2. + 0.32s} + \frac{605.59 + 70.28s}{1228.05 + s(49.18 + s)} \quad (5.68)$$

To remove the nonlinearity caused by the time delay, it was represented the by a first order padé approximant:

$$e^{-\theta s} = \frac{1 - \frac{s\theta}{2}}{1 + \frac{s\theta}{2}} \quad (5.69)$$

Injecting this approximation into 5.68 and simplifying:

$$G_{\text{Actuators}} = \frac{132.71 + 20.99s + 1.57s^2 + 0.02s^3}{133.63 + 29.36s + 1.45s^2 + 0.034s^3 + 0.0003s^4} \quad (5.70)$$

Now, to compare this approximation with the full nonlinear model in figure 5.12 its response to a step in pitching moment demand is plotted alongside that of the full nonlinear model. From figure 5.12 it is evident, then, the linear transfer function $G_{\text{Actuators}}$ matches full nonlinear model with great accuracy.

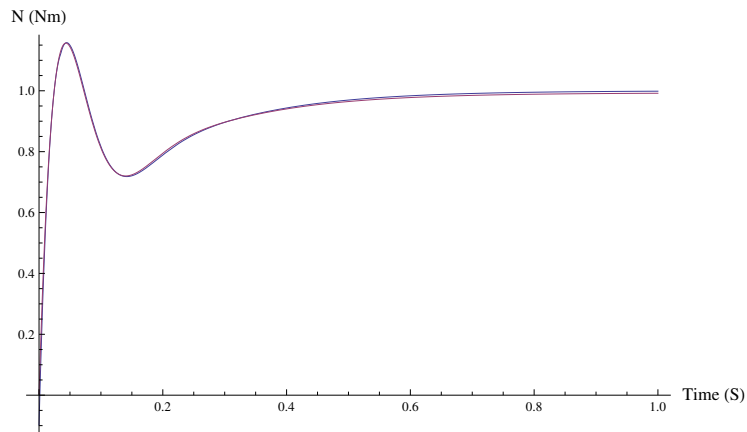


Figure 5.12: Pitching Moment Response of the Simplified Open Loop Pitching Dynamics (Red) vs the Full Nonlinear Model (Blue).

5.3.3 PD Design for Roll and Pitch

In this section the design of the Control Law for the vehicle will be detailed.

In order to stabilise the vehicle and help the pilot to control it, it was decided that a Control Augmentation System (CAS) would be the best alternative to govern all 3 angular motion, Roll, Pitch and Yaw. The pilot, or Path Planner (should it were to be implemented), will issue commands of Roll, Pitch and Roll angle. In the case of a pilot, this inputs are given through the transmitter from the ground as illustrated in figure 5.13.

The control system structure will be aimed to stabilise the vehicle and make it resilient against perturbations or changes in the plant. The major players in the stability of the plant are the Roll and Pitch motions which because of the vehicle geometry are symmetric. While the Yaw is only relevant for orientation purposes. Thus, the control system will be designed around Roll and Pitch.

Controller Structure

The IMU implemented a Extended Kalman Filter (EKF) which returned filtered values of the angles and the angular rates p q r . It has been developed in the



Figure 5.13: Mapping of the pilot reference inputs to the control system.

modelling chapter that the relation between the euler angles and the angular rates is given by:

$$\begin{bmatrix} \dot{\phi} \\ \dot{\theta} \\ \dot{\psi} \end{bmatrix} = \begin{bmatrix} 1 & \sin \phi \tan \theta & \cos \phi \tan \theta \\ 0 & \cos \phi & -\sin \phi \\ 0 & \frac{\sin \phi}{\cos \theta} & \frac{\cos \phi}{\cos \theta} \end{bmatrix} \begin{bmatrix} p \\ q \\ r \end{bmatrix} \quad (5.71)$$

Now, if a quasi hover state is assumed by constraining the vehicle within a small range of variation of the euler angles, the matrix in equation 5.73 turns:

$$\begin{bmatrix} 1 & \sin \phi \tan \theta & \cos \phi \tan \theta \\ 0 & \cos \phi & -\sin \phi \\ 0 & \frac{\sin \phi}{\cos \theta} & \frac{\cos \phi}{\cos \theta} \end{bmatrix} \approx \begin{bmatrix} 1 & 0 & 0 \\ 0 & 1 & 0 \\ 0 & 0 & 1 \end{bmatrix} \quad (5.72)$$

And so, it can safely be assumed that:

$$\begin{bmatrix} \dot{\phi} \\ \dot{\theta} \\ \dot{\psi} \end{bmatrix} \approx \begin{bmatrix} p \\ q \\ r \end{bmatrix} \quad (5.73)$$

The role of the controller is to stabilise the vehicle and help the pilot control it, thus, a controller had to be designed such that the vehicle followed the pitch angle reference θ_{Ref} sent from the stick position by the pilot.

Given that the EKF provided high quality measurements for both the pitching angle θ and the pitching rate $\dot{\theta}$, it was decided that to obtain an stabilising controller the most pragmatic way was to design a PD controller. To exploit the quality of the $\dot{\theta}$ measurement and to avoid the so-called “derivative kick” the feedback of the derivative of the output $\dot{\theta}$ was selected rather than trying to construct an estimate derivative of the error. The structure of this controller

is shown in figure 5.14. Hence, the task of designing the controller is finding the gains K_D and K_P .

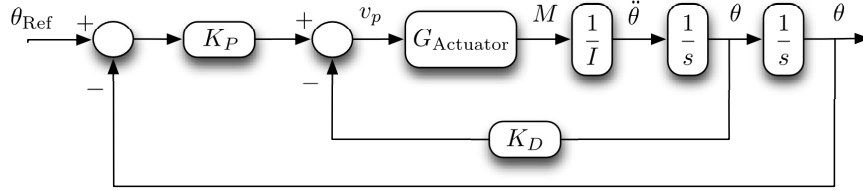


Figure 5.14: Structure of the PD controller for the pitching dynamics.

Gain Tuning

In the simulation model several successful combinations of gains were found by trial and error, which resulted in a stabilising controller. However, this methodology neither gave any guarantee to provide stability and robustness of the controller, nor it provided evidence that the vehicle was exploiting all the performance capabilities of the vehicle. Hence, it was concluded that a more informative and systematic approach should be carried out. The approach chosen was a mix between closed-loop shaping in the frequency domain and testing in the ball-joint rig.

The approach followed to tune the controller was a mixture of model based tuning and testing with the real vehicle on the rig. Essentially, the procedure was to find gains that gave desirable characteristics on the frequency domain and, then, testing them in the vehicle to see its performance. Thus, by visualising the bode plots, an informative quantification of the quality parameters and a clear picture of the trends that the gains introduced was obtained. Thus, minimising the amount of experiments by reducing the amounts of candidate gains. And, by testing the gains of the vehicle, it was ensured that no undesirable coupling arose, the real measurements sensor were put to test and the full dynamics were taken into consideration.

To carry out this approach, the first step is to define the sensitivity transfer function, S , and the complementary sensitivity function, T and the open loop transfer function, L . From the diagram in 5.14 this functions are given by:

$$T = \frac{G_{\text{Actuators}} K_P}{I s^2 + G_{\text{Actuators}} (K_P + K_D s)} \quad S = \frac{s(G_{\text{Actuators}} K_D + I s)}{G_{\text{Actuators}} K_P + G_{\text{Actuators}} K_D s + I s^2} \quad (5.74)$$

$$L = -\frac{G_{\text{Actuators}} K_P}{G_{\text{Actuators}} K_D s + I s^2}$$

Several authors [31] suggest that the quality a control system can be expressed by the peaks of the sensitivity and the complementary sensitivity functions. This peaks are defined as:

$$M_S = \max_{\omega}(|S(j\omega)|) \quad M_T = \max_{\omega}(|T(j\omega)|) \quad (5.75)$$

Skogestad,[31], suggest that the M_S should be less than 2 (6dB) and M_T should be less than 1.25 (2dB) to guarantee a good quality of response and stability robustness. That is, enforcing those limits guarantees acceptable gain and phase margins. As an indicator of performance he suggests to use the close loop bandwidth ω_B and the gain at low frequencies of the S function. ω_B is defined as the frequency at which S crosses -3dB from below, thus, higher the ω_B the faster the system will be. Regarding S, the smaller the gain of S at low frequencies the better the disturbance rejection.

Summing up the requirements, the design of the controller will aim to find a high ω_B while guaranteeing stability by maintaining M_T and M_S below the specified boundaries and ensuring good disturbance rejection by making small the gains at low frequencies.

To easily manipulate the gains and see the immediate results, a graphical interface was constructed in Mathematica with two sliders, one for the K_P and one for the K_D . A screenshot is shown in figure 5.15. With this facility it was very easy to test and play with the gains, thus, resulting in a deeper understanding of the effects and trends. While, at the same time, it provided a quantified measure of the quality of the response in terms of the Peaks M_T and M_S . And, more importantly, it raised awareness on the effects of possible changes in the gains showing the trends that each gain introduced on the response. This was fundamental because in provided a much deeper insight on the suitability of each combination of gains than what could have been achieved by a conventional trial and error tuning on the rig.

To test the controller on the vehicle, it was attached to a ball joint in a way that it constrained only the position, thus, allowing the 3 angular motions, Roll, Pitch and Yaw to be free and constraining only the translational motion. The setup is illustrated in figure A.12. Whereby, it provided an accurate picture of the effect of the different gain combinations on the vehicle. The most relevant inconvenience of this setup was that there was an offset between the ball and the vehicle's centre of gravity. This exerted an inverted-pendulum-like destabilising moment to the vehicle. Hence, it made vehicle more unstable than when flying. In the end, due to the robustness of the controllers enforced by the peaks M_T and M_S , the controllers were able to cope with it.

The procedure to test the controller was to upload the gains to the microcontroller for both Roll and Pitch and steadily increase the throttle until the nominal operating point. Then, simulating perturbations, the vehicle was pushed out from equilibrium to see if the gains were able to bring it back to position. To test the reference following, several inputs from the transmitter stick were sent and the response was recorded via telemetry. To the prevent the vehicle from yawing, a similar PD controller was hand-tuned on the simulation model until it gave a satisfactory performance and, later, it was retuned on the rig and remained unchanged during the trials of the Roll and Pitch controllers. A sequence of a typical test is shown in figure 5.16.

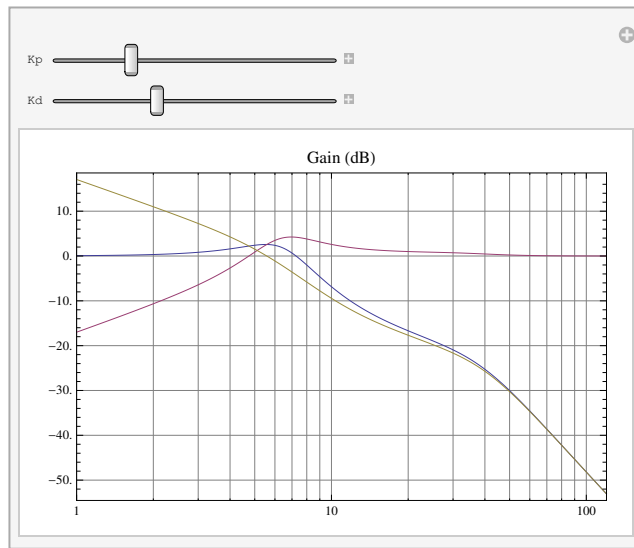


Figure 5.15: GUI to modify the gains and display the closed loop frequency responses. T is presented in Blue, S in Red and T in Yellow.

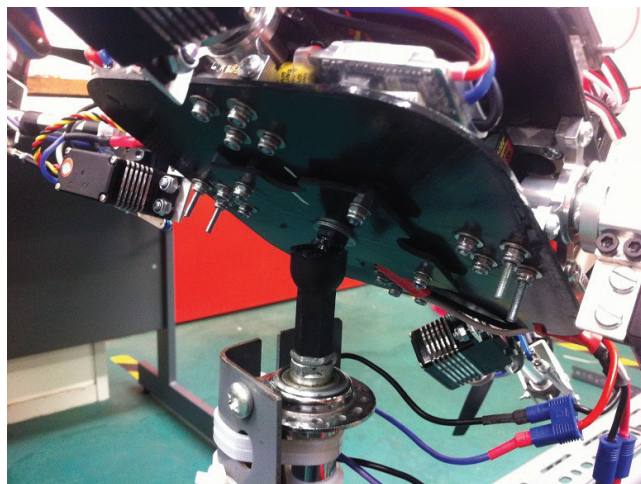


Figure 5.16: Detail of the ball joint rig. The ball joint is attached to a frame by a bicycle hub that allows the ball joint to spin, yaw, freely. On its side, the ball joint allows for free movement of the pitch and roll axes. Hence, the only motion constrained is the translational.

With the setup described, both the test rig and the bode plot interface, the tuning procedure was carried out as follows. With the GUI by moving the sliders different combinations of gains were found that comply with the afore-

mentioned criteria. Once a candidate combination was found it was tested on the real vehicle attached to the ball joint rig to see its performance. By following this approach, a deeper understanding of the tuning process was gained, because, apart from seeing the response on the real vehicle on the rig, it was also possible to quantify M_T , M_D , ω_B and S , to monitor the trends and to understand better the trade-off implications.

Finally, by this methodology, the gains obtained were:

$$K_P = 2.5 \quad K_D = 0.38 \quad (5.76)$$

The frequency response of T, S and L is shown in figure 5.17. The characteristic parameters of this response are:

$$M_T = 1.90\text{dB} \quad M_S = 3.79\text{dB} \quad \omega_c = 3.83 \frac{\text{rad}}{\text{s}} \quad \frac{dS}{d\omega_{\text{Low Freq}}} = -20 \frac{\text{dB}}{\text{dec}} \quad (5.77)$$

and the stability margins are:

$$GM = 23.6\text{dB} \quad PM = 78.62^\circ \quad (5.78)$$

The poles of the system are:

p_1	$-2.21 + 6.03j$
p_2	$-2.21 - 6.03j$
p_3	-6.35
p_4	$-21.94 + 32.68j$
p_5	$-21.94 - 32.68j$
p_6	-57.76

and the zeros are:

z_1	$-7.47 + 7.05j$
z_2	$-7.47 - 7.05j$
z_3	-60.57

Baseline, Conventionally Actuated Quadrotor

To put these figures into perspective, it is necessary to compare them against a baseline. The aim of this project is to develop an innovative actuated vehicle, hence, the logical step is to compare it with a conventionally actuated quadrotor. Thus, a model of the pitching dynamics of the same quadrotor dynamics was developed, but, this time the function $G_{\text{Actuators}}$ was equivalent to a differential thrust dynamics, i.e., G_{Motor} . In order to make the systems comparable, the controller of this conventional quadrotor was tuned so that its dominant poles laid at the same position than those of the gyroscopically actuated vehicle.

The gains that were found to give the same dominant poles are:

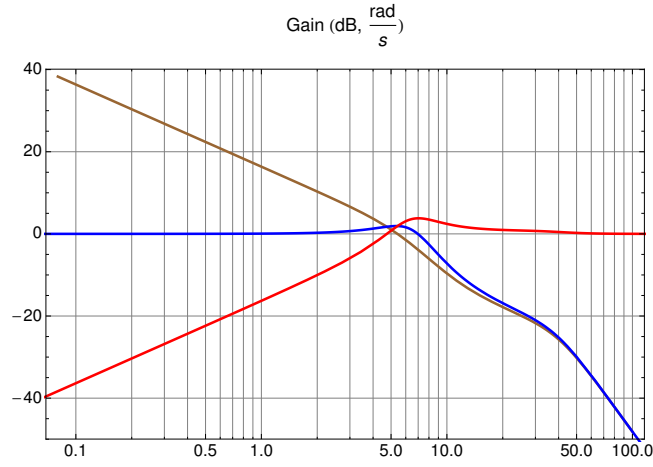


Figure 5.17: Closed loop functions frequency response, with the final gains $K_P = 2.5$ and $K_D = 0.38$. Blue is T, Red is S and Brown is L.

$$K_{P_{\text{motors}}} = 6.58 \quad K_{D_{\text{motors}}} = 1.61 \quad (5.79)$$

The closed loop frequency responses of the functions T_{motor} , S_{motor} , L_{motor} , for the conventional quadrotor are:

$$M_{T_{\text{motors}}} = 2.07\text{dB} \quad M_{S_{\text{motor}}} = 5.76\text{dB} \quad \omega_{c_{\text{motor}}} = 2.68 \frac{\text{rad}}{\text{s}} \quad \frac{dS}{d\omega_{\text{Low Freq}_{\text{motor}}}} = -20 \frac{\text{dB}}{\text{dec}} \quad (5.80)$$

And the stability margins are:

$$GM_{\text{motors}} = 4.71\text{dB} \quad PM_{\text{motors}} = 34.45 \quad (5.81)$$

The poles of the baseline system are:

p_1	$-2.22 + 6.02j$
p_2	$-2.22 - 6.02j$
p_3	-6.17
p_4	-7.69
p_5	$-20.81 + 53.76j$
p_6	$-20.81 - 53.76j$
p_7	-57.07
p_8	-58.68

and the zeros:

z_1	57.07
z_2	-6.17
z_3	$-24.59 + 24.97j$
z_4	$-24.59 - 24.97j$
z_4	-57.07

With the baseline system designed it's time to compare the new vehicle's performance against it.

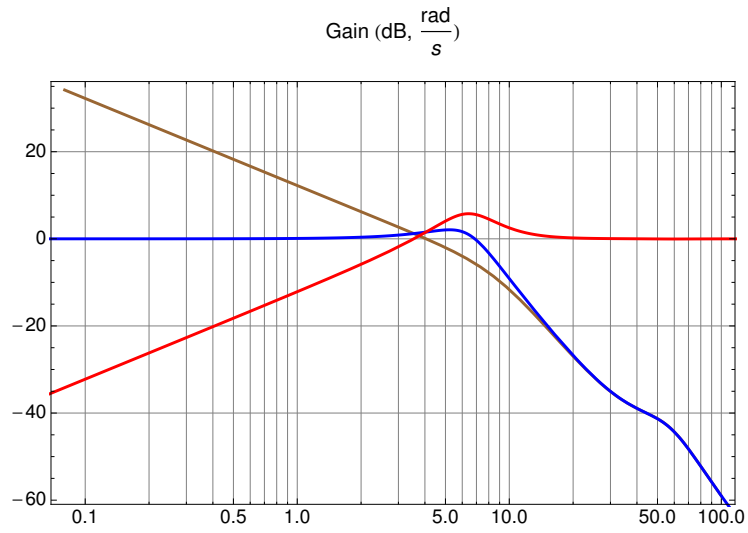


Figure 5.18: Closed loop functions frequency response for the baseline controller, aka, differential thrust. Blue is T, Red is S and Brown is L.

Performance Comparison

To see at a glance the difference between both systems in figure 5.18 the closed loop response frequency response of the new quadrotor are presented alongside those of the conventional quadrotor. Also, in figure 5.19 the gain and the phase of the two systems is presented to provide more insight into the comparison.

In the following the two systems will be compared in terms of each of the performance measures.

Let's start with the closed loop function peaks:

$$M_T = 1.90\text{dB} \quad M_S = 3.79\text{dB} \quad M_{T_{\text{motors}}} = 2.07\text{dB} \quad M_{S_{\text{motor}}} = 5.76\text{dec} \quad (5.82)$$

The target for these peaks was $M_T < 2\text{dB}$ and $M_S < 6\text{dB}$. Both peaks are lower with the new actuator suite than in the conventionally actuated quadrotor. This means that the stability and robustness of the new system has higher safeguards than with the conventional quadrotor. In which the limits imposed are only met in the case of M_S and they're violated in the case of M_T . This is better seen in the Stability Margins:

$$GM = 23.6\text{dB} \quad PM = 78.62^\circ \quad GM_{\text{motors}} = 4.71\text{dB} \quad PM_{\text{motors}} = 34.45 \quad (5.83)$$

The conventional quadrotor, has a very narrow gain margin, consequence of the violation of M_T . And, the phase margin is almost half that of the new design. Thus, it can be concluded that an overall better quality of the response of the new strategy's actuated quadrotor and a higher confidence level about its stability has been achieved.

To compare the response in terms of performance, the parameters to be evaluated is the bandwidth and the phase lag. The bandwidth for both systems are:

$$\omega_c = 3.83 \frac{\text{rad}}{\text{s}} \quad \omega_{c_{\text{motor}}} = 2.68 \frac{\text{rad}}{\text{s}} \quad (5.84)$$

The speed of the new vehicle is higher with the new strategy, but, more importantly, from figure 5.19 it can be seen that the phase lag is much lower also in the new platform yielding then, a faster response.

This is mostly because the non-minimum phase effect that arises in the conventional quadrotor due to the right-hand plane zero present in this system. This is very clear from the frequency response of the two actuator suits in figure 5.10. The direct cause of the rhz is the presence of time delay in the motor response. Thus, it can be stated that the new vehicle has better performance than a conventional one. This is mostly because the problem of the time delay has been overcome by the use of the new actuator suite.

Summing up, evidence has been provided of both the improvement of the new strategy's ability to provide stability and robustness, via M_T and M_S , and

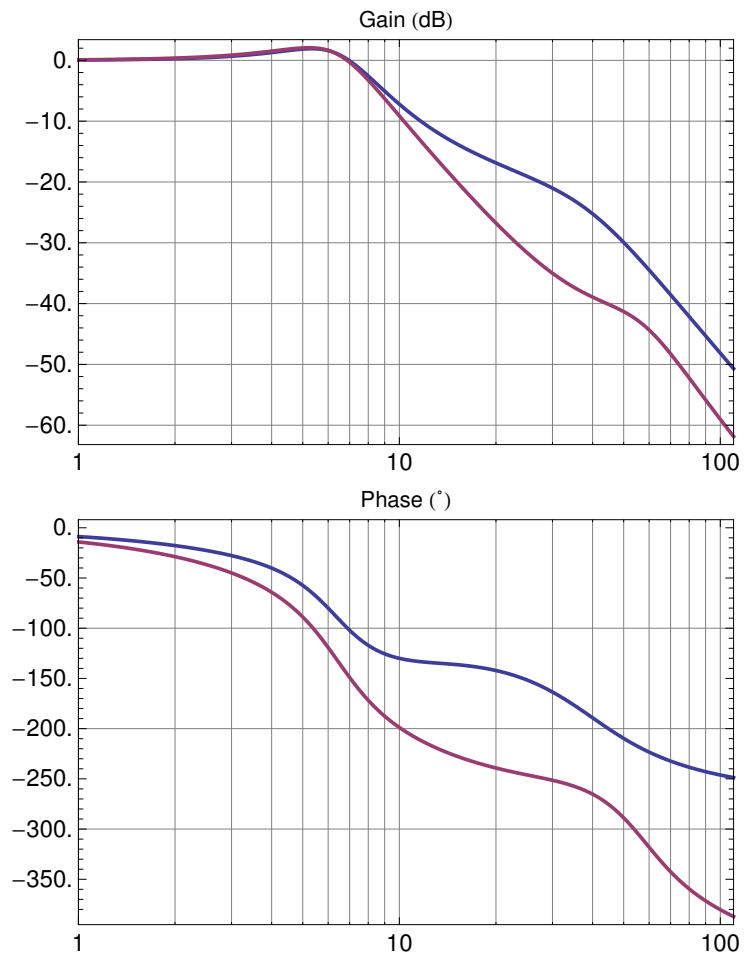
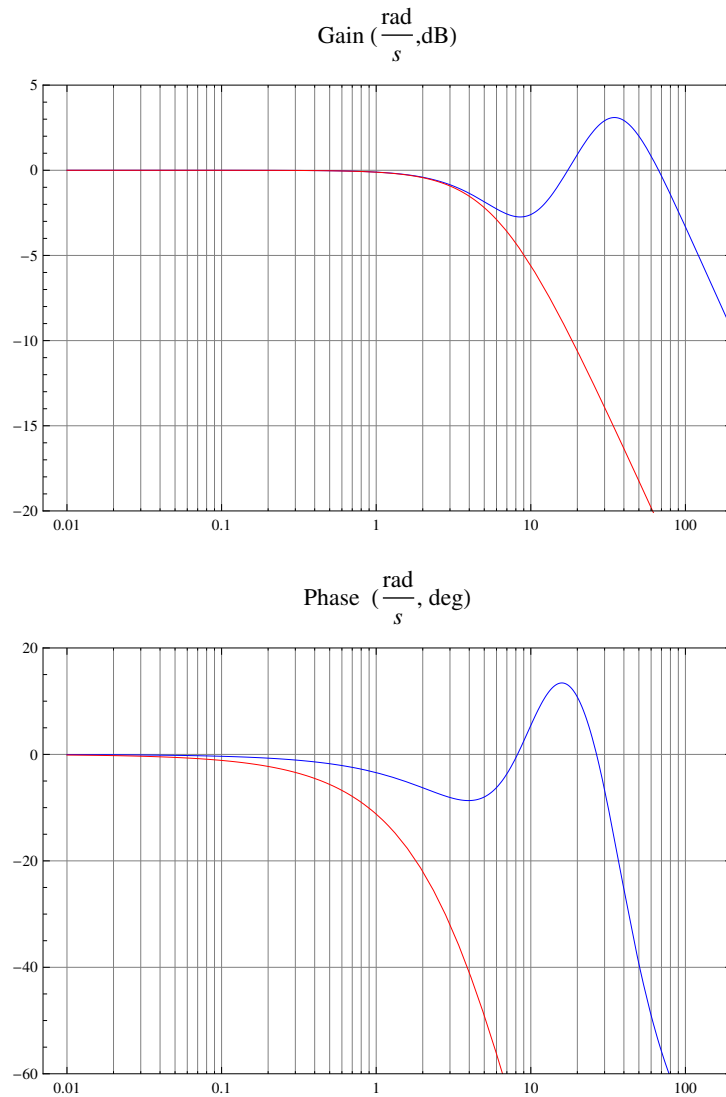


Figure 5.19: Gain and Phase of the Closed loop function T, for both actuators suites, The gyrosopic+motors (Blue) and the conventional quadrotor (Red).

of its ability to provide higher performance, via the phase lag and the bandwidth. However, the advantage in performance, speed essentially, is not, by any objective measures, radical or groundbreaking and so an inevitable question arises: with all the price paid in terms of complexity and added weight, is there any way of improving the performance further? The answer is yes, and will be analysed in the next subsection.

How to Improve

To start the discussion on which is the way to improve the vehicle's performance dramatically a clear picture of the performance of the two actuators suites must be kept in mind. To facilitate this, figure 5.10 is reproduced here, in red is the conventional, differential thrust, actuation strategy while in blue, is the proposed strategy of gyroscopic effects combined with motors:



The first thing that can be inferred is that the major improvement is in the frequency at which the system rolls off. The new design induces a much larger bandwidth since the system rolls off about 100 rad/s while in the conventional actuation about 10 rad/s. In the controller design this major feature has not been used. The only feature that has benefitted the new design, has been the smaller phase lag at low frequencies, but the overall bandwidth has not seen

a major improvement. To see why more clear, in figure 5.20 the T transfer function of the controller designed is shown alongside the frequency response of the actuators.

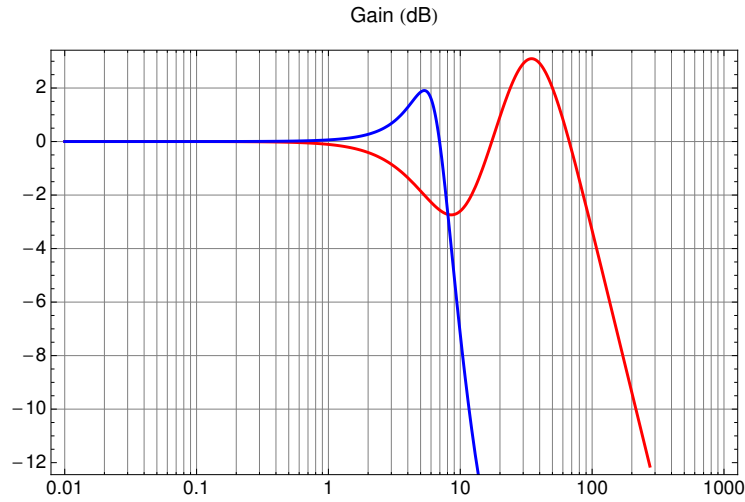


Figure 5.20: Gain of frequency response of the T function (Blue) and of the Gyroscopic+Motor actuation suite (Red).

It is clear, that the controller rolls off much earlier than the actuators do, hence, it is not exploiting all the potential that this strategy could yield. Then, the question of why have this gains been elected. The reason is, because it would lead to very large servo deflections that would saturate very fast. But now, lets consider the features of such a design and, later, solutions will be provided to mitigate the saturation problem.

Scaling up the order of magnitudes of the gains and searching for a acceptable solution in terms of M_T and M_S criteria. A controller that exploited the full features of the actuators was found. With the gains:

$$K_{P_{\text{HighGain}}} = 32.3 \quad K_{D_{\text{HighGain}}} = 1.19 \quad (5.85)$$

The closed loop frequency responses of the functions T_{HighGain} , S_{HighGain} , L_{HighGain} , for the high gain controller, the indicators are:

$$M_{T_{\text{HighGain}}} = 0.95\text{dB} \quad M_{S_{\text{HighGain}}} = 5.96\text{dB} \quad \omega_{c_{\text{HighGain}}} = 13.42 \frac{\text{rad}}{\text{s}} \quad (5.86)$$

The outcome is very promising, the system is much more faster, almost one order of magnitude, while the quality of response indicators have been kept below the specified limits. This is more clear when the phase and gain of the 3 systems is compared, see figure 5.21.

This, is the kind of performance improvements that this actuation concept can bring, however, with the current actuators, it's not possible because they

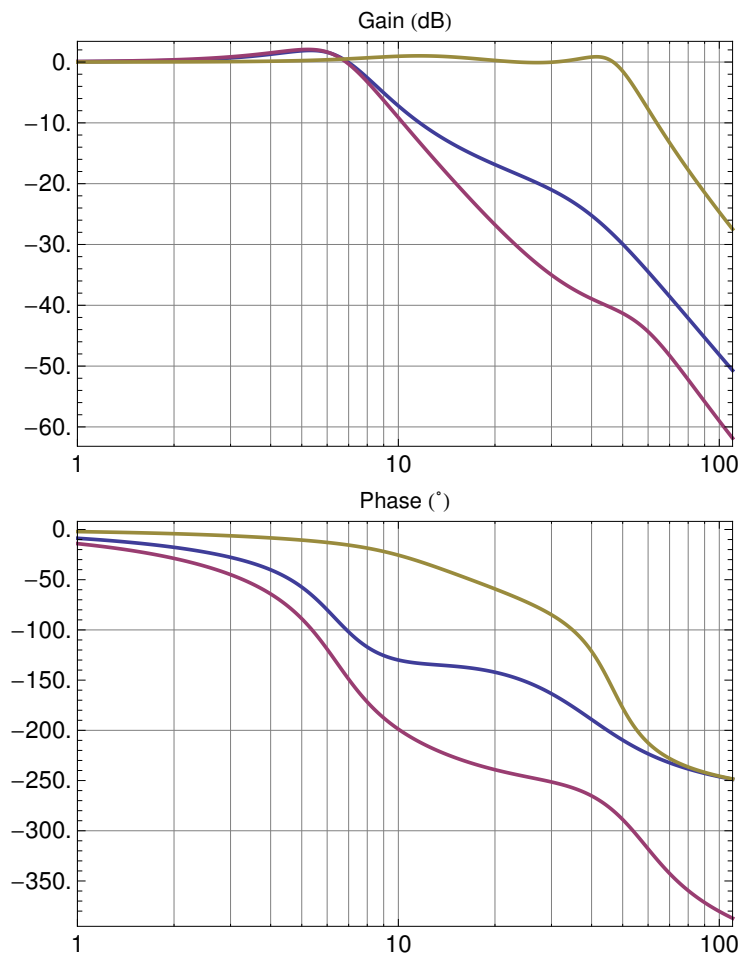


Figure 5.21: Closed loop functions frequency response for the high gain controller. Blue is T, Red is S and Brown is L.

would saturate. For example, K_D is 35, thus, if the error in pitch is 0.1 rad the pitching moment demand would be 3.5Nm, which would require servo deflections of up to about 2.4 rad, and the the servo limit is 0.3 rad. On the other hand motors would be asked to deliver within its boundaries. Then, the solution to the problem is reduced to making the servos deliver the same action with less deflection.

The actions that the servo delivers are proportional to $\dot{\eta}J\Omega_0$, so the increment of any of this 3 parameters would lead to an increase on the servo action. An increase on $\dot{\eta}$ however, would lead to higher deflections, thus, it can not be modified. Hence, the solution to the problem is either to increment on either J or Ω . Therefore, the whole propeller rotor would have to be redesigned.

There are several aspects that can should be taken into account to redesign a propeller that would lead to higher J or Ω_0 . The first step would be to increment the diameter and reduce greatly the pitch, thus Ω_0 would raise and the thrust would be kept constant, and, as the diameter has increased, so has J since $J \propto R^2$. Another step to increase J would be to increase the density of the material. This could be accomplished by designing the propeller for example in aluminium. In this line, also, to increment the inertia J small insertions of a high density metal such as lead or tungsten in the tips of the propeller, could lead to promising results.

All this increments in terms of $J\Omega_0$ would lead to a more stringent requirements in terms of mechanical strength of the actuators such as the motors and the servos. Hence, a careful analysis on the loads of each of the components should be carried out. And, if required, some elements should be either changed or redesigned.

Chapter 6

Testing and Results

6.1 Introduction

In this section the different test carried out with the vehicle are summarised. First, a comparison of the responses of the simulation model against the real vehicle in the ball joint is undertaken. Second, a sample test for the tuning procedure in the ball joint is illustrated. And, third and finally, the first flight is documented.

6.2 Validation of the Simulation Model

In order to be able to confidently fly the vehicle, the simulation model had to be validated. To do this, it was thought that the safest approach was to validate the simulation model to make sure that the controllers that were being designed had accurate foundations before the actual vehicle flew.

To assess the validity of the simulation model several impulse inputs were fed into the real vehicle and recorded, after, the same inputs were fed to the simulation model and both responses are compared.

When the vehicle is mounted on the ball joint, its dynamics are different from the vehicle in flight. This is because, the joint is not located at the centre of gravity, but located in the same X and Y but with an offset in Z downwards.

To model the effect of the joint, the forces and moments that it creates onto the vehicle have to be analysed. Basically, the force that the joint exerts onto the vehicle is the reaction to the resultant of the forces that are applied onto the airframe, namely thrust and weight. And the moment that the joint creates is the resultant of the transport of the aforementioned reaction force to the CG, i.e. $\mathbf{M}_{\text{Joint}} = \mathbf{r}_{\text{CG2Joint}} \times \mathbf{F}_{\text{Resultant}}$. Hence, to include the dynamics of the ball joint the following action have to be included into the simulation model:

$$\mathbf{F}_{\text{Joint}} = -\mathbf{F}_{\text{Resultant}} = -\Sigma\mathbf{F} \quad \mathbf{M}_{\text{Joint}} = \mathbf{r}_{\text{CG2Joint}} \times \mathbf{F}_{\text{Joint}} \quad (6.1)$$

With this modifications, the simulation model is, then, fully comparable

with the experimental results from the ball joint test rig. In the following the results of the simulation are to be compared with the ball joint test rig for the different axes, Roll, Pitch and Yaw, to assess the accuracy of the modelling.

To get a good picture of the dynamics of the system, specially, of the high frequency components which contain the most uncertainty, it was thought that the best benchmark signal would be an impulse. Thus, with the transmitter stick an impulse was created and both the response of the real vehicle and the input were recorded. Then, the recorded command was fed into the simulation model and the response are compared for all three axes.

Pitch

In figure 6.1 the response to an impulse from the transmitter is represented for both the simulation and the vehicle in the ball joint. It can be seen that although the signal quantisation does not allow for much resolution, the trend in the amplitudes of the peaks and the frequency are very similar to each other. The existence of overshoot and the underdamping tendency is due inverted pendulum like de-stabilising action of the ball joint rig to real vehicle. According to the simulation, in flight the vehicle does not experience this kind of underdamped dynamics.

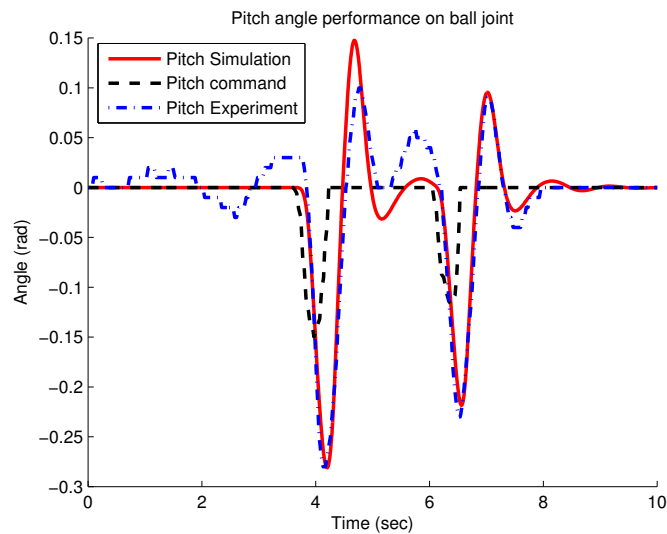


Figure 6.1: Pitch Validation

Roll

Similarly to the Pitch, the Roll comparison in figure 6.2 shows a very similar frequency. Regarding the damping, the ratios of the amplitudes appear to be very close one to another, but, the quantisation of the experimental signal, again, does not allow for a precise conclusion. Similarly with the pitch, the existence of overshoot and the underdamping tendency is due to the de-stabilising effect introduced by the rig moments. According to the simulation, in flight the vehicle does not experience this kind of underdamped dynamics.

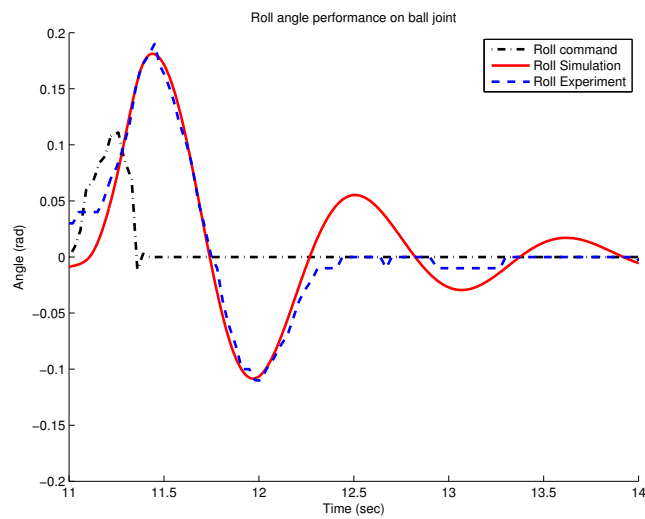


Figure 6.2: Roll Validation

Yaw

To assess the performance in the yaw axis of the simulation model, a train of pulses were sent to the vehicle and the response was recorded and the same pulses were fed into the simulation model. The result is plot in figure 6.3. It can, then, be seen that the model represents with high fidelity the behaviour of the real vehicle since the amplitudes of the peaks are almost the same, indicating similar damping, and the time between peaks is also very similar, thus, indicating the similar frequency.

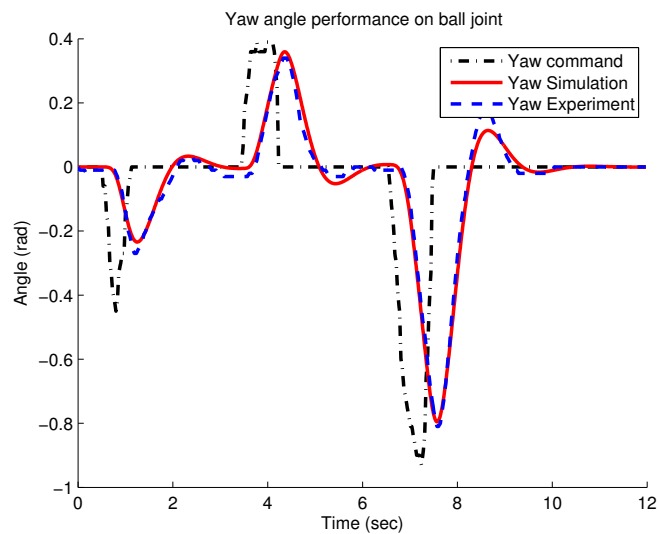


Figure 6.3: Yaw Validation

Validation Conclusions.

Evidence has been presented that the overall the simulation model qualitatively follows the trends of the real vehicle with fidelity. This is only a first step in the validation of the model and a more extensive quantitative validation based on flight test data should be carried out in the future.

6.3 Stability at ball joint rig

This section presents a typical test on the ball joint rig that that was carried out for the tuning of the controller. The sequence followed is described below.

1. Holding the vehicle a slow ramp of the throttle is send and when the nominal rpm have been obtained the vehicle is released to check for **stability**. This is shown in figure 6.4.
2. A series of perturbation were introduced to check the controller for **disturbance rejection**. This was done by pushing the vehicle in each of axis with a foam handle. For each axis see figure 6.5 for Roll, figure 6.6 for Pitch and figure 6.7 for Yaw. See figure 6.9 for a sample recovery sequence.
3. Finally, the controller was tested for **reference tracking**. The time histories for a sample test are presented for each axis see, figure 6.8 for Roll , figure 6.10 Pitch and figure 6.11 for Yaw.

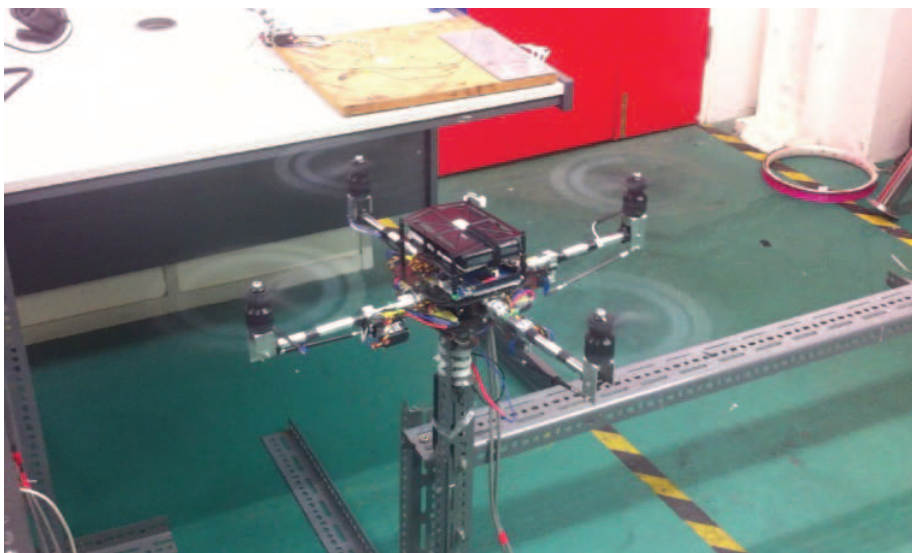


Figure 6.4: Stability at ball joint rig



Figure 6.5: Perturbations in Roll at ball joint rig

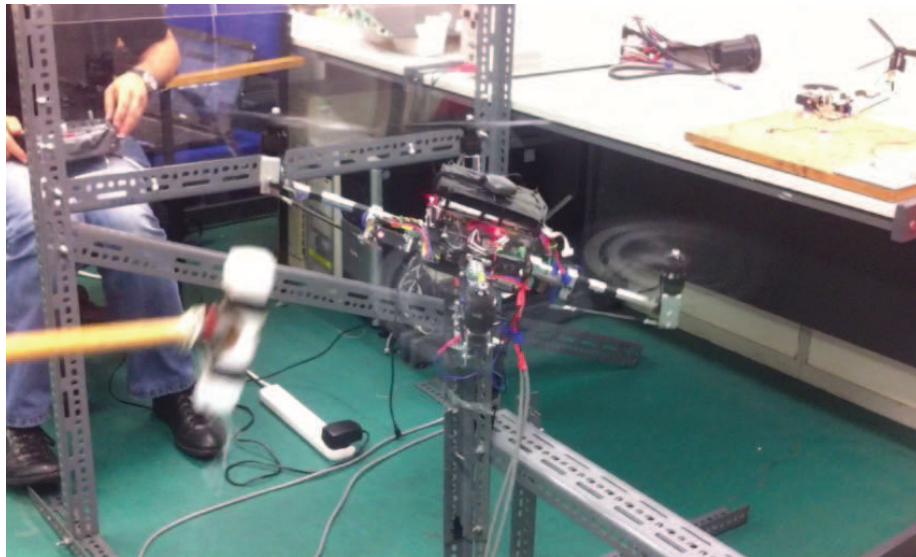


Figure 6.6: Perturbations in Pitch at ball joint rig

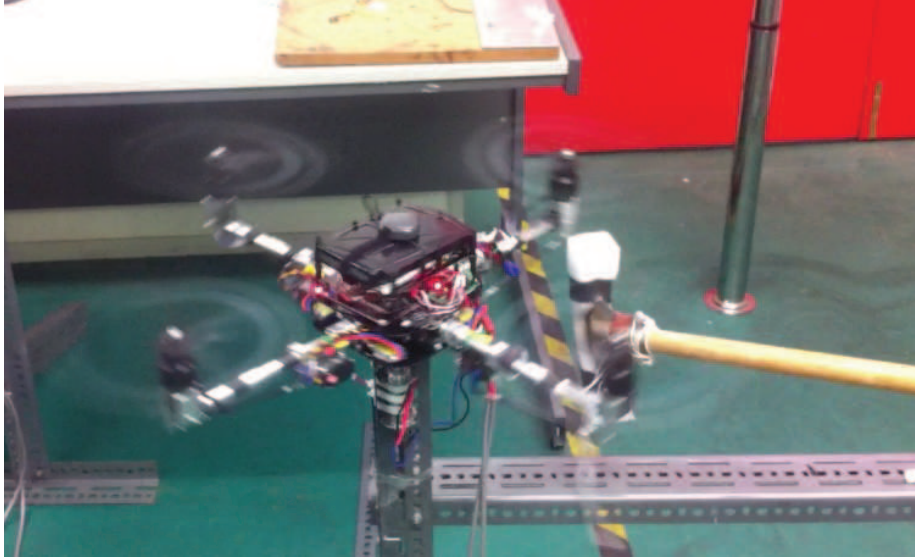


Figure 6.7: Perturbations in Yaw at ball joint rig

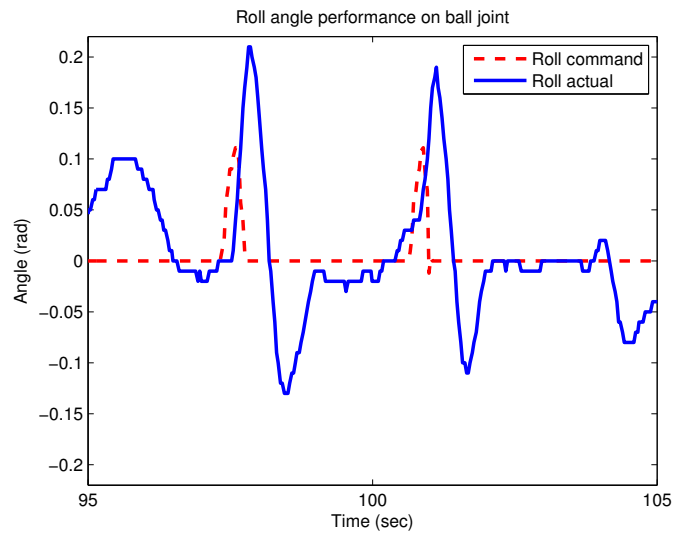


Figure 6.8: Roll angle command tracking at ball joint rig

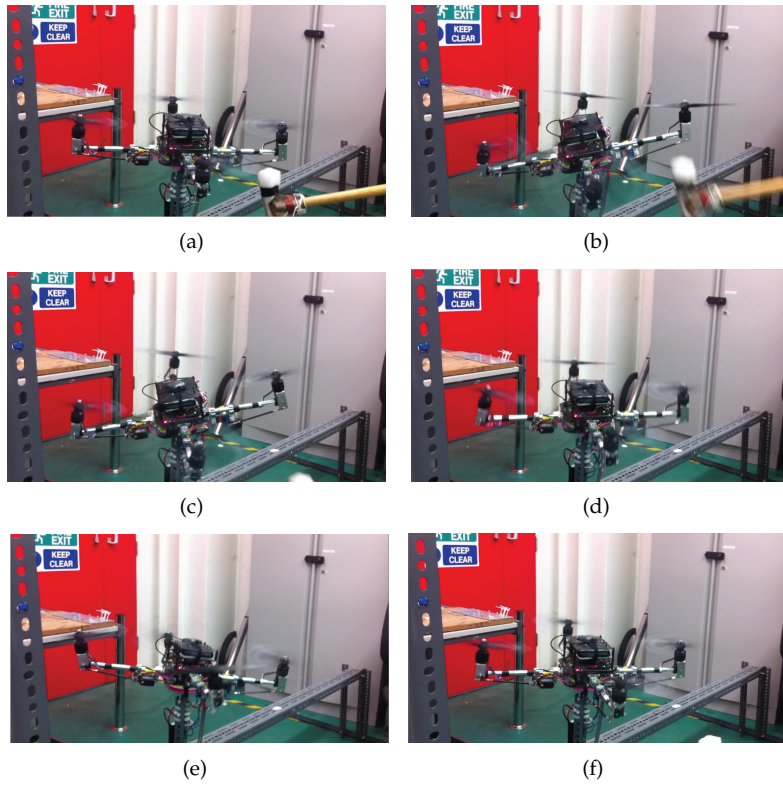


Figure 6.9: Vehicle recovery after a disturbance test.

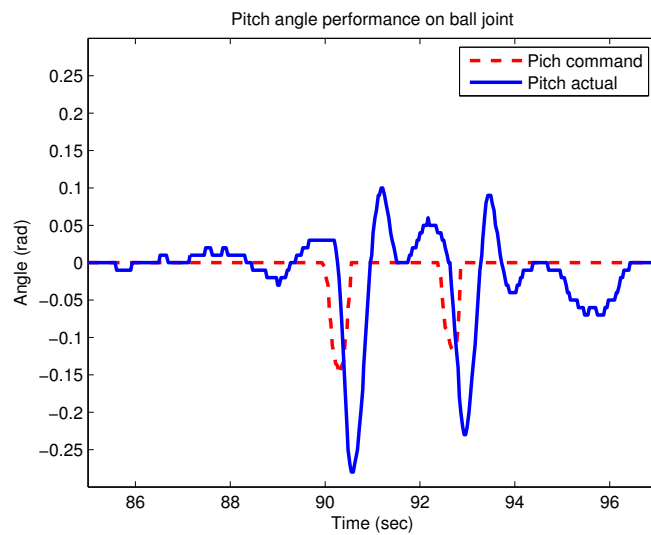


Figure 6.10: Pitch angle command tracking at ball joint rig

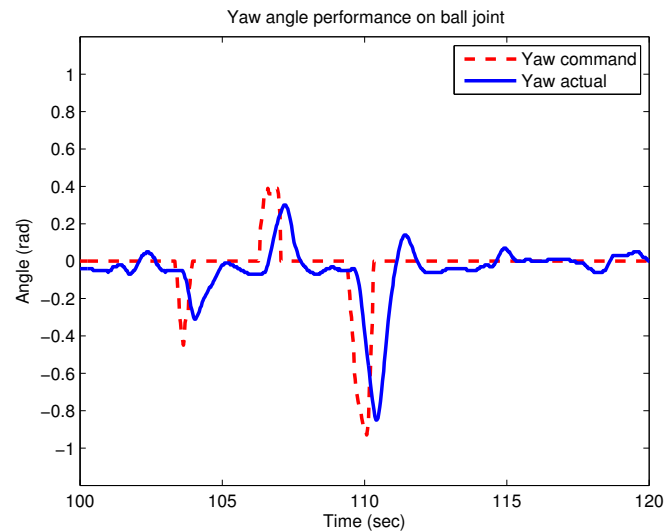


Figure 6.11: Yaw angle command tracking at ball joint rig

6.4 Flight test

Finally, once the control was tuned and satisfactory performance was achieved, the first flight was attempted. The vehicle took-off, see figure 6.16, hovered, see figures 6.19 and 6.18, and moved around for about a minute and then landed, see figure 6.17. Relevant flight variables of interest were recorded and are shown in this section.

The data recorded is shown in a series of figures, the data has been organised by axes according to each control loop. For each axis, the variables shown are, the Angle Commanded, the Actual Angle, the angular rate and the total moment resulting from the control law. To evaluate the performance of the controller. The throttle history was also monitored, ranging from -50% to 50%, -50 meaning, zero stick and 50% meaning full throttle. The plots are organised as follows:

- The **Throttle** history is illustrated in figure 6.12.
- The **Roll** axis is illustrated in figure 6.14.
- The **Pitch** axis is illustrated in figure 6.13.
- The **Yaw** axis is illustrated in figure 6.15.

The first flight was the last stage of the project, hence, it was intended just as a field-test to all the theory developed in this thesis. Further flight testing should imply quantitative comparisons based on systematic testing to analyse relevant variables in order to further validate the simulation model and to improve the control system.

Conclusions

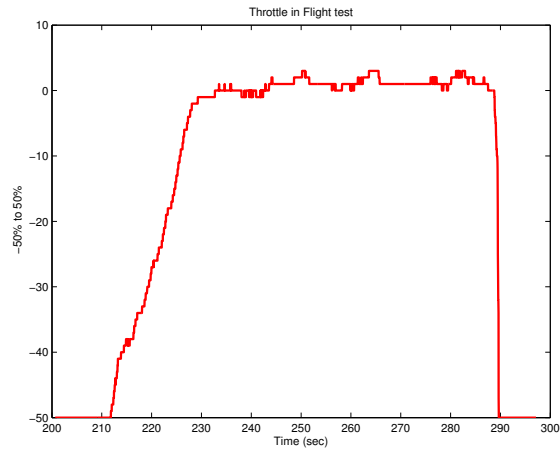


Figure 6.12: Throttle during flight test. Note that the throttle varies from -50%, zero stick, to 50%, full stick. Hence, around zero, the vehicle is at hover using around half of the power, with the stick in the middle.

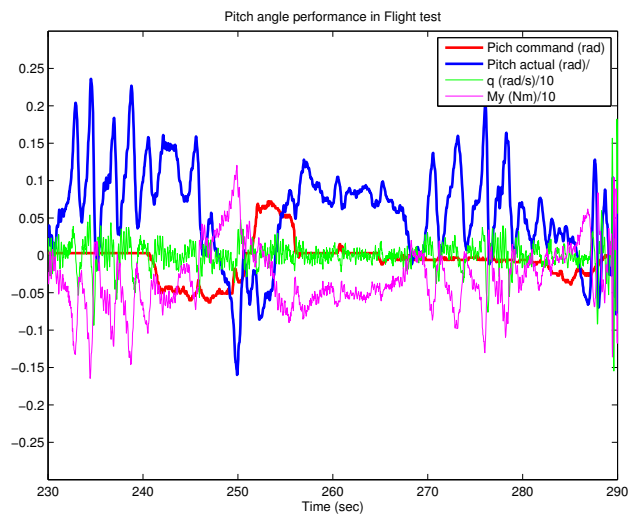


Figure 6.13: Pitch angle during the first flight. Note the scaling of the moment and angular rate.

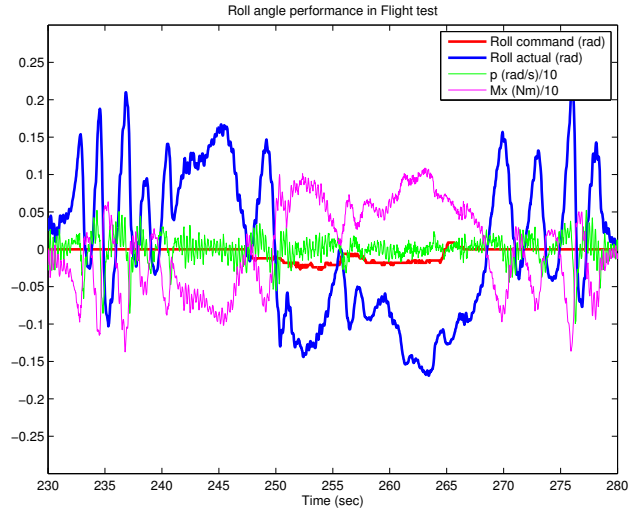


Figure 6.14: Roll angle during the first flight. Note the scaling of the moment and angular rate.

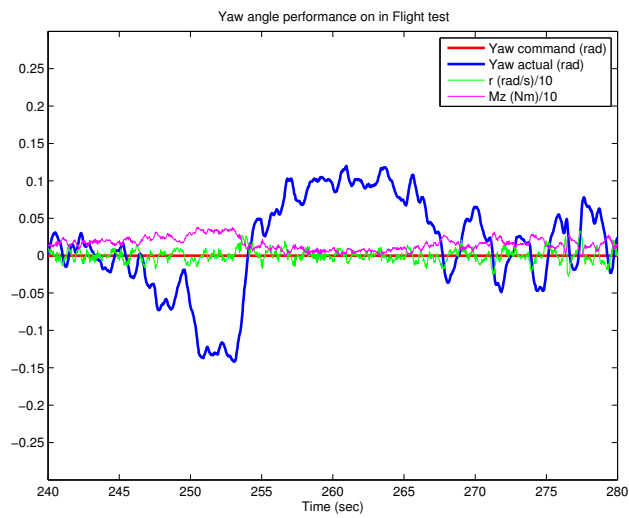


Figure 6.15: Yaw angle during the first flight. Note the scaling of the moment and angular rate.

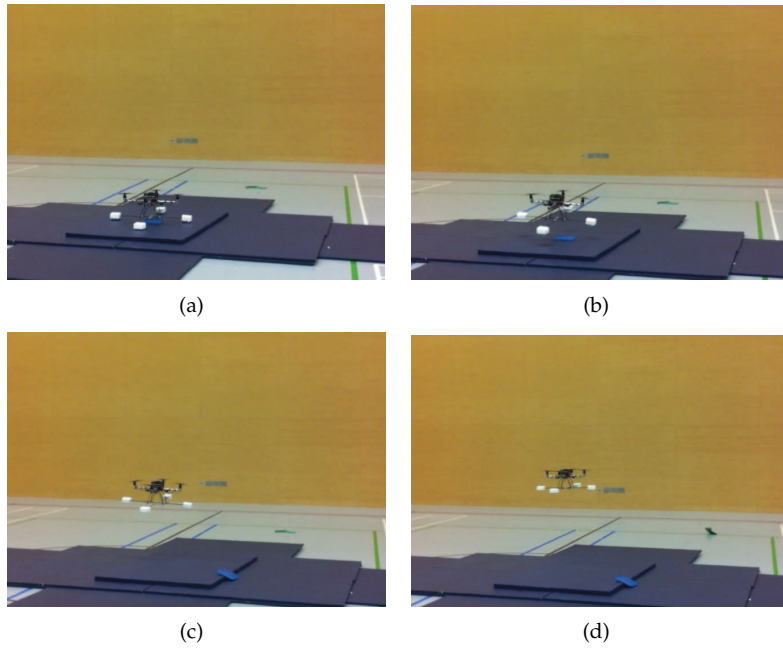
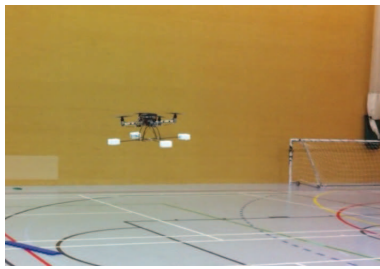
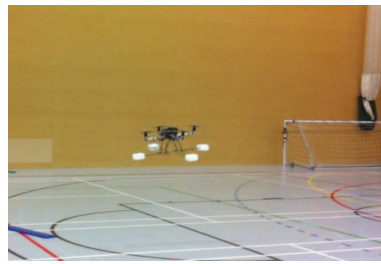


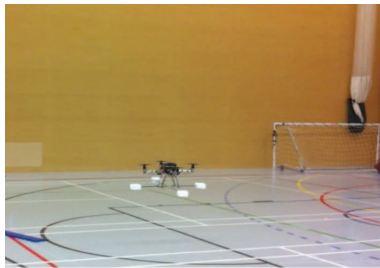
Figure 6.16: First Flight: takeoff



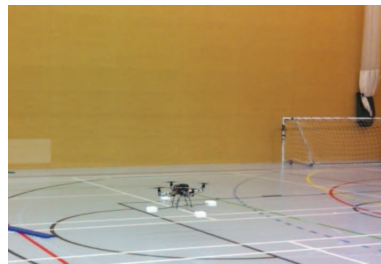
(a)



(b)



(c)



(d)



(e)

Figure 6.17: First Flight: landing



Figure 6.18: First Flight, Vehicle at hover.



Figure 6.19: First Flight, Vehicle at hover.

Chapter 7

Conclusions of the Work

7.1 Conclusions of the Work

- **Actuator Modelling.** A mathematical model has been developed and presented for the novel actuator suite. This model encapsulates the gyroscopic effects, the aerodynamic forces and moments as well as the motor and servomotor dynamics. A thorough identification of dynamics of the individual actuators, motors and servomotors has been carried out in the frequency domain. Aerodynamic measurements to characterise the propellers in static regime have also been performed. And, the production of gyroscopic forces and moments has been fully developed as well. Finally, the vehicle ability to carry load without diminution in efficiency of the propulsion system has been shown.
- **Flight tested control system.** A successful control system has been developed and successfully demonstrated on flight with the real vehicle. The control developed is based on a Pseudoinverse Control Allocator and a simple PD control law. Evidence has been presented about the capability of the control system to yield promising results in terms of performance, stability and robustness while it has shown to be efficient enough to be implemented in a simple microcontroller.
- **Improvement against a Conventional Quadrotor.** Comparing to a conventional actuation strategy in a quadrotor, i.e., based on varying propeller rpm, evidence has been presented of the potential of the new actuation strategy to increase the speed and performance of the actuator suite. The actuators, have shown significant increase in speed with the current design. A control system has been presented that improves stability, robustness and performance over conventional quadrotors. Furthermore, suggestions are made on the light of the results for the improvement of the design of the actuator suite that can lead to an order of magnitude improvement in the speed.

7.2 Future Work

7.2.1 Modelling

- **Flight Test Validation.** Flight testing campaign in order to compile data to carry out a quantitative validation of the simulation model. And, if necessary, some system identification techniques could be used to resolve mismatches.
- **Propeller Characterisation.** More measurements are needed to model the propeller for different range of attainable flight conditions. Including translational flight, climbing and descending flight. Also, ground effects should be estimated.
- **Airframe Aerodynamics.** In this work, since the objective was to stabilise the platform, the aerodynamic forces and moments of the airframe have been neglected. To produce a larger amplitude simulation model this effect should be quantified over a variety of flight conditions, specially high speed translational flight.
- **Propeller Interaction.** In this project no study of the interaction of the different propellers between each other has been carried out. This could prove to be significant source of disturbance, specially when the propellers are tilted.
- **Inertia Variation.** In the simulation model a constant averaged inertia is assumed, whereas in the real vehicle the inertia changes with the angle of the deflections of the servos, hence, this issue should be further studied and quantified. Although in the CAD model not much difference has been found between the two extreme positions this could become more significant if the rotors become heavier.

7.2.2 Control System

- **Path Planner for Autonomous Flight.** A next step in the development of automated testing and data gathering would be to design a path planner and follower on top of the control system already built. This could allow for better quality data gathering than manual flight.
- **Other Control Allocation Strategies.** The utilisation of dynamic control allocation to split the virtual control command into a high frequency component, dealt by the gyroscopic effects and a low frequency component, dealt by the motors could lead to new findings in performance improvement. Also, another more complete control allocation algorithms including actuator saturation should be also explored.
- **Nonlinear Controller.** Nonlinear controller design techniques could be a way to exploit the full potential of the new actuator strategy by implementing the full nonlinear dynamics of the actuators.
- **Actuator Redesign.** Rotor redesign to increase the nominal angular velocity of the propellers and its inertia. This could be carried out by changing the shape, to reduce the pitch and increase the nominal rpm, and the material to increase the inertia. Trade-offs in terms of weight, power consumption and control action should be performed.

Appendix A

Testing Setup

A.1 Introduction

In this appendix a full description of the testing setup and procedures will be presented. This appendix can also be found in Al-Rihani's thesis [2] since it is common for both reports.

Two main tests for the motors were conducted, static test and dynamic test. The static tests aim to assess the propeller performance by finding the aerodynamic coefficients C_T and C_Q . Also the static tests are intended to find the efficiency of the motor and to investigate the linearity of the system, specifically the ESC, and finally the overall performance of the propulsive system will be assessed. The dynamic test was designed to characterise the motor dynamics in order to find the transfer function of the motor.

Similarly, a dynamic test with the prototyped arm for the RC servomotors for both the servoblock and push pull was performed in order to obtain a Transfer function of both. Since no direct angle measurement was available the internal potentiometer was used as an output. For that a mapping between the potentiometer voltage of the servo to the output was also carried out.

Finally, a description of the ball joint rig that was used to tune and test the controller is also presented.

A.2 Motor Static Testing

Two static tests were performed for the propulsive system, the motor thrust static test and the motor torque static test.

The static tests objectives are:

- Characterise the propeller by finding the aerodynamic coefficients C_T and C_Q .
- Assess the efficiency of the motopropulsive system.

- Study the linearity of the system specifically the motor controller.
- Assess the overall performance of the propulsive system.

A.2.1 Motor Thrust Static Test

Aims of the test

The motor thrust static test is designed to find the relation between the input which an RC PWM in (ms) to the output which is the thrust generated (g) and the corresponding current consumption (A) and propeller rotational speed (Hz) accordingly.

Test Setup

In order to measure the thrust of rotor an L shape adapter was used to change the direction of thrust to push on a scale, see figure A.1. This adapter is attached to a swivel joint so that it rotates freely. The distance from the rotor centre to the swivel axis is exactly the same to the distance from the swivel axis to the pushing point on the scale surface. This allows the propeller thrust to be projected as is to the scale. The scale has a resolution of 1g, and maximum capacity of 5 kg.

The rotation speed is measured by laser interferometer based on a phototransistor. The phototransistor is fixed behind the rotor to a fixed frame. On the front side of the propeller a laser pointer is also fixed to a fixed frame. The laser beam is pointed to the phototransistor such the beam crosses through the propeller disk. Hence, when the propeller rotates, the blades cross the beam, switching on and off the phototransistor with each blade. Thus, for a 3-blade propeller the beam is crossed three times per revolution. This setup is illustrated in figure A.2.

The Phototransistor is connected to a circuit as shown in figure A.3. An oscilloscope probe is connected to the point shown in the circuit. In a way that the oscilloscope reads 0 when the laser beam illuminates the phototransistor and when a blade of the propeller crosses the laser beam the phototransistor is not illuminated and the oscilloscope reads 5v. Hence, with the propeller rotating, a train of pulses will be read by the oscilloscope whose frequency can be recorded. Because the the propeller has 3 blades one third of the train of pulses will be the frequency of the propeller. A sample of the pulse train is shown as seen in the oscilloscope in figure A.4, where both the PWM input and the phototransistor output are displayed.

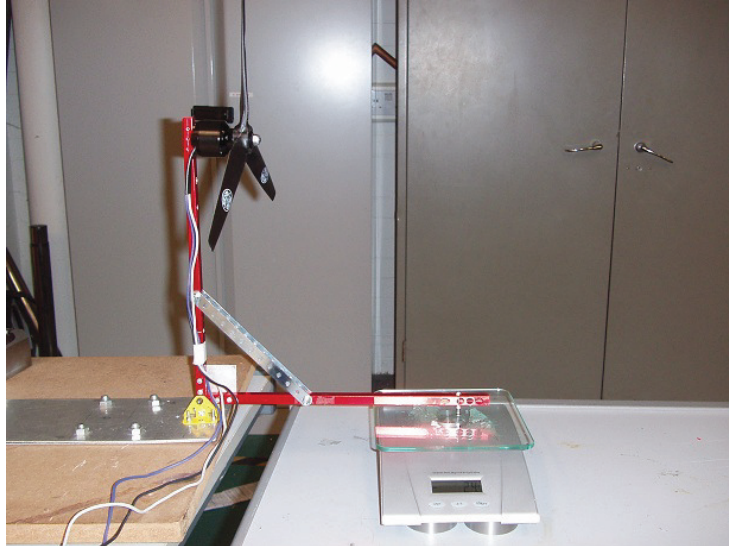


Figure A.1: Motor thrust static test setup

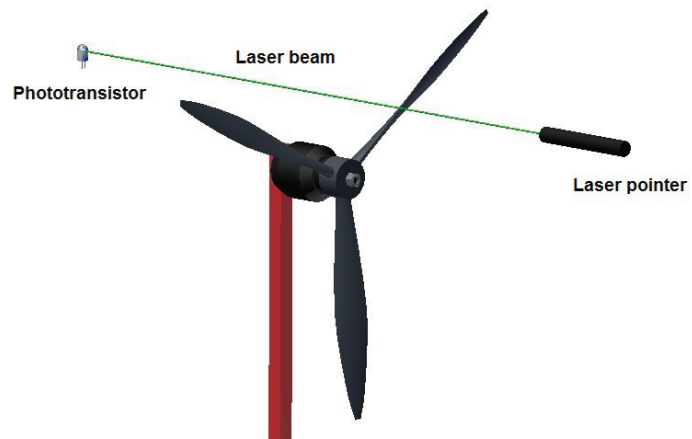


Figure A.2: Laser interferometer setup

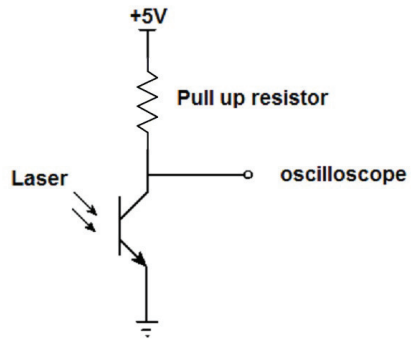


Figure A.3: Phototransistor Circuit

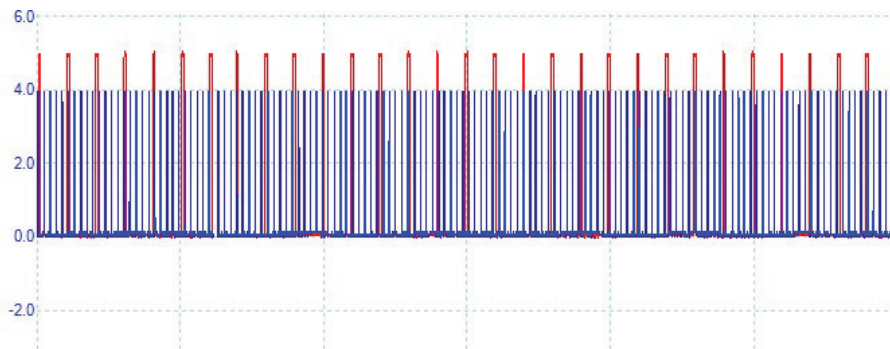


Figure A.4: Train of pulses as read by the oscilloscope. The PWM signal sent to the ESC in red, and the laser interferometer signal in blue

Test procedure

- Atmospheric conditions are recorded and listed in table A.1.
- The components are connected following the same pattern as in the final vehicle. i.e The motor is connected to the ESC, and the ESC input signal is connected to the Servo controller board. The servo controller board is connected to the microcontroller board via serial.
- The ESC is powered from a power supply at 16V with a limiting current of 30A, the maximum recommended for the ESC.
- Teaching the ESC for the input signal is done from 1.0 ms minimum to 2.0 ms maximum according to the manufacturer directions.
- The test starts by sending a commands of a PWM width of 1.1 to 1.95 and recording the corresponding propeller frequency with the oscilloscope, the current consumption as indicated by the power supply, and the generated thrust as indicated by the scale.
- The test is repeated three times.

Recorded data are listed in tables A.2 and A.3.

Temperature	20°C
Pressure	989 millibars
Humidity	51 %
Density	1.17

Table A.1: Motor static thrust test environment conditions

Duty Cycle (ms)	Prop Freq (Hz)	Current (A)	Thrust (g)
1.1	58	0.18	23
1.1	58.4	0.18	24
1.1	58.7	0.19	26
1.15	71	0.26	39
1.15	71	0.26	41
1.15	71.5	0.26	42
1.2	93.75	0.45	75
1.2	93.4	0.45	74
1.2	93.7	0.45	75
1.25	120	0.8	135
1.25	120	0.8	136
1.25	122.2	0.82	143
1.3	146	1.29	217
1.3	145.8	1.31	218
1.3	146.2	1.3	225
1.35	171	2	328
1.35	171	2.02	322
1.35	173	2.04	332
1.4	198	2.92	418
1.4	198.2	2.9	422
1.4	198.7	2.92	420
1.45	219.5	3.98	527
1.45	220	4	530
1.45	221.1	4	533
1.5	245	5.37	662
1.5	242.3	5.35	665
1.5	245	5.33	653
1.55	264.8	6.65	770
1.55	264	6.76	773
1.55	262.9	6.55	750
1.6	283.4	8.27	890
1.6	285.4	8.33	900
1.6	283	8.21	887
1.65	304.1	10.25	1040
1.65	305	10.2	1030
1.65	304.4	10.15	1023

Table A.2: Motor static thrust test recorded data part 1

Duty Cycle (ms)	Prop Freq (Hz)	Current (A)	Thrust (g)
1.7	321	12.13	1170
1.7	320.6	12	1150
1.7	323	12	1144
1.75	340	14.5	1297
1.75	339	14.5	1298.5
1.75	337.9	14.45	1300
1.8	354	16.7	1403
1.8	355	16.8	1400
1.8	354	16.6	1420
1.85	368	19.1	1544
1.85	368.8	19.2	1520
1.85	369	19.25	1539
1.9	383	22.1	1660
1.9	381	22.2	1633
1.9	383.9	22.3	1660
1.95	393	24	1733
1.95	394.5	24	1723
1.95	392	23.85	1711

Table A.3: Motor static thrust test recorded data part 2

A.2.2 Motor Torque static Test

Aims of the test

The motor thrust static test is designed to find the relation between the RC PWM in (ms) to the outputs, the torque generated (Nm), the current consumption (A) and the propeller rotational speed (Hz) accordingly.

Test Setup

In order to measure the torque of rotor, the same L shape adapter was used to change the direction of torque to push on a scale, see figure A.5. Unlike the thrust test, in this test the motor was mounted on the side of the adapter. This adapter is attached to a swivel joint that is giving the L shape adapter the ability to rotate freely. The distance from the swivel axis to the pushing point on the scale surface is 132mm. The scale is the same used in the previous test, it has a resolution of 1g, and maximum capacity of 5 kg.



Figure A.5: Motor torque static test setup

Test procedure

- Atmospheric conditions are recorded and shown in table A.4.
- The components are connected with the same layout that the vehicle, i.e, the motor is connected to the ESC, and the ESC input signal is connected to the Servo controller board. The servo controller board is connected to the microcontroller board via serial.
- The ESC is powered from a power supply at 16V with a limiting current of 30A, the maximum recommended for the ESC.
- The ESC teaching was not repeated because they were ready from the thrust static test.
- The test starts by sending a commands of a PWM width of 1.1 to 1.95 and recording the corresponding propeller frequency from the oscilloscope, the current consumption as indicated by the power supply, the generated force due to the torque as indicated by the scale.
- The test is repeated three times.

Recorded data are listed in tables A.5 and A.6

Temperature	19.1°C
Pressure	966 millibars
Humidity	53 %
Density	1.18195

Table A.4: Motor static torque test environment Conditions

Duty cycle (ms)	Prop freq. (Hz)	Current (A)	Scale reading (g)	Torque (Nm)
1.1	57.8	0.19	13	1.72
1.1	58	0.19	10	1.32
1.1	57.5	0.19	5	0.66
1.15	70.5	0.26	10	1.32
1.15	70.4	0.26	11	1.45
1.15	70.4	0.26	5	0.66
1.2	93.7	0.46	16	2.11
1.2	93.85	0.45	19	2.51
1.2	93.7	0.45	12	1.58
1.25	121.5	0.83	28	3.70
1.25	119.6	0.79	30.28	4.00
1.25	119.4	0.78	25	3.30
1.3	149.4	1.4	32	4.22
1.3	148.8	1.25	35	4.62
1.3	149.1	1.4	29	3.83
1.35	173	2	45	5.94
1.35	172.5	2.05	41	5.41
1.35	173	2	42	5.54
1.4	198	3	56	7.39
1.4	197.8	2.93	52	6.86
1.4	197.8	3	56	7.39
1.45	220	4.2	78	10.30
1.45	220	4.15	74	9.77
1.45	219.2	4.1	72	9.50
1.5	243.6	5.54	88	11.62
1.5	243	5.5	89	11.75
1.5	243	5.5	82	10.82
1.55	262.5	6.9	100	13.20
1.55	262.4	6.8	95	12.54
1.55	262.2	6.91	97	12.80
1.6	280.4	8.57	120	15.84
1.6	280.7	8.5	114	15.05
1.6	281.2	8.5	110	14.52
1.65	300	10.5	122	16.10
1.65	300	10.45	128	16.90
1.65	300	10.5	120	15.84

Table A.5: Motor static torque test recorded data part 1

Duty cycle (ms)	Prop freq. (Hz)	Current (A)	Scale reading (g)	Prop speed Tachometer (RPM)
1.7	316.3	12.4	135	17.82
1.7	316	12.4	145	19.14
1.7	315.8	12.4	136	17.95
1.75	334.2	14.9	150	19.80
1.75	333.1	14.9	161	21.25
1.75	333.4	14.9	139	18.35
1.8	348.9	17.15	169	22.31
1.8	350	17.22	166	21.91
1.8	347.3	17.16	158	20.86
1.85	360	19.6	170	22.44
1.85	361	19.8	175	23.10
1.85	362.5	19.5	174	22.97
1.9	375.1	22.98	200	26.40
1.9	377	22.6	200	26.40
1.9	377.6	22.6	194	25.61
1.95	382	24.5	195	25.74
1.95	385	24.5	205	27.06
1.95	384.5	24.4	200	26.40

Table A.6: Motor static torque test recorded data part 2

A.3 Motor Dynamic Testing

Aims of the test

To simulate effectively the vehicle dynamics a clear picture of the dynamic of the motors should be obtained, hence, a test was conducted to identify the motor transfer function around operating point.

The strategy in this test is to give the motor a sinusoidal input and read the propeller frequency output, fit both to a sinusoidal function and then compare the input to the output to find the corresponding Gain and Phase. This is repeated for different frequencies gather enough data complete a bode plot representative the motor dynamics in which a transfer function is fitted.

Test Setup

The test setup is exactly the same as the motor static thrust test explained earlier.

Test procedure

- The motor run to archive a designated nominal point, 7.5N of nominal thrust.
- A series of sinusoidal inputs of the same amplitude and different frequencies were fed, the amplitude was 10% of throttle. Frequencies between 0.1Hz to 10Hz were tested.
- For each test, the input PWM and the propeller frequency were recorded against time. The sample rate reached 1 MSs (Mega Sample sec.) at the high frequencies.
- A sinusoidal function is fitted for both input and output data.
- The Gain and Phase are calculated for all the frequencies, results are listed in table A.7.
- From the amplitude and phase, a bode plot was created.
- A transfer function was fitted to the bode plot created and was found to be:

$$TF_{\text{motor}} = \frac{e^{-0.035s} 9.19}{(1 + 0.16s)} \quad (\text{A.1})$$

For the detail procedure, refer to the modelling chapter.

Frequency (Hz)	Gain ($\frac{rad/s}{ms}$)	Phase(rad)
0.1	8.8995	-0.1484
0.2	8.7764	-0.2616
0.3	8.6197	-0.3511
0.4	8.4082	-0.4601
0.5	8.1532	-0.5506
0.6	7.9208	-0.6422
0.7	7.6004	-0.7258
0.8	7.2862	-0.8042
0.9	6.9953	-0.8876
1	6.7453	-0.9470
2	4.2049	-1.5020
3	2.9658	-1.8573
4	2.2399	-2.1649
5	1.8128	-2.4358
6	1.4980	-2.6999
7	1.2878	-2.9653
8	1.0901	-3.2291
9	0.9340	-3.4705
10	0.8232	-3.7513

Table A.7: Motor dynamic test recorded data

A.4 Servo Dynamic Testing

A.4.1 Servo mapping Test

RC Servos are composed of an electrical motor, a gear box, a control circuit, a potentiometer that reads the actual position of the servo output spline, send this feedback to the controller that positions the output spline as commanded. See figure A.6.

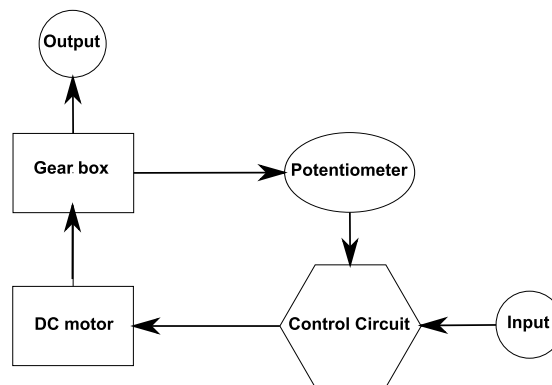


Figure A.6: Servo internal model

Aims of the test

To properly find the dynamic model of the RC servo, a way to measure the output of the servo is needed. The servo output is the angle of its arm. There is not a trivial way to measure the angle position directly in motion, hence, another way to obtain the angle must be found. Since the RC servo contains already a potentiometer, it can be used to find the angle. To do so, a mapping between potentiometer output in volts and the corresponding angle is to be carried out. Since this relation is linear, the transfer function from mS to potentiometer volts can be found and then scaled to convert to volts to angle.

Figure A.7 shows the control circuit of the HS-7950TH servo, and the arrow points to the microcontroller pin that is connected to the potentiometer. By soldering a wire here, the potentiometer voltage is accessible.

It was found that the feedback signal was noisy, and to solve this issue, a low pass filter available in the Pico software of the USB Oscilloscope was used. The cutoff frequency depends on each test and was between 100Hz to 700Hz.

Test Setup

To find the relation between potentiometer volts and the angle a feedback wire was connected to the potentiometer output of the HS-7950TH servo to read the

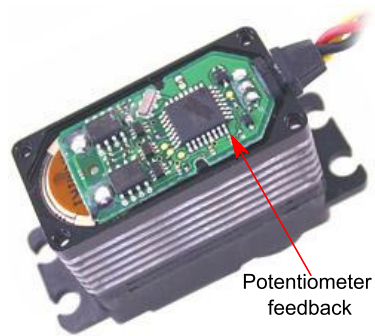


Figure A.7: HS-7950TH servo control Circuit

voltage representing the servo angle. And a Protractor was fixed to the servo as shown in figure A.8, to read the change in the servo arm angle.

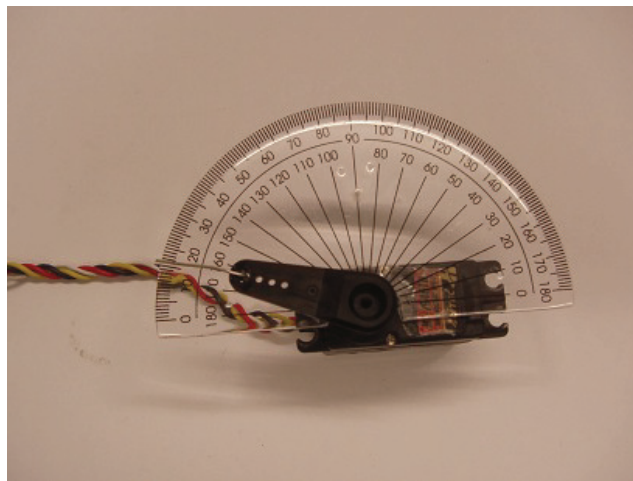


Figure A.8: Servo mapping using a Protractor

Test procedure

- The servo is feed a PWM input signal starting from 0.8 ms to 2.2 ms.
- For each input value, the feedback voltage of the potentiometer is recorded, and the net angle is read on the Protractor.
- The test is repeated three times.

Table A.8 and A.9 list all the recorded data.

input PWM (ms)	Feedback (V)	Angle(deg)
0.7971	2.465	0
0.7977	2.465	-0.5
0.7981	2.465	-0.2
0.845	2.401	4
0.8451	2.4	4
0.8909	2.339	8.5
0.8988	2.329	9.5
0.899	2.328	9.5
0.946	2.275	9
0.9469	2.276	9
0.992	2.194	18.5
1	2.192	19.5
1	2.192	19.5
1.046	2.145	19
1.046	2.146	24
1.093	2.069	29
1.093	2.071	29
1.093	2.072	28.8
1.147	2.009	29.5
1.147	2.009	34.5
1.186	1.966	38.5
1.194	1.956	40
1.194	1.955	39.5
1.248	1.857	45.5
1.248	1.854	45.5
1.287	1.803	49.5
1.294	1.791	50.5
1.294	1.791	50.5
1.349	1.737	55.5
1.349	1.737	55.5
1.387	1.67	59
1.395	1.655	59.5
1.395	1.654	59.8
1.449	1.604	65
1.449	1.604	65.2
1.48	1.559	68
1.496	1.528	70
1.496	1.527	69.5

Table A.8: Servo mapping test recorded data part 1

input PWM (ms)	Feedback (V)	Angle(deg)
1.55	1.46	75
1.55	1.461	74.8
1.581	1.426	78
1.597	1.401	79.5
1.597	1.4	79
1.643	1.335	84
1.643	1.334	84
1.682	1.285	87.5
1.697	1.257	88.5
1.697	1.258	88.9
1.744	1.201	93.5
1.744	1.2	93.5
1.775	1.154	96.5
1.798	1.112	99
1.798	1.113	99
1.845	1.066	98.5
1.876	1.022	106.5
1.9	0.984	108.5
1.945	0.9304	108.5
1.969	0.888	115.5
2	0.86	118.5
2.046	0.7945	123.5
2.069	0.7536	126
2.093	0.726	128.5
2.147	0.6586	129.5
2.193	0.579	138.5
2.248	0.5256	143.5

Table A.9: Servo mapping test recorded data part 2

A.4.2 Servoblock Servo Dynamic Test

Aims of the test

To simulate the vehicle and to be able to design and test the controller, an accurate dynamic model of the Servoblock servo is needed. So the aim of this test is to identify the servoblock servo transfer function by fitting frequency information of input and output of the system.

Test Setup

The prototype of one arm of the UAV was built according to the design as can be seen in figure A.9. The two servos that were used are fitted with feedback. The servoblock was mounted to a fixed frame as shown in figure A.10.

Test procedure

- The motor starts to run to a nominal speed of around 5000RPM which gives around 7.5N of thrust, that is the share of each rotor of the total nominal thrust (30N).
- The command to the Push pull servo is set in the middle during the test.
- A series of sinusoidal inputs of the same amplitude and different frequencies are fed to the servoblock servo. Frequencies between 0.6Hz to 15Hz are tested.
- For each test, the input PWM and the feedback of the servo are recorded using the oscilloscope.
- The strategy to get the Gain and Phase and then the transfer function are similar to the one used in the motor dynamic testing. Gain and Phase are listed in table A.10 and the transfer function is found to be:

$$TF_{\text{servoblock}} = \frac{1228.05}{1228.05 + 49.1806s + s^2} \quad (\text{A.2})$$

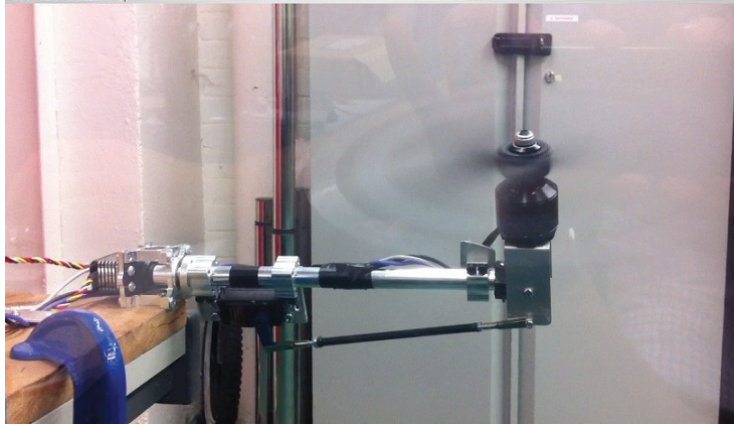


Figure A.9: Prototype of one arm was build for testing

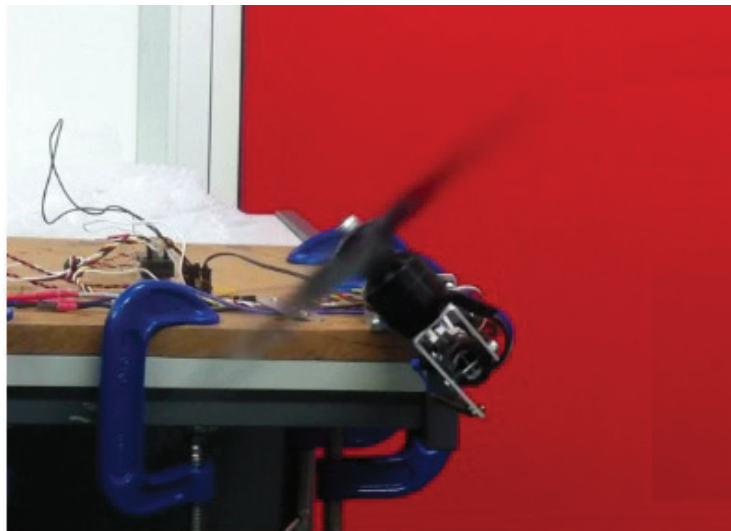


Figure A.10: Servoblock dynamic test

Frequency (Hz)	Gain (V/s)	Phase(rad)
0.6	1343.30	-3.2775
0.85	1310.83	-3.3524
1	1346.28	-3.3943
1.3	1343.26	-3.4604
1.5	1251.91	-3.5177
2	1293.12	2.6343
2.5	1247.28	-3.7269
3	1225.60	2.4419
4	1103.99	-3.9727
5	1146.98	-4.3007
6	873.53	-5.0570
7	725.13	-4.9763
8	563.05	-5.3310
9	389.88	-5.3900
10	366.60	-5.3814
11	302.96	-5.3860
15	245.21	-5.4434

Table A.10: Servoblock servo dynamic test recorded data

A.4.3 Push-Pull Servo Dynamic Test

Aims of the test

Similar to the servoblock dynamic identification, to simulate the vehicle and be able to design and test the controller, a proper dynamic model of the push pull servo is needed. So the aim of this test is to identify the pushpull servo transfer function by fitting a TF in the frequency domain.

Test Setup

The same setup that was used for the servoblock dynamic test and as shown in figure A.11.

Test procedure

- The motor starts to run to a nominal speed of around 5000RPM that is supposed to give a 7.5N of thrust, the nominal thrust.
- The command to the servoblock servo is set in the middle, neutral, during the test.
- A series of sinusoidal inputs of the same amplitude and different frequencies are feed to the push pull servo. Frequencies between 0.1Hz to 14Hz are tested.
- For each test, the input PWM and the feedback of the servo is recorded using the oscilloscope.
- As in the motor dynamic test, Gain and Phase are calculated, then a transfer function was fitted. The Gain and Phase are listed in table A.11. And the transfer function is found to be:

$$TF_{\text{pushpull}} = \frac{1212.73}{1212.73 + 51.105s + s^2} \quad (\text{A.3})$$

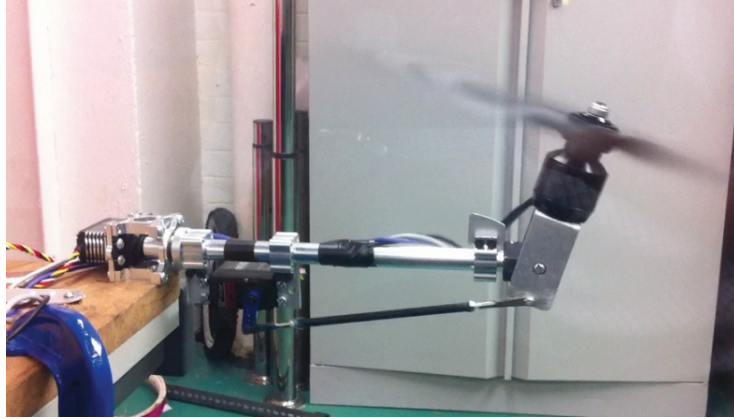


Figure A.11: pushpull dynamic test

Frequency (Hz)	Gain (V/s)	Phase(rad)
0.1	1346.54	-3.1590
0.5	1346.44	-3.2794
0.8	1340.76	-3.3683
0.9	1332.00	-3.3991
1	1297.08	-3.4279
1.2	1310.74	-3.4843
1.5	1308.24	-3.5862
1.75	1292.85	-3.6554
2	1263.64	-3.6997
2.5	1166.99	-3.8726
3	1128.83	-3.9609
4	1121.90	-4.0030
5	1143.28	-4.2335
6	803.17	-4.9234
7	818.51	-4.8722
8	415.74	-5.2796
9	338.12	-5.0105
10	301.93	-5.0967
11	318.42	-5.1508
12	292.92	-5.0771
14	292.92	-5.0771

Table A.11: Push-Pull dynamic test recorded data

A.5 Ball Joint Rig

The ball joint rig was build to tune and test the controller. The rig will constrain the translational movement of the vehicle in all directions but will enable freely the rotational movement.

Test of stability by applying perturbations in Pitch, Roll and Yaw was performed. Results can be seen in the Results chapter.

The rig was build using a 8mm plastic ball joint from igus. It was attached to a small bicycle axle. see figure A.12. The UAV is attached to the joint from the bottom. Using the ball joint gives the UAV the flexibility to tilt freely in roll and pitch, and using the axle will allow the UAV to rotate freely in the yaw.

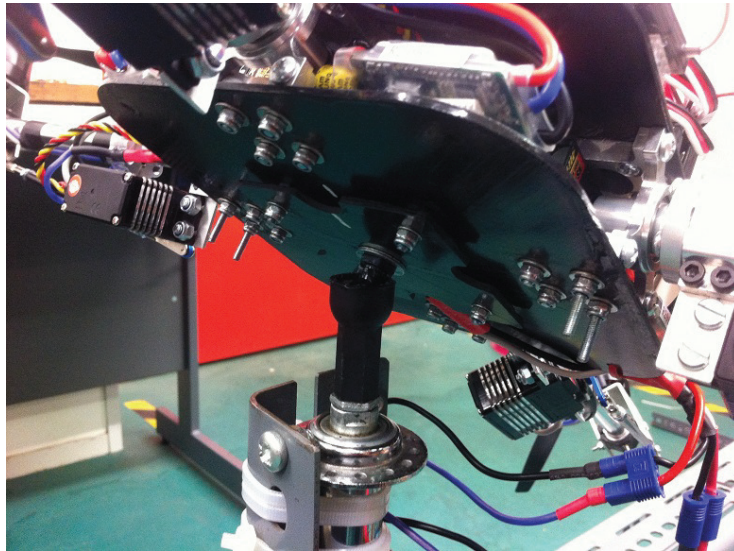


Figure A.12: Balljoint

There was an offset between the ball and the vehicle's centre of gravity, thus made the vehicle to act as inverted-pendulum and hence making it more unstable than in flight. However the testing show that controller was robust enough to handle this destabilising effect.

Appendix B

2 blade or 3 blade propellers

B.1 Introduction

In this appendix the mathematical reasoning behind the election of a two blade propeller vs a three blade propeller will be developed. This will be based on the two propellers that were considering initially in the design, both propellers attached to the outrunner part of the brushless DC motor are shown in figures B.1(a) and B.1(b).

To simplify and to reduce the mathematical burden, the reasoning of the the tilting reaction equations derivation only one degree of tilting will be developed. The degree preserved will be the push-pull described in the main text. A picture of the reference frame used is in figure B.2

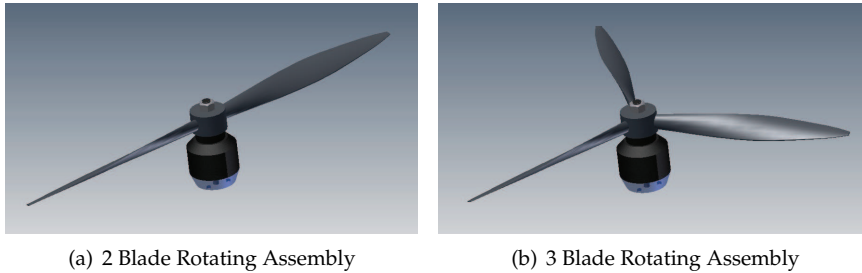


Figure B.1: Two propeller considered attached to the rotor of the motor outrunner motor.

The key difference between both propellers is its inertia tensor. The inertia tensor for the 2 blade and the 3 blade rotating assembly is shown below as obtained from the CAD software.

$$\mathbf{I}_{2\text{blade}} \begin{bmatrix} 109.781 & 0.426 & 0 \\ 0.426 & 17.569 & 0 \\ 0 & 0 & 100.588 \end{bmatrix} \text{ kg mm} \quad (\text{B.1})$$

$$\mathbf{I}_{3\text{blade}} \begin{bmatrix} 69.407 & 0 & 0 \\ 0 & 69.407 & 0 \\ 0 & 0 & 110.856 \end{bmatrix} \text{kg mm} \quad (\text{B.2})$$

The important point here is the difference between $I_{xx2\text{Blade}}$ and $I_{yy2\text{Blade}}$ because $I_{xx2\text{Blade}} \propto 10I_{yy2\text{Blade}}$. While in the 3 blade $I_{xx3\text{Blade}} = I_{yy3\text{Blade}}$. As the a very important control action is based on the gyroscopic effects this difference is fundamental and will affect greatly the performance as will be shown in the equations that will be developed next.

B.2 Newton Euler Description

The gyroscopic moments created by the propellers when they are tilted are described by the Euler equation of motion. That is:

$$\mathbf{M}_i = \frac{d}{dt}\mathbf{M} = \mathbf{I}_i\boldsymbol{\alpha}_i + \boldsymbol{\omega}_i \times \mathbf{I}_i\boldsymbol{\omega}_i \quad (\text{B.3})$$

Where \mathbf{M}_i is the moment in the centre of gravity. \mathbf{I}_i is the inertia tensor in the reference frame i respect to the CG, $\boldsymbol{\alpha}_i$ is the total angular acceleration of the body in the reference frame i , i.e. $\boldsymbol{\alpha} = \frac{d}{dt}\boldsymbol{\omega}$, and $\boldsymbol{\omega}$ is the total angular velocity.

Equation B.3 establishes the relationship between the rotation motion of a spinning body and the actions, moments, applied onto its CG.

Frames Used

Three non inertial reference frames are used to describe the rotating motion of the spinning assembly.

- Reference Frame 1 attached to the Vehicle.
- Reference Frame 2 attached to the PushPull, i.e. to the motor mount.
- Reference Frame 3 attached to the Rotating Body, i.e. rotating with it.

Rotation Matrices

The relation between the representation of vectors in each frame are given by its rotation matrices matrices. That is to rotate an arbitrary vector \mathbf{v} from the Reference Frame 2 to the Reference Frame 1:

$${}^1\mathbf{v} = \mathbf{R}_{2\text{to}1} {}^2\mathbf{v} \quad (\text{B.4})$$

Where $\mathbf{R}_{2\text{to}1}$ is:

$$\mathbf{R}_{2\text{to}1} = \begin{bmatrix} 1 & 0 & 0 \\ 0 & \cos(\gamma) & -\sin(\gamma) \\ 0 & \sin(\gamma) & \cos(\gamma) \end{bmatrix} \quad (\text{B.5})$$

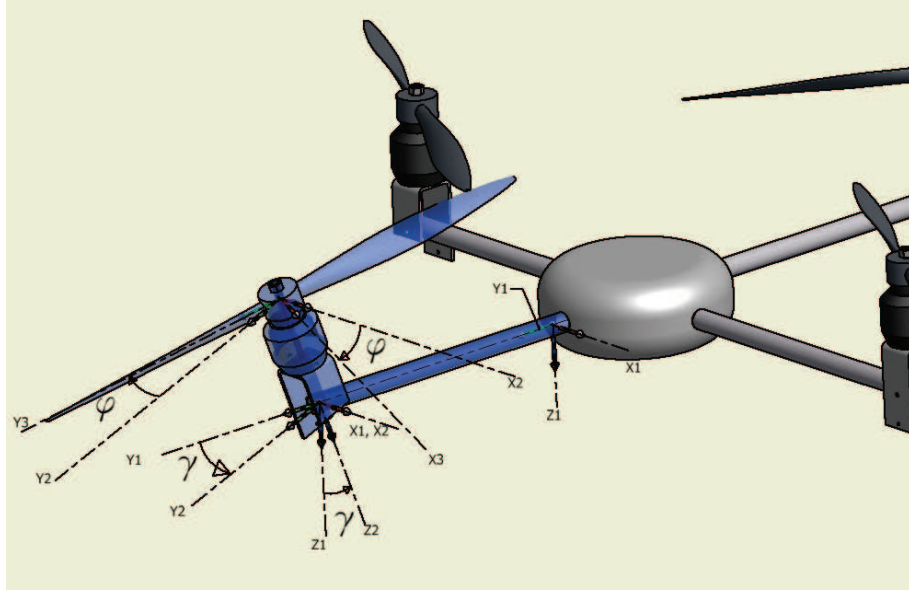


Figure B.2: Reference Frames

As the rotation matrices are unitary and orthogonal their transpose is equivalent to their inverse therefore:

$$\mathbf{R}_{1to2} = \mathbf{R}_{2to1}^T = \begin{bmatrix} 1 & 0 & 0 \\ 0 & \cos(\gamma) & -\sin(\gamma) \\ 0 & \sin(\gamma) & \cos(\gamma) \end{bmatrix}^T = \begin{bmatrix} 1 & 0 & 0 \\ 0 & \cos(\gamma) & \sin(\gamma) \\ 0 & -\sin(\gamma) & \cos(\gamma) \end{bmatrix} \quad (\text{B.6})$$

Similarly the rotation matrices from the frames 3 to 2 and from the frames 2 to 3 are defined:

$$\mathbf{R}_{3to2} = \begin{bmatrix} \cos(\phi) & -\sin(\phi) & 0 \\ \sin(\phi) & \cos(\phi) & 0 \\ 0 & 0 & 1 \end{bmatrix} \quad (\text{B.7})$$

$$\mathbf{R}_{2to3} = \begin{bmatrix} \cos(\phi) & \sin(\phi) & 0 \\ -\sin(\phi) & \cos(\phi) & 0 \\ 0 & 0 & 1 \end{bmatrix} \quad (\text{B.8})$$

Now combining them, the rotation matrices from 1 to 3 and from 3 to 1 can be obtained:

$$\mathbf{R}_{1to3} = \mathbf{R}_{2to3} \mathbf{R}_{1to2} = \begin{bmatrix} \cos(\phi) & \cos(\gamma) \sin(\phi) & \sin(\gamma) \sin(\phi) \\ -\sin(\phi) & \cos(\gamma) \cos(\phi) & \cos(\phi) \sin(\gamma) \\ 0 & -\sin(\gamma) & \cos(\gamma) \end{bmatrix} \quad (\text{B.9})$$

$$\mathbf{R}_{3to1} = \begin{bmatrix} \cos(\phi(t)) & -\sin(\phi(t)) & 0 \\ \cos(\gamma) \sin(\phi(t)) & \cos(\gamma) \cos(\phi(t)) & -\sin(\gamma) \\ \sin(\gamma) \sin(\phi(t)) & \cos(\phi(t)) \sin(\gamma) & \cos(\gamma) \end{bmatrix} \quad (\text{B.10})$$

Unit Vectors

As the different motions are expressed in the different reference frames it is needed to define the unitary vectors of the different reference frame with respect to the common reference frame. In this case, the Euler equation hold for a reference frame that is attached to the propeller assembly, therefore the reference frame 3 must be the common reference frame upon all motions are described.

$${}^3\mathbf{i}_1 = \mathbf{R}_{1to3} {}^1\mathbf{i}_1 = \mathbf{R}_{1to3} \begin{bmatrix} 1 \\ 0 \\ 0 \end{bmatrix} = \begin{bmatrix} \cos(\phi) \\ -\sin(\phi) \\ 0 \end{bmatrix} \quad (\text{B.11})$$

Similarly the vectors in the y and z axes can be defined:

$${}^3\mathbf{j}_1 = \begin{bmatrix} \cos(\gamma) \sin(\phi) \\ \cos(\gamma) \cos(\phi) \\ -\sin(\gamma) \end{bmatrix} \text{ and } {}^3\mathbf{k}_1 = \begin{bmatrix} \sin(\gamma) \sin(\phi) \\ \cos(\phi) \sin(\gamma) \\ \cos(\gamma) \end{bmatrix} \quad (\text{B.12})$$

Likewise Unit Vectors of the frame 2 are referred to the frame 3.

$${}^3\mathbf{i}_2 = \mathbf{R}_{2to3} {}^2\mathbf{i}_2 = \begin{bmatrix} \cos(\phi) \\ -\sin(\phi) \\ 0 \end{bmatrix}, {}^3\mathbf{j}_2 = \mathbf{R}_{2to3} {}^2\mathbf{j}_2 = \begin{bmatrix} \sin(\phi) \\ \cos(\phi) \\ 0 \end{bmatrix} \text{ and } {}^3\mathbf{k}_2 = \mathbf{R}_{2to3} {}^2\mathbf{k}_2 = \begin{bmatrix} 0 \\ 0 \\ 1 \end{bmatrix} \quad (\text{B.13})$$

Angular Velocity

Now that all the unit vectors are defined the motion of rotation of the tilting propeller can begin to be specified.

First, Rotation due to the push-pull. This is the contribution of the push-pull tilt motion, its reference axis is the arm, that is Reference Frame 2 and its angle is γ thus:

$${}^3\boldsymbol{\omega}_{\text{pushpull}} = {}^3\mathbf{i}_1 \dot{\gamma} \quad (\text{B.14})$$

Second, Rotation due to the motor, that is the spinning propeller, this vector will be defined in the reference frame of the body, i.e. along the shaft of the motor. Therefore:

$${}^3\boldsymbol{\omega}_{\text{motor}} = {}^3\mathbf{k}_2 \dot{\phi} \quad (\text{B.15})$$

Summing up the total angular velocity of the rotating assembly expressed in the reference frame 3 is:

$${}^3\boldsymbol{\omega}_{\text{total}} = {}^3\boldsymbol{\omega}_{\text{pushpull}} + {}^3\boldsymbol{\omega}_{\text{motor}} \quad (\text{B.16})$$

Expanding:

$${}^3\boldsymbol{\omega}_{\text{total}} = {}^3\mathbf{i}_1 \dot{\gamma} + {}^3\mathbf{k}_3 \dot{\phi} \quad (\text{B.17})$$

Now recalling the unit vectors definition an simplifying:

$${}^3\boldsymbol{\omega}_{\text{Total}} = \begin{bmatrix} \cos(\phi) \dot{\gamma} \\ -\sin(\phi) \dot{\gamma} \\ \dot{\phi} \end{bmatrix} \quad (\text{B.18})$$

B.2.1 Angular Acceleration

Now the angular acceleration will be calculated. Note that as the vectors are expressed in a rotating frames a cross product term arises.

As with the angular velocity the angular acceleration is given by the following contributions:

Acceleration due to the push-pull:

$${}^3\alpha_{\text{pushpull}} = {}^3\mathbf{i}_2\ddot{\gamma} \quad (\text{B.19})$$

Acceleration of due to the motor:

$${}^3\alpha_{\text{motor}} = {}^3\mathbf{k}_3\ddot{\phi} + {}^3\boldsymbol{\omega}_{\text{pushpull}} \times {}^3\mathbf{k}_3\dot{\phi} \quad (\text{B.20})$$

Resolving the terms into its components and simplifying results in:

$${}^3\alpha_{\text{Total}} = \begin{pmatrix} \cos(\phi)\ddot{\gamma} - \sin(\phi)\dot{\gamma}\dot{\phi} \\ -\cos(\phi)\dot{\gamma}\dot{\phi} - \sin(\phi)\ddot{\gamma} \\ \ddot{\phi} \end{pmatrix} \quad (\text{B.21})$$

B.2.2 Total Moments

Now, as the propeller has 3 blades and the rotor of the motor is symmetric the inertia tensor is diagonal. Thus introducing the calculated α_{Total} and ω_{Total} into equation B.3 yields:

$${}^3M_{\text{Total}} = \begin{bmatrix} (I_{xx} \cos(\phi) - I_{xy} \sin(\phi))\ddot{\gamma} - (2I_{xy} \cos(\phi) + (I_{xx} - I_{yy} + I_{zz}) \sin(\phi))\dot{\gamma}\dot{\phi} \\ ((I_{xx} - I_{yy} - I_{zz}) \cos(\phi) - 2I_{xy} \sin(\phi))\dot{\gamma}\dot{\phi} + (I_{xy} \cos(\phi) - I_{yy} \sin(\phi))\ddot{\gamma} \\ (I_{xy} \cos(2\phi) + (I_{xx} - I_{yy}) \cos(\phi) \sin(\phi))\dot{\gamma}^2 + I_{zz}\ddot{\phi} \end{bmatrix} \quad (\text{B.22})$$

This are the moments in reference frame 3 about the CG of the rotating assembly that are caused by the movement described. Therefore the reactions on the airframe will be $-{}^3\mathbf{M}$. Also they have to be expressed in the body axis, i.e. in the frame 1. Thus the total action of the tilt on the airframe is:

$${}^1\mathbf{M}_{\text{React}} = \mathbf{R}_{3to1}(-{}^3\mathbf{M}) \quad (\text{B.23})$$

$${}^1\mathbf{M}_{\text{React}} = \begin{bmatrix} {}^1\mathbf{M}_{\text{ReactX}} \\ {}^1\mathbf{M}_{\text{ReactY}} \\ {}^1\mathbf{M}_{\text{ReactZ}} \end{bmatrix} \quad (\text{B.24})$$

$${}^1\mathbf{M}_{\text{ReactX}} = \frac{1}{2}((2(2I_{xy} \cos(2\phi) + (I_{xx} - I_{yy}) \sin(2\phi))\dot{\gamma}\dot{\phi} - (I_{xx} + I_{yy} + (I_{xx} - I_{yy}) \cos(2\phi) - 2I_{xy} \sin(2\phi))\ddot{\gamma})) \quad (\text{B.25})$$

$$\begin{aligned}
{}^1\mathbf{M}_{\text{ReactY}} = \frac{1}{2} & \left((-\sin(\gamma)((I_{yy} - I_{xx}) \sin(2\phi) - 2I_{xy} \cos(2\phi))\dot{\gamma}^2 + 2\cos(\gamma)(I_{zz} + \right. \\
& (I_{yy} - I_{xx}) \cos(2\phi) + 2I_{xy} \sin(2\phi))\dot{\phi}\dot{\gamma} - \cos(\gamma)(2I_{xy} \cos(2\phi) + (I_{xx} - I_{yy}) \sin(2\phi))\ddot{\gamma} + \\
& \left. 2I_{zz} \sin(\gamma)\ddot{\phi} \right) \quad (\text{B.26})
\end{aligned}$$

$$\begin{aligned}
{}^1\mathbf{M}_{\text{ReactZ}} = \frac{1}{2} & \left((-\cos(\gamma)(2I_{xy} \cos(2\phi) + (I_{xx} - I_{yy}) \sin(2\phi))\dot{\gamma}^2 + 2\sin(\gamma)(I_{zz} + (I_{yy} \right. \\
& - I_{xx}) \cos(2\phi) + 2I_{xy} \sin(2\phi))\dot{\phi}\dot{\gamma} - \sin(\gamma)(2I_{xy} \cos(2\phi) + (I_{xx} - I_{yy}) \sin(2\phi))\ddot{\gamma} - 2I_{zz} \\
& \left. \cos(\gamma)\ddot{\phi} \right) \quad (\text{B.27})
\end{aligned}$$

Appendix C

Simulink Model

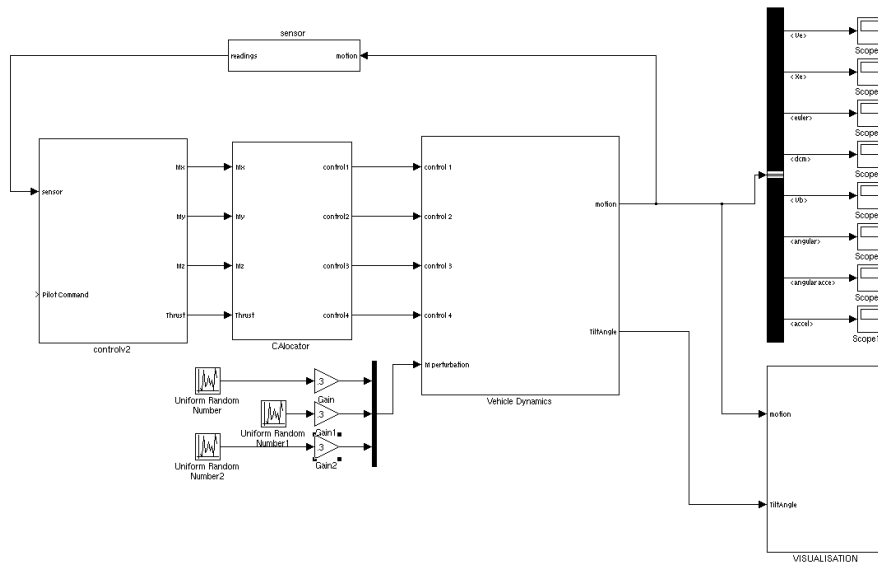


Figure C.1: General Structure of the Simulink Simulation Model

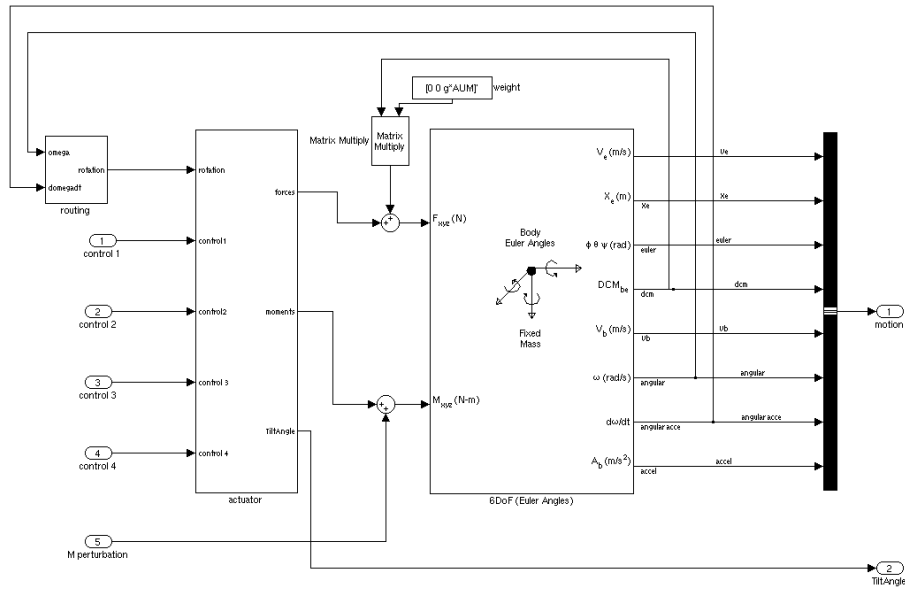


Figure C.2: Vehicle Dynamics block. Implementing the equations of motion and the actuator dynamics.

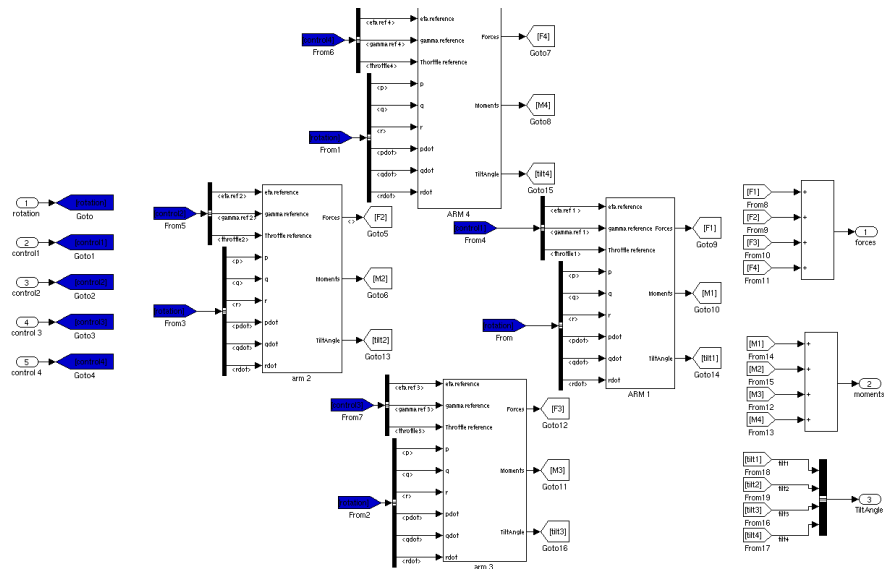


Figure C.3: Actuators Block. Implementing the dynamics of each actuator Arm.

Appendix D

Platform technical drawing

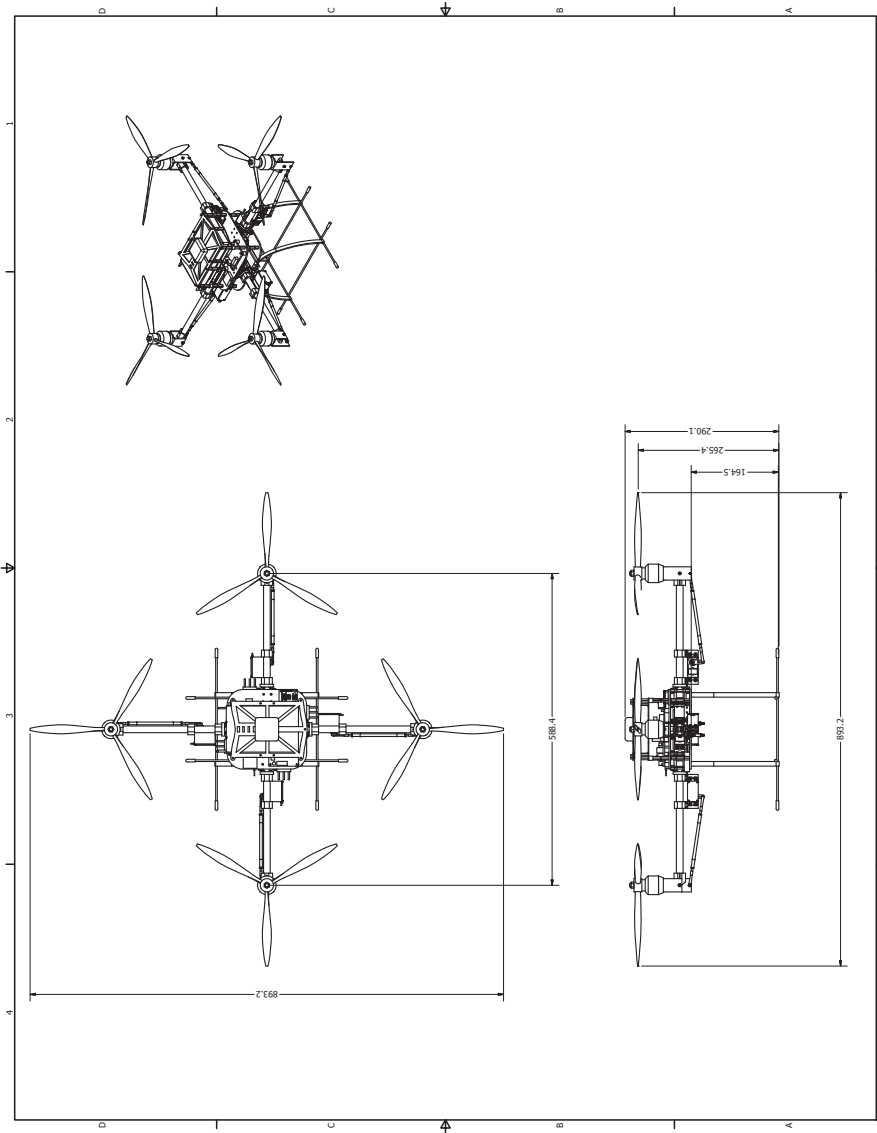


Figure D.1: Platform technical drawing

Appendix E

SBG IG-500N IMU Technical Specifications

IG-500N

Redefine motion limits...

GPS aided Orientation Sensor



The IG-500N is a miniature and high performance GPS enhanced Attitude and Heading Reference System (AHRS). With its embedded Extended Kalman Filter, the IG-500N delivers unmatched precision for attitude and position measurements even during very high dynamic conditions.

All in one: the IG-500N

The IG-500N includes a MEMS based Inertial Measurement Unit (IMU), a GPS receiver and a pressure sensor. It provides precise drift-free attitude and position, even in long time turns.

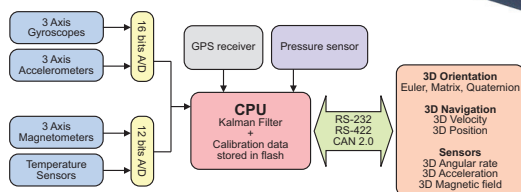
This miniature Inertial Navigation System (INS) runs a real time, on board, Extended Kalman Filter that computes orientation, position and velocity data at high update rates, up to 100 Hz.

The attitude accuracy is also improved, compared to traditional AHRS, by removing transient accelerations measured by the GPS receiver.

Easy and fast integration

SBG Systems has designed a powerful and easy to use Development Kit for this product. In just a few seconds, you can start evaluating and configuring your new device. Integrating the IG-500N in your application is even easier.

Simplified Block Diagram



Key Features

- GPS enhanced 3D velocity, position and orientation at high update rate (100 Hz)
- Accurate attitude even in high G maneuvers
- Precise UTC referenced output and SyncOut signal
- Embedded 4Hz GPS receiver & barometric sensor
- Wide inertial sensors range options
- Calibrated over full temperature range -40 to 85°C for bias, gain, misalignments, cross-axis and gyro-g
- Advanced and easy to use magnetometers compensation procedure for soft and hard iron
- Available protocols RS-232, RS-422, CAN and USB
- Very compact and lightweight design (44 grams)
- Very low power design down to 800 mW
- Robust and high precision aluminum enclosure

Fields of use

- Unmanned vehicles
- Vehicle motion analysis
- Aerospace
- Robotics
- Marine industry



Tel: +33 (0)1 80 88 45 00 • Mail: contact@sbg-systems.com • Web: www.sbg-systems.com

Figure E.1: SBG IG-500N IMU Technical Specifications

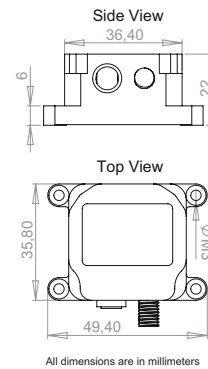
IG-500N

Redefine motion limits...

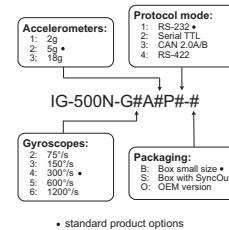
Technical Specifications

Parameter	Specification	Remarks		
Attitude				
Sensing range	360° in all axes			
Static accuracy	± 0.5° (Pitch, Roll) ± 1° (Heading)	Stabilized Kalman Filter Homogenous magnetic field		
Dynamic accuracy	± 1.0° RMS	Under good GPS availability		
Repeatability	< 0.2°			
Resolution	< 0.05°			
Output frequency	0 to 500 Hz 0 to 100 Hz	Calibrated sensors only Sensors, attitude, velocity, position		
Standard Sensors				
	Accelerometers	Gyroscopes	Magnetometers	
Measurement range	± 5 g	± 300 °/s	± 1.2 Gauss	Refer to sensors options table
Non-linearity	< 0.2% of FS	< 0.1% of FS	< 0.2% of FS	
Bias stability	± 5 mg	± 0.5 °/s	± 0.5 mGauss	Over temperature range Kalman filter stabilized
Scale factor stability	< 0.1%	< 0.05%	< 0.5%	Over temperature range
Noise density	0.25 mg/√Hz	0.05 °/s/√Hz	0.01 mG/√Hz	
Alignment error	< 0.1°	< 0.1°	< 0.1°	
Bandwidth	50 Hz	40 Hz	500 Hz	Additional software filter available
Sampling rate	10 000 Hz	10 000 Hz	1 000 Hz	
GPS Receiver				
Receiver type	L1 frequency, C/A Code, 50-Channels, 4 Hz			
Position accuracy	2.0 meters 2.5 meters 5.0 meters	with SBAS support CEP (Horizontal accuracy) SEP (Vertical accuracy)		
Acquisition time	< 1.0 s / 29 s	Hot start / Cold start		
Tracking sensitivity	-160 dB			
Pressure Sensor				
Resolution	2.5 Pa	20 cm resolution		
Pressure accuracy	± 50 Pa / ± 150 Pa	Relative / Absolute		
Long term stability	100 Pa	Over 12 months		
Update rate	100 Hz			
Communication				
Output modes	Euler angles, Quaternion, Matrix, 3D velocity, 3D position, Calibrated sensor data, Raw sensor and GPS data	Each output can be enabled or disabled by the user		
Interface options	Serial (RS-232, RS-422 or TTL 3.3V) CAN 2.0A/B up to 1 Mbit/s Usb using provided UsbToUart	RS-422 and CAN 2.0A/B are only available for OEM and S packages		
Serial data rate	9 600 to 921 600 bps	Configurable slew rate		
Physical				
Dimensions OEM	27x30x14 mm			
Dimensions box	36x49x22 mm / 36x49x25 mm	B package / S package		
Weight OEM	10 grams			
Weight box	44 grams / 49 grams	B package / S package		
Specified temperature	-40 to 85°C	Non-condensing environment		
Shock limit	1 000g (Powered), 2 000g (Unpowered)	Shocks can affect performance		
Electrical				
Operating voltage	3.3 V to 30 V			
Power consumption	800 mW @ 5.0 V	High efficiency DC/DC converter		
SyncOut, Trigger	Open drain pull-up voltage -0.3 to 25 V	Open drain, use a pull-up resistor		
Start-up time	< 1 s	Valid data		

Mechanical drawing



Product code options



Rev 2.1 Specifications are subject to change without notice.

SBG Systems s.a.s. • 3bis, chemin de la Jonchère • 92500 Rueil Malmaison • FRANCE



Figure E.2: SBG IG-500N IMU Technical Specifications

Bibliography

- [1] O. Garcia A. Sanchez, J. Escareño and R. Lozano. Autonomous hovering of a noncyclic tiltrotor uav: Modeling, control and implementation. *Proceedings of the 17th World Congress The International Federation of Automatic Control. Seoul, Korea., July 2008.*
- [2] Yazan Al-Rihani. Development of a dual axis tilt rotorcraft uav: Design, prototyping and control. *MSc Thesis, Cranfield University, 2012.*
- [3] Autodesk. Inventor. <http://www.autodesk.co.uk>.
- [4] Samir Bouabdallah. *Design and control of quadrotors with application to autonomous flying*. PhD thesis, 2007.
- [5] J. M. Buffington. Tailless aircraft control allocation. *AIAA Guidance, Navigation, and Control Conference and Exhibit, pages 737–747, New Orleans, LA, 1997.*
- [6] J. M. Buffington and D. F. Enns. Lyapunov stability analysis of daisy chain control allocation. *J. Guid. Control Dyn.*, 1996.
- [7] Michael V. Cook. *Flight Dynamic Principles*. Elsevier/Butterworth-Heinemann, 2007.
- [8] digilent. <http://www.digilentinc.com>, May 2012.
- [9] Guillaume J. J. Ducard and Minh-Duc Hua. Discussion and practical aspects on control allocation for a multi-rotor helicopter. *International Archives of the Photogrammetry, Remote Sensing and Spatial Information Sciences, Vol. XXXVIII-1/C22 UAV-g 2011, Conference on Unmanned Aerial Vehicle in Geomatics, Zurich, Switzerland, 2011.*
- [10] W. C. Durham. Constrained control allocation. *J. Guid. Control Dyn.*, 16:717–725, 1994.
- [11] W. C. Durham. Efficient, near-optimal control allocation. *J. Guid. Control Dyn.* 22:369–372, 1999.
- [12] D. Enns. Control allocation approaches. *AIAA Guidance, Navigation, and Control Conference and Exhibit, pages 98–108, Boston, MA, 1998.*
- [13] G. R. Gress. Using dual propellers as gyroscopes for tilt- prop hover control. *Proc. AIAA Biennial Int. Powered Lift Conf. Exhibit, Williamsburg, VA, Nov. 2002.*

- [14] Gary R. Gress. Lift fans as gyroscopes for controlling compact vtol air vehicles: Overview and development status of oblique active tilting. *American Helicopter Society 63th Annual Forum, Virginia Beach, VA*, May 2007.
- [15] Ola Harkegard. *Backstepping and Control Allocation with Applications to Flight Control*. PhD thesis, Dept. of Electrical Engineering, Linköping University, Sweden., 2003.
- [16] Aeryon Labs Inc. Aeryon scout. <http://www.aeryon.com/>, May 2012.
- [17] Digi International Inc. Xbee. <http://www.digi.com>, May 2012.
- [18] Jaehyun Jin. Modified pseudoinverse redistribution methods for redundant controls allocation. *JOURNAL OF GUIDANCE, CONTROL, AND DYNAMICS*, 2005.
- [19] Tor A. Johansen. Optimizing nonlinear control allocation. *IEEE Decision and Control, 2004. CDC. 43rd IEEE Conference on*, 2004.
- [20] F. Kendoul, I. Fantoni, and R. Lozano. Modeling and control of a small autonomous aircraft having two tilting rotors. In *Decision and Control, 2005 and 2005 European Control Conference. CDC-ECC '05. 44th IEEE Conference on*, pages 8144 – 8149, dec. 2005.
- [21] J.G. Leishman. *Principles of Helicopter Aerodynamics*. Cambridge Aerospace Series. Cambridge University Press, 2006.
- [22] Y-Y.; Moerder D. D.; Cooper E. G Lim, K. B.; Shin. A new approach to attitude stability and control for low airspeed vehicles. *AIAA Guidance, Navigation and Control Conference and Exhibit; ; Providence, RI; United States*, 16-19 Aug. 2004.
- [23] masterairscrew. 12 x 6 3-blade. <http://masterairscrew.com>, May 2012.
- [24] microdrones. <http://www.microdrones.com/>, May 2012.
- [25] Mikrokopter. <http://www.mikrokopter.de>, May 2012.
- [26] R. Davies N. Amiri, A. Ramirez-Serrano. Modelling of opposed lateral and longitudinal tilting dual-fan unmanned aerial vehicle. *18th IFAC World Congress Milano (Italy)*, Sept. 2011.
- [27] parallax. <http://www.parallax.com>, May 2012.
- [28] Peter Corke Paul Pounds, Robert Mahony. System identification and control of an aerobot drive system. *Information, Decision and Control*, 2007.
- [29] robbe. Roxxy bl control 930-6. <http://www.robbe.de>, May 2012.
- [30] ServoCity. <http://www.servocity.com/>, may 2012.
- [31] S. Skogestad and I. Postlethwaite. *Multivariable feedback control: analysis and design*. John Wiley, 2005.
- [32] Sparkfun. <http://www.sparkfun.com/>, May 2012.

- [33] spektrum. <http://www.spektrumrc.com/>, May 2012.
- [34] F. Robert Stengel. *Flight Dynamics*. Princeton University Press, 2004.
- [35] Sbg Systems. Ig-500n. <http://www.sbg-systems.com>, May 2012.
- [36] Ryohei Kitayoshi Ichiro Maruta Toshiharu Sugie Takashi Wada, Masato Ishikawa. Practical modeling and system identification of r/c servo motors. *18th IEEE International Conference on Control Applications Part of 2009 IEEE Multi-conference on Systems and Control Saint Petersburg*, July 8-10, 2009.
- [37] Menno Wierema. Design, implementation and flight test of indoor navigation and control system for a quadrotor uav. Master's thesis, Aerospace Engineering at Delft University of Technology, 2008.
- [38] xaircraft. <http://www.xaircraft.co.uk/>, May 2012.